Arch Computat Methods Eng
DOI 10.1007/s11831-017-9209-4

ORIGINAL PAPER

Recent Developments in Variational Multiscale Methods for Large-Eddy Simulation of Turbulent Flow

Ursula Rasthofer[1] · **Volker Gravemeier**[2]

Received: 8 December 2016 / Accepted: 2 January 2017

Abstract The variational multiscale method is reviewed as a framework for developing computational methods for large-eddy simulation of turbulent flow. In contrast to other articles reviewing this topic, which focused on large-eddy simulation of turbulent incompressible flow, this study covers further aspects of numerically simulating turbulent flow as well as applications beyond incompressible single-phase flow. The various concepts for subgrid-scale modeling within the variational multiscale method for large-eddy simulation proposed by researchers in this field to date are illustrated. These conceptions comprise (i) implicit large-eddy simulation, represented by residual-based and stabilized methods, (ii) functional subgrid-scale modeling via small-scale subgrid-viscosity models and (iii) structural subgrid-scale modeling via the introduction of multifractal subgrid scales. An overview on exemplary numerical test cases to which the reviewed methods have been applied in the past years is provided, including explicit computational results obtained from turbulent channel flow. Wall-layer modeling, passive and active scalar transport as well as developments for large-eddy simulation of turbulent two-phase flow and combustion are discussed to complete this exposition.

✉ Ursula Rasthofer
urasthofer@ethz.ch

Volker Gravemeier
vgravem@lnm.mw.tum.de

[1] Computational Science and Engineering Laboratory, ETH Zurich, Clausiusstr. 33, 8092 Zurich, Switzerland

[2] Institute for Computational Mechanics, Technical University of Munich, Boltzmannstr. 15, 85748 Garching, Germany

1 Introduction

Turbulent flows are ubiquitous in the technical field of engineering as well as the natural environment. Solar flares originate from the turbulence developing on the surface of the sun. Accurate weather forecasting is enabled by the knowledge of turbulent atmospheric flows involved in the formation of clouds. The drag acting on cars, aircraft and nautical vessels is controlled by turbulent boundary layers, and the design of efficient internal combustion engines strongly relies on the turbulent mixing of fuel and oxidizer, to name but a few examples.

The non-linear nature of turbulence gives rise to an enormous range of length and time scales. The Reynolds number estimates the ratio of the length scale $\mathcal{L}$ associated with the largest structures in the flow field and the length scale η_K, i.e., the Kolmogorov scale, related to the smallest ones as $\mathcal{L}/\eta_K \sim \mathrm{Re}^{\frac{3}{4}}$. Until today, this dependency renders Direct Numerical Simulation (DNS), which aims at resolving all features down to the smallest scales, infeasible for all but the simplest turbulent flows. Thus, with DNS being ruled out, a certain level of modeling will become unavoidable. In contrast to DNS, for instance, approaches based on the Reynolds-Averaged Navier–Stokes (RANS) equations merely compute the statistical averages; that is, the time-averaged non-turbulent mean flow, leaving all turbulent features to a model. However, Kolmogorov's hypothesis of local isotropy (see [128]), i.e, the flow-independence of the smaller scales, suggests restricting the modeling effort to these scales only. The universal character of the smaller scales can be considered as the basis of an alternative approach to the numerical simulation of turbulent flows, that is, Large-Eddy Simulation (LES). By computing the larger flow-dependent structures and modeling the impact of the smaller ones on their evolution, LES can be

Published online: 27 February 2017

categorized in between DNS and RANS modeling. As a result, the cost of LES is significantly reduced compared to DNS, while the necessary degree of modeling is kept notably lower than for RANS approaches.

The Variational Multiscale Method (VMM) was introduced for the first time about 20 years ago in [106] and further developed as a general framework for computational mechanics in [107]. It aims at problems with broad scale ranges, which typically pose an enormous challenge for standard numerical methods. When applying the VMM, the scales of the underlying problem are separated into a predefined number of scale groups. This scale separation opens a door for a different numerical treatment of each of these predefined scale groups and allows for designing advanced computational methods. A categorization of the VMM into the broad field of multiscale methods, taking into account applications both in fluid as well as in solid mechanics, may be found, e.g., in the overview article [86].

Aside from various other applications, as aforementioned, the theoretical framework of the VMM was also extended to the incompressible Navier–Stokes equations with a view to turbulent flow in [110]. Thus, the foundations for generating a new approach to LES were laid. In the past 15 years, the VMM for LES has evolved into a frequently used and comprehensive approach to numerically investigating turbulent flows. In fact, it has not only shown very good performance for classical benchmark examples such as homogeneous isotropic turbulent flow in a box and turbulent channel flow, but also demonstrated its applicability for robust and accurate numerical simulation of complex engineering and biomedical flow. For instance, the aerodynamics of wind turbines were analyzed in [105], flow-control applications to a realistic wing design were reported in [176], multi-ion transport in dilute electrolyte solutions under turbulent flow conditions in [8] and pulsatile turbulent flow in the upper and lower pulmonary airways in [53].

With respect to the aforementioned predefined number of scale groups, VMMs for LES are usually categorized into two- and three-scale approaches. In two-scale approaches, resolved and unresolved scales are distinguished, whereas in three-scale approaches, the resolved scales are further differentiated in that the larger and smaller ones of these resolved scales are separated. For instance, the recent review in [1] is guided by this classification. Here, in contrast to that, we follow a different categorization based on the one introduced in [188]: (i) Implicit LES (ILES), here represented by residual-based and stabilized methods, (ii) functional subgrid-scale modeling via small-scale subgrid-viscosity models and (iii) structural subgrid-scale modeling, which has so far merely been realized via the introduction of multifractal subgrid scales.

This review does not only focus on LES of turbulent incompressible flow, but also aims at covering further aspects of numerically simulating turbulent flow as well as applications beyond incompressible single-phase flow. This is one of the aspects setting it apart from all reviews on the VMM for LES published earlier in [1, 80, 118]. An important aspect for LES of wall-bounded turbulent flow at very high Reynolds number is wall-layer modeling, which will be addressed in this article. As concerns further complexities introduced into turbulent flows, passive and active scalar transport will be considered. Moreover, developments for LES of turbulent two-phase flow and combustion will likewise be covered briefly.

The remainder of the present review article is organized as follows: In Sect. 2, the incompressible Navier–Stokes equations are introduced, and the fundamental concepts of LES as well as traditional approaches are outlined. The variational multiscale formulation of the incompressible Navier–Stokes equations is derived in Sect. 3. Residual-Based VMMs (RBVMMs) are addressed in Sect. 4. Section 5 provides an overview of VMMs with small-scale subgrid-viscosity modeling. In Sect. 6, a VMM for which the subgrid-scales are explicitly estimated from a multifractal modeling procedure is shown. Section 7 juxtaposes the various VMMs presented in Sects. 4–6. Developments towards wall-layer modeling in the context of the VMM are compiled in Sect. 8. In Sects. 9, extensions of the VMMs introduced in Sects. 4–6 to passive and active scalar transport are presented. Section 10 addresses the application of VMMs to LES of turbulent two-phase flow and combustion. A brief summary and outlook in Sect. 11 concludes this review article.

2 Large-Eddy Simulation

In the field of LES, extensive research has been performed in the past more than five decades since the publication of the Smagorinsky subgrid-scale model in [196]. As a result, LES has found its way into a wide variety of fluid mechanical applications. In the following, we only briefly summarize the traditional concepts of LES and related subgrid-scale modeling strategies. Comprehensive insights into the historical aspects, practical issues as well as the related physical and mathematical theory may be obtained from various review articles such as [66, 71, 95, 138, 153, 167, 185] as well as textbooks such as [14, 75, 117, 188].

2.1 Problem Statement: The Navier–Stokes Equations

Turbulent flow in the domain Ω is governed by the Navier–Stokes equations. The incompressible Navier–Stokes

equations, comprising momentum conservation and continuity equation, are given by

$$\frac{\partial \mathbf{u}}{\partial t} + \nabla \cdot (\mathbf{u} \otimes \mathbf{u}) + \nabla p_{\text{kin}} - 2\nu \nabla \cdot \boldsymbol{\varepsilon}(\mathbf{u}) = \mathbf{f} \quad \text{in } \Omega, \tag{1}$$

$$\nabla \cdot \mathbf{u} = 0 \quad \text{in } \Omega, \tag{2}$$

where $\mathbf{u}(\mathbf{x}, t) = (u_1(\mathbf{x}, t), u_2(\mathbf{x}, t), u_3(\mathbf{x}, t))^{\text{T}}$ denotes the velocity vector, $p_{\text{kin}}(\mathbf{x}, t)$ the kinematic pressure, imposing the divergence-free constraint, and ν the kinematic viscosity, assumed constant. The rate-of-deformation tensor $\boldsymbol{\varepsilon}(\mathbf{u})$ is defined as

$$\boldsymbol{\varepsilon}(\mathbf{u}) = \frac{1}{2}\left(\nabla \mathbf{u} + (\nabla \mathbf{u})^{\text{T}}\right). \tag{3}$$

Moreover, a potential volume force is denoted by $\mathbf{f}$, but omitted in the remainder of this section. Both the conservative form $\nabla \cdot (\mathbf{u} \otimes \mathbf{u})$ of the convective term of the momentum equation (1) as well as the alternative convective form $\mathbf{u} \cdot \nabla \mathbf{u}$ will be used below.

Furthermore, boundary conditions on the boundary $\partial\Omega$ of the domain Ω are defined as follows:

$$\mathbf{u} = \mathbf{u}_{\text{D}} \quad \text{on } \Gamma_{\text{D},\mathbf{u}}, \tag{4}$$

$$-\mathbf{u}(\mathbf{u} \cdot \mathbf{n}) + \left(-p_{\text{kin}}\mathbf{I} + 2\nu\boldsymbol{\varepsilon}(\mathbf{u})\right) \cdot \mathbf{n} = \mathbf{h}_{\mathbf{u}} \quad \text{on } \Gamma^{\text{in}}_{\text{N},\mathbf{u}}, \tag{5}$$

$$\left(-p_{\text{kin}}\mathbf{I} + 2\nu\boldsymbol{\varepsilon}(\mathbf{u})\right) \cdot \mathbf{n} = \mathbf{h}_{\mathbf{u}} \quad \text{on } \Gamma^{\text{out}}_{\text{N},\mathbf{u}}, \tag{6}$$

where $\mathbf{I}$ is the identity tensor and $\mathbf{n}$ the outer unit normal vector on $\partial\Omega$. Dirichlet boundary conditions are enforced on the part $\Gamma_{\text{D},\mathbf{u}}$ of $\partial\Omega$ and Neumann boundary conditions on $\Gamma_{\text{N},\mathbf{u}}$. It is assumed that $\Gamma_{\text{D},\mathbf{u}} \cap \Gamma_{\text{N},\mathbf{u}} = \emptyset$ and $\Gamma_{\text{D},\mathbf{u}} \cup \Gamma_{\text{N},\mathbf{u}} = \partial\Omega$. Neumann boundary conditions are prescribed differently on in- and outflow parts of the Neumann boundary. The total momentum flux is specified on a potential inflow part $\Gamma^{\text{in}}_{\text{N},\mathbf{u}}(t) = \{\mathbf{x} \in \Gamma_{\text{N},\mathbf{u}} | \mathbf{u}(\mathbf{x}, t) \cdot \mathbf{n}(\mathbf{x}) < 0\}$, but only the traction on the outflow part $\Gamma^{\text{out}}_{\text{N},\mathbf{u}}(t) = \{\mathbf{x} \in \Gamma_{\text{N},\mathbf{u}} | \mathbf{u}(\mathbf{x}, t) \cdot \mathbf{n}(\mathbf{x}) \geqslant 0\}$, with $\Gamma^{\text{out}}_{\text{N},\mathbf{u}} \cap \Gamma^{\text{in}}_{\text{N},\mathbf{u}} = \emptyset$ and $\Gamma^{\text{out}}_{\text{N},\mathbf{u}} \cup \Gamma^{\text{in}}_{\text{N},\mathbf{u}} = \Gamma_{\text{N},\mathbf{u}}$; see, e.g., [82, 109, 112]. The Neumann boundary condition is split up this way owing to potentially arising eddies at the outflow boundary, which may evoke (partial) inflow at the outlet. The incorporation of the resulting convective boundary term at the outlet of the domain is mandatory for ensuring stability at the outflow boundary in such cases, meaning that potential eddies are indeed convected out of the domain, as observed, e.g., in [11, 87]. Finally, the initial condition is given by

$$\mathbf{u} = \mathbf{u}_0 \quad \text{in } \Omega, \tag{7}$$

with a velocity field $\mathbf{u}_0$ assumed to be divergence-free.

2.2 The Filtered Navier–Stokes Equations

In LES, merely the evolution of the larger, problem-dependent scales is computed. To eliminate the smaller and more universal scales, a spatial low-pass filtering operation, which is expressed as a convolution of the velocity field with a filter kernel G subject to

$$\bar{\mathbf{u}}(\mathbf{x}, t) = \int G(\mathbf{x} - \check{\mathbf{x}})\mathbf{u}(\check{\mathbf{x}}, t)\mathrm{d}\check{\mathbf{x}}, \tag{8}$$

is (traditionally) applied, as proposed in [137]. The filter kernel G is assumed homogeneous with normalization $\int G(\mathbf{x})\mathrm{d}\mathbf{x} = 1$. The resolved large-scale part is denoted by $\bar{(\cdot)}$, and the unresolved subfilter-scale part, marked by $(\cdot)''$, is obtained as

$$\mathbf{u}'' = \mathbf{u} - \bar{\mathbf{u}}. \tag{9}$$

Applying the filtering operation to the Navier–Stokes equations (1) and (2) and assuming commutation with derivative operators, the filtered Navier–Stokes equations, governing the evolution of the resolved scales, take the form

$$\frac{\partial \bar{\mathbf{u}}}{\partial t} + \nabla \cdot (\bar{\mathbf{u}} \otimes \bar{\mathbf{u}}) + \nabla \bar{p}_{\text{kin}} - 2\nu \nabla \cdot \boldsymbol{\varepsilon}(\bar{\mathbf{u}}) = -\nabla \cdot \boldsymbol{\tau}_{\text{sfs}}, \tag{10}$$

$$\nabla \cdot \bar{\mathbf{u}} = 0, \tag{11}$$

where the subfilter-scale stress tensor $\boldsymbol{\tau}_{\text{sfs}}$ is defined as

$$\boldsymbol{\tau}_{\text{sfs}} = \overline{\mathbf{u} \otimes \mathbf{u}} - \bar{\mathbf{u}} \otimes \bar{\mathbf{u}}. \tag{12}$$

According to [137], the subfilter-scale stress tensor $\boldsymbol{\tau}_{\text{sfs}}$ can be decomposed into two parts. The first part, termed Leonard-stress tensor, is given by

$$\boldsymbol{\tau}_{\text{L}} = \overline{\bar{\mathbf{u}} \otimes \bar{\mathbf{u}}} - \bar{\mathbf{u}} \otimes \bar{\mathbf{u}} \tag{13}$$

and comprises all terms which can be computed from the known filtered solution. The second part

$$\boldsymbol{\tau}^*_{\text{sfs}} = \overline{\bar{\mathbf{u}} \otimes \mathbf{u}''} + \overline{\mathbf{u}'' \otimes \bar{\mathbf{u}}} + \overline{\mathbf{u}'' \otimes \mathbf{u}''} \tag{14}$$

contains the subfilter scales and is further split into cross-stress tensor $\boldsymbol{\tau}_{\text{C}}$ and subfilter-scale Reynolds-stress tensor $\boldsymbol{\tau}_{\text{R}}$ as

$$\boldsymbol{\tau}_{\text{C}} = \overline{\bar{\mathbf{u}} \otimes \mathbf{u}''} + \overline{\mathbf{u}'' \otimes \bar{\mathbf{u}}}, \tag{15}$$

$$\boldsymbol{\tau}_{\text{R}} = \overline{\mathbf{u}'' \otimes \mathbf{u}''}. \tag{16}$$

However, the filtered momentum equation is not closed, since $\boldsymbol{\tau}^*_{\text{sfs}}$ is not exclusively defined in terms of the resolved velocity field. Closure is achieved by modeling the impact of the subfilter scales on the basis of the information contained in the resolved scales only. By including the Leonard-stress tensor into the non-linear term, an alternative form of the filtered momentum equation is obtained, which reads

$$\frac{\partial \bar{\mathbf{u}}}{\partial t} + \nabla \cdot \left(\overline{\bar{\mathbf{u}} \otimes \bar{\mathbf{u}}} \right) + \nabla \bar{p}_{\text{kin}} - 2\nu \nabla \cdot \boldsymbol{\varepsilon}(\bar{\mathbf{u}}) = -\nabla \cdot \boldsymbol{\tau}^*_{\text{sfs}}. \quad (17)$$

For this strategy based on an analytical filter, called explicit filtering, filtering and subfilter-scale modeling are assumed independent of the subsequent discretization of the filtered governing equation system. As a result, the numerical scheme has to ensure an accurate solution of the filtered equations. An alternative approach consists of taking the cumulative effect of the numerical treatment of the governing equations, in particular, the introduction of a computational grid and the application of discrete approximations of the derivative operators inherent in every flow simulation as an implicit filtering leading to the large-scale field. In this case, as discussed, e.g., in [190], the consideration of the alternative form (17) of the filtered momentum equation appears to be more appropriate, since the form $\bar{\mathbf{u}} \otimes \bar{\mathbf{u}}$ of the convective term gives rise to unresolved scales which are truncated by the implicit filter, inevitably resulting in $\overline{\bar{\mathbf{u}} \otimes \bar{\mathbf{u}}}$. In the context of implicit filtering, it is also more appropriate to refer to the unresolved scales as the subgrid scales rather than the subfilter scales and to the subfilter-scale stress tensor as the subgrid-scale stress tensor $\boldsymbol{\tau}^*_{\text{sgs}}$ (and $\boldsymbol{\tau}_{\text{sgs}}$, respectively). With regard to the subsequent application of the VMM, this notation is adopted for the remainder of the present paper.

2.3 Fundamental Subgrid-Scale-Modeling Strategies

According to [188], two modeling strategies are usually distinguished in LES. Functional models, on the one hand, intend to model only the impact of the subgrid scales onto the evolution of the resolved scales, but not necessarily their structure. In the mean, they act dissipatively, removing energy from the resolved scales. The subgrid-viscosity concept builds on the assumption that the involved mechanisms exhibit a behavior similar to the dissipation by molecular motion. A general expression for the deviatoric part of the subgrid-scale stress tensor thus reads as

$$\boldsymbol{\tau}_{\text{sgs}} - \frac{1}{3}\text{tr}(\boldsymbol{\tau}_{\text{sgs}})\mathbf{I} = -2\nu_{\text{sgs}}\boldsymbol{\varepsilon}(\bar{\mathbf{u}}), \quad (18)$$

where ν_{sgs} denotes the subgrid viscosity. The Smagorinsky model [196], introduced in the 1960s, is among the most popular subgrid-viscosity models. To date, various modifications and enhancements have been developed, such as its dynamic form proposed in [73] to adapt the involved model parameter to local flow structures. The underlying concept, which is based on the so-called Germano identity [72], evolved into a comprehensive procedure to determine otherwise tunable model parameters and was recently reviewed in [149]. However, subgrid-viscosity models inherently rely on the assumption that the subgrid-scale stress tensor is aligned with the resolved strain-rate tensor. Indeed, the actual subgrid-scale stress tensor and the strain-rate tensor are merely weakly correlated; see, e.g., [143]. Moreover, by definition, subgrid-viscosity models do not intend to recover the phenomenon of inverse energy transfer from the subgrid scales to the resolved scales. Although energy is transferred to the subgrid scales on average, backscatter can be quite significant and of the same magnitude as forward scatter; see, e.g., [170].

On the other hand, structural models aim at reconstructing the subgrid-scale stress tensor directly, making use of information extracted from the resolved velocity field. By exploiting the similarity between the scales of adjacent ranges, Bardina's scale-similarity model [6, 7] estimates the subgrid-scale stress tensor from its definition as

$$\boldsymbol{\tau}_{\text{sgs}} \sim \overline{\bar{\mathbf{u}} \otimes \bar{\mathbf{u}}} - \bar{\bar{\mathbf{u}}} \otimes \bar{\bar{\mathbf{u}}}. \quad (19)$$

In general, scale invariance, which also enters the dynamic form of the Smagorinsky model mentioned above, constitutes a particularly important property for subgrid-scale modeling in LES, as pointed out in [150]. Bardina's scale-similarity model may also be categorized as a particular case of the general class of deconvolution-type models. Deconvolution-type models, such as the approximate deconvolution model originally introduced in [204], use an approximate inverse of the filtering operator to obtain information on the unresolved scales. Models of this category display a notably high level of correlation with the actual subgrid-scale stress tensor. Furthermore, forward scatter as well as backscatter of energy are captured naturally via the non-linear interactions retained by structural approaches. However, these models often do not supply sufficient subgrid-scale dissipation. This aspect is particularly discussed in [56]. Both physically and mathematically motivated approaches have been proposed to adequately capture the missing subgrid-scale dissipation; see, e.g., [70] for an overview. In the case of the scale-similarity model, an additional subgrid-viscosity term is frequently included, leading to a so-called mixed model; see, e.g., [6, 7, 222]. Other structural models, such as the velocity-estimation model (see [57]), explicitly approximate the subgrid-scale velocity.

The aforementioned subgrid-scale models seek for a proper approximation of the unclosed terms and are thus referred to as explicit subgrid-scale models. In contrast, ILES, as proposed in [17], assumes that the numerical dissipation contained within the discrete scheme is able to take the effect of the unresolved scales into account, thereby relying on the assumption that the effect of the subgrid scales is dissipative in the mean, similar to functional models. For instance, an advanced form of

an ILES, called Adaptive Local Deconvolution Method (ALDM), was introduced in [104].

3 The Variational Multiscale Method

Originally, the VMM was introduced in [106] to explain the origins of stabilized methods, as used in the Finite Element Method (FEM), by relating them to subgrid-scale models in general. Following its origin, most of the research on VMMs for LES has been conducted within the FEM. Therefore, the respective notations are almost exclusively adopted here. However, it is emphasized that the VMM constitutes a theoretical framework for LES not specifically related to the FEM, let alone restricted to it. In fact, the VMM can also be used as a framework within other numerical methods. This issue was comprehensively discussed in [80] with a focus on the Finite Volume Method (FVM), besides the FEM. FVM-based methods may be found, e.g., in [38, 79]. Furthermore, approaches as well as references regarding Finite Difference Methods (FDMs) and spectral methods were provided in [80]. In the following, the VMM is first related to the concepts of traditional LES, then a two- and a three-scale formulation are introduced.

3.1 A Paradigm for Scale Separation in Large-Eddy Simulation

The variational multiscale concept offers a different perspective on the fundamental step of scale separation in LES. In the VMM, scale separation based on a variational projection of the governing equations is assumed. The variational projection, identifying the resolved and subgrid scales, emanates from the discretization of the governing equations by a numerical method well suited for discretizing those equations appropriately, for instance, the FEM. The reader is referred, e.g., to [92] for an exhaustive discussion regarding the Galerkin FEM and its mathematical interpretation as a projection. VMMs for LES are therefore inherently linked with approaches assuming implicit filtering. Although filtering might not be applied explicitly, the filtered formulation, displayed in Sect. 2.2, frequently serves as an analytical tool for devising and evaluating approaches to LES. Specifically for this case, the VMM enables a profound mathematical framework for LES. Owing to implicit filtering, the VMM can be straightforwardly applied to arbitrary complex geometries. Furthermore, the VMM allows for a priori separating an arbitrary number of scale ranges and provides an equation for each scale range, describing the evolution of the respective scales; see, e.g., [51, 80]. By augmenting the number of separated scale groups beyond the established two-scale decomposition used in LES, more advanced multilevel LES approaches may be derived consistently; see [190] for a categorization of multilevel methods in general as well as a compilation of various concepts. This opportunity gives further evidence of the multi-purpose framework enabled by the VMM.

3.2 Variational Formulation of the Incompressible Navier–Stokes Equations

For the variational formulation of the Navier–Stokes equations, appropriate solution function spaces $\mathcal{S}_{\mathbf{u}}$ for $\mathbf{u}$ and $\mathcal{S}_p$ for p_{kin} as well as weighting function spaces $\mathcal{V}_{\mathbf{u}}$ for the velocity weighting function $\mathbf{v}$ and $\mathcal{V}_p$ for the pressure weighting function q are assumed. The system of Eqs. (1) (in convective form) and (2) is multiplied by $\mathbf{v} \in \mathcal{V}_{\mathbf{u}}$ and $q \in \mathcal{V}_p$ and integrated over the domain Ω. Viscous and pressure term are integrated by parts, with boundary conditions (4) as well as (5) and (6) applied to the resulting boundary integrals.

The variational formulation of the incompressible Navier–Stokes equations is given as follows: find $(\mathbf{u}, p_{\mathrm{kin}}) \in \mathcal{S}_{\mathbf{u}} \times \mathcal{S}_p$ such that

$$\mathcal{B}_{\mathrm{NS}}(\mathbf{v}, q; \mathbf{u}, p_{\mathrm{kin}}) = \ell_{\mathrm{NS}}(\mathbf{v}) \tag{20}$$

for all $(\mathbf{v}, q) \in \mathcal{V}_{\mathbf{u}} \times \mathcal{V}_p$. The form on the left-hand side is defined as

$$\mathcal{B}_{\mathrm{NS}}(\mathbf{v}, q; \mathbf{u}, p_{\mathrm{kin}}) := \mathcal{B}_{\mathrm{M}}(\mathbf{v}; \mathbf{u}, p_{\mathrm{kin}}) + \mathcal{B}_{\mathrm{C}}(q; \mathbf{u}), \tag{21}$$

with the momentum part

$$\begin{aligned} \mathcal{B}_{\mathrm{M}}(\mathbf{v}; \mathbf{u}, p_{\mathrm{kin}}) := \\ \left(\mathbf{v}, \tfrac{\partial \mathbf{u}}{\partial t}\right)_{\Omega} + (\mathbf{v}, \mathbf{u} \cdot \nabla \mathbf{u})_{\Omega} - \left(\nabla \cdot \mathbf{v}, p_{\mathrm{kin}}\right)_{\Omega} \\ + (\boldsymbol{\varepsilon}(\mathbf{v}), 2\nu\boldsymbol{\varepsilon}(\mathbf{u}))_{\Omega} - (\mathbf{v}, \mathbf{u}(\mathbf{u} \cdot \mathbf{n}))_{\Gamma_{\mathrm{N},\mathbf{u}}^{\mathrm{in}}} \end{aligned} \tag{22}$$

and the continuity part

$$\mathcal{B}_{\mathrm{C}}(q; \mathbf{u}) := (q, \nabla \cdot \mathbf{u})_{\Omega}. \tag{23}$$

The linear form $\ell_{\mathrm{NS}}(\mathbf{v})$ on the right-hand side is given as

$$\ell_{\mathrm{NS}}(\mathbf{v}) := (\mathbf{v}, \mathbf{f})_{\Omega} + \left(\mathbf{v}, \mathbf{h}_{\mathbf{u}}\right)_{\Gamma_{\mathrm{N},\mathbf{u}}} \tag{24}$$

and includes the Neumann boundary condition. The last term of the momentum part arises due to the aforementioned inflow part of the Neumann boundary condition (5). Since this term is not subject to the following scale separation, it will be omitted in the subsequent derivations for brevity. Here, $(\cdot,\cdot)_{\Omega}$ and $(\cdot,\cdot)_{\Gamma}$ denote the usual L_2-inner product in a domain Ω and on a boundary Γ, which may be further specified by additional sub- or superscripts.

3.3 Two-Scale Decomposition

For the basic variant of the variational multiscale formulation of the Navier–Stokes equations, the velocity is decomposed into resolved and unresolved (or subgrid) components as

$$\mathbf{u} = \mathbf{u}^h + \hat{\mathbf{u}}, \tag{25}$$

where resolved velocity scales are identified by $(\cdot)^h$ related to a spatial discretization of characteristic element length h. The subgrid scales are denoted by $\hat{(\cdot)}$. Analogously, the pressure is decomposed as

$$p_{\text{kin}} = p^h_{\text{kin}} + \hat{p}_{\text{kin}}. \tag{26}$$

According to the decomposition of the solution functions, direct sum decompositions of the underlying function spaces into a finite-dimensional subspace of resolved scales and an infinite-dimensional subspace of unresolved scales in the form $\mathcal{S}_{\mathbf{u}} = \mathcal{S}^h_{\mathbf{u}} \oplus \hat{\mathcal{S}}_{\mathbf{u}}$ and $\mathcal{S}_p = \mathcal{S}^h_p \oplus \hat{\mathcal{S}}_p$, respectively, are assumed. Inserting the decomposition of velocity and pressure, (25) and (26), into the variational formulation (20) leads to

$$\begin{aligned} &\mathcal{B}_{\text{NS}}(\mathbf{v}, q; \mathbf{u}^h, p^h_{\text{kin}}) \\ &\quad + \mathcal{B}^1_{\text{NS}}(\mathbf{v}, q; \mathbf{u}^h, \hat{\mathbf{u}}, \hat{p}_{\text{kin}}) + \mathcal{B}^2_{\text{NS}}(\mathbf{v}; \hat{\mathbf{u}}) = \\ &\quad \ell_{\text{NS}}(\mathbf{v}), \end{aligned} \tag{27}$$

where

$$\begin{aligned} &\mathcal{B}^1_{\text{NS}}(\mathbf{v}, q; \mathbf{u}^h, \hat{\mathbf{u}}, \hat{p}_{\text{kin}}) := \\ &\left(\mathbf{v}, \tfrac{\partial \hat{\mathbf{u}}}{\partial t}\right)_\Omega + \left(\mathbf{v}, \mathbf{u}^h \cdot \nabla \hat{\mathbf{u}} + \hat{\mathbf{u}} \cdot \nabla \mathbf{u}^h\right)_\Omega \\ &- \left(\nabla \cdot \mathbf{v}, \hat{p}_{\text{kin}}\right)_\Omega + (\boldsymbol{\varepsilon}(\mathbf{v}), 2\nu\boldsymbol{\varepsilon}(\hat{\mathbf{u}}))_\Omega + (q, \nabla \cdot \hat{\mathbf{u}})_\Omega \end{aligned} \tag{28}$$

contains linear terms in the unresolved-scale quantities. The quadratic contribution from the convective term is given by

$$\mathcal{B}^2_{\text{NS}}(\mathbf{v}; \hat{\mathbf{u}}) := (\mathbf{v}, \hat{\mathbf{u}} \cdot \nabla \hat{\mathbf{u}})_\Omega. \tag{29}$$

For separating resolved and unresolved scales via a variational projection, direct sum decompositions of the weighting function spaces $\mathcal{V}_{\mathbf{u}} = \mathcal{V}^h_{\mathbf{u}} \oplus \hat{\mathcal{V}}_{\mathbf{u}}$ and $\mathcal{V}_p = \mathcal{V}^h_p \oplus \hat{\mathcal{V}}_p$, respectively, are also introduced. Accordingly, the weighting functions read as

$$\mathbf{v} = \mathbf{v}^h + \hat{\mathbf{v}}, \tag{30}$$

$$q = q^h + \hat{q}, \tag{31}$$

respectively. By this decomposition, the variational form of the Navier–Stokes equations is decoupled into a resolved- and an unresolved-scale equation, that is, variational form (27) is separately weighted by the resolved- and the unresolved-scale part of the decomposed weighting functions. The equation projected onto the space of resolved scales reads as

$$\begin{aligned} &\mathcal{B}_{\text{NS}}(\mathbf{v}^h, q^h; \mathbf{u}^h, p^h_{\text{kin}}) \\ &+ \mathcal{B}^1_{\text{NS}}(\mathbf{v}^h, q^h; \mathbf{u}^h, \hat{\mathbf{u}}, \hat{p}_{\text{kin}}) + \mathcal{B}^2_{\text{NS}}(\mathbf{v}^h; \hat{\mathbf{u}}) = \\ &\ell_{\text{NS}}(\mathbf{v}^h) \end{aligned} \tag{32}$$

for all $(\mathbf{v}^h, q^h) \in \mathcal{V}^h_{\mathbf{u}} \times \mathcal{V}^h_p$ and the equation projected onto the space of unresolved scales as

$$\begin{aligned} &\mathcal{B}_{\text{NS}}(\hat{\mathbf{v}}, \hat{q}; \mathbf{u}^h, p^h_{\text{kin}}) \\ &+ \mathcal{B}^1_{\text{NS}}(\hat{\mathbf{v}}, \hat{q}; \mathbf{u}^h, \hat{\mathbf{u}}, \hat{p}_{\text{kin}}) + \mathcal{B}^2_{\text{NS}}(\hat{\mathbf{v}}; \hat{\mathbf{u}}) = \\ &\ell_{\text{NS}}(\hat{\mathbf{v}}) \end{aligned} \tag{33}$$

for all $(\hat{\mathbf{v}}, \hat{q}) \in \hat{\mathcal{V}}_{\mathbf{u}} \times \hat{\mathcal{V}}_p$. The resolved-scale equation is solved for $(\mathbf{u}^h, p^h_{\text{kin}}) \in \mathcal{S}^h_{\mathbf{u}} \times \mathcal{S}^h_p$, while the unresolved-scale equation, yielding $(\hat{\mathbf{u}}, \hat{p}_{\text{kin}}) \in \hat{\mathcal{S}}_{\mathbf{u}} \times \hat{\mathcal{S}}_p$, is usually omitted. Hence, the resolved-scale equation is not closed, and the unresolved-scale contributions have to be appropriately modeled. Eventually, the variational multiscale formulation (32) is split up as follows:

$$\begin{aligned} &\mathcal{B}_{\text{NS}}(\mathbf{v}^h, q^h; \mathbf{u}^h, p^h_{\text{kin}}) + \mathcal{C}(\mathbf{v}^h; \mathbf{u}^h, \hat{\mathbf{u}}) + \mathcal{R}(\mathbf{v}^h; \hat{\mathbf{u}}) \\ &+ \mathcal{B}^{1,\text{lin}}_{\text{NS}}(\mathbf{v}^h, q^h; \hat{\mathbf{u}}, \hat{p}_{\text{kin}}) = \\ &\ell_{\text{NS}}(\mathbf{v}^h), \end{aligned} \tag{34}$$

where

$$\begin{aligned} &\mathcal{C}(\mathbf{v}^h; \mathbf{u}^h, \hat{\mathbf{u}}) := \left(\mathbf{v}^h, \mathbf{u}^h \cdot \nabla \hat{\mathbf{u}} + \hat{\mathbf{u}} \cdot \nabla \mathbf{u}^h\right)_\Omega = \\ &\left(\mathbf{v}^h, \mathbf{u}^h \cdot \nabla \hat{\mathbf{u}}\right)_\Omega + \left(\mathbf{v}^h, \hat{\mathbf{u}} \cdot \nabla \mathbf{u}^h\right)_\Omega \end{aligned} \tag{35}$$

is the projection of the cross-stress tensor and

$$\mathcal{R}(\mathbf{v}^h; \hat{\mathbf{u}}) := \mathcal{B}^2_{\text{NS}}(\mathbf{v}^h; \hat{\mathbf{u}}) = \left(\mathbf{v}^h, \hat{\mathbf{u}} \cdot \nabla \hat{\mathbf{u}}\right)_\Omega \tag{36}$$

the projection of the subgrid-scale Reynolds-stress tensor onto the space of resolved scales. The form

$$\begin{aligned} &\mathcal{B}^{1,\text{lin}}_{\text{NS}}(\mathbf{v}^h, q^h; \hat{\mathbf{u}}, \hat{p}_{\text{kin}}) := \\ &\left(\mathbf{v}^h, \tfrac{\partial \hat{\mathbf{u}}}{\partial t}\right)_\Omega - \left(\nabla \cdot \mathbf{v}^h, \hat{p}_{\text{kin}}\right)_\Omega \\ &+ \left(\boldsymbol{\varepsilon}(\mathbf{v}^h), 2\nu\boldsymbol{\varepsilon}(\hat{\mathbf{u}})\right)_\Omega + \left(q^h, \nabla \cdot \hat{\mathbf{u}}\right)_\Omega \end{aligned} \tag{37}$$

contains the remaining linear terms in the unresolved-scale quantities. The variational multiscale formulation (34) represents an analogue to the filtered Navier–Stokes equations and provides an alternative mathematical framework for LES. Converting the particularly relevant convective term as well as the cross- and subgrid-scale Reynolds-stress terms of the variational multiscale formulation into their respective filter-based form leads to $\overline{\bar{\mathbf{u}} \cdot \nabla \bar{\mathbf{u}}}$, $\overline{\bar{\mathbf{u}} \cdot \nabla \mathbf{u}''} + \overline{\mathbf{u}'' \cdot \nabla \bar{\mathbf{u}}}$ and $\overline{\mathbf{u}'' \cdot \nabla \mathbf{u}''}$, respectively. These filtered terms may be compared to their counterparts in Eq. (17). The filtered form, given in Eq. (17) and specifically suggested for implicit filtering, is thus obtained naturally, with the important difference that the assumption of commutation between partial derivatives and filter operation is not required (see also, e.g., [51, 214]).

3.4 Three-Scale Decomposition

For a three-scale decomposition, the variables are further split up into three scale groups, larger resolved, smaller resolved and unresolved scales. That is, velocity and pressure solution and weighting functions are decomposed as follows:

$$\mathbf{u} = \underbrace{\overline{\mathbf{u}}^h + \mathbf{u}'^h}_{\mathbf{u}^h} + \hat{\mathbf{u}}, \tag{38}$$

$$p_{\mathrm{kin}} = \underbrace{\overline{p}^h_{\mathrm{kin}} + p'^h_{\mathrm{kin}}}_{p^h_{\mathrm{kin}}} + \hat{p}_{\mathrm{kin}}, \tag{39}$$

$$\mathbf{v} = \underbrace{\overline{\mathbf{v}}^h + \mathbf{v}'^h}_{\mathbf{v}^h} + \hat{\mathbf{v}}, \tag{40}$$

$$q = \underbrace{\overline{q}^h + q'^h}_{q^h} + \hat{q}. \tag{41}$$

These decompositions are in accordance with direct sum decompositions of the underlying function spaces into finite-dimensional subspaces of larger and smaller resolved scales and an infinite-dimensional subspace of unresolved scales: $\mathcal{S}_{\mathbf{u}_h} = \overline{\mathcal{S}}^h_{\mathbf{u}} \oplus \mathcal{S}'^h_{\mathbf{u}} \oplus \hat{\mathcal{S}}_{\mathbf{u}}$, $\mathcal{S}_{p_h} = \overline{\mathcal{S}}^h_{p} \oplus \mathcal{S}'^h_{p} \oplus \hat{\mathcal{S}}_{p}$ as well as $\mathcal{V}_{\mathbf{u}} = \overline{\mathcal{V}}^h_{\mathbf{u}} \oplus \mathcal{V}'^h_{\mathbf{u}} \oplus \hat{\mathcal{V}}_{\mathbf{u}}$, $\mathcal{V}_p = \overline{\mathcal{V}}^h_{p} \oplus \mathcal{V}'^h_{p} \oplus \hat{\mathcal{V}}_{p}$.

The three-scale decomposition allows for replacing the resolved-scale equation (32) by two equations, an equation projected onto the space of larger resolved scales,

$$\begin{aligned} &\mathcal{B}_{\mathrm{NS}}(\overline{\mathbf{v}}^h, \overline{q}^h; \mathbf{u}^h, p^h_{\mathrm{kin}}) \\ &+ \mathcal{B}^1_{\mathrm{NS}}(\overline{\mathbf{v}}^h, \overline{q}^h; \mathbf{u}^h, \hat{\mathbf{u}}, \hat{p}_{\mathrm{kin}}) + \mathcal{B}^2_{\mathrm{NS}}(\overline{\mathbf{v}}^h; \hat{\mathbf{u}}) \\ &= \ell_{\mathrm{NS}}(\overline{\mathbf{v}}^h) \end{aligned} \tag{42}$$

for all $(\overline{\mathbf{v}}^h, \overline{q}^h) \in \overline{\mathcal{V}}^h_{\mathbf{u}} \times \overline{\mathcal{V}}^h_{p}$, which is solved for $(\overline{\mathbf{u}}^h, \overline{p}^h_{\mathrm{kin}}) \in \overline{\mathcal{S}}^h_{\mathbf{u}} \times \overline{\mathcal{S}}^h_{p}$, and an equation projected onto the space of smaller resolved scales,

$$\begin{aligned} &\mathcal{B}_{\mathrm{NS}}(\mathbf{v}'^h, q'^h; \mathbf{u}^h, p^h_{\mathrm{kin}}) \\ &+ \mathcal{B}^1_{\mathrm{NS}}(\mathbf{v}'^h, q'^h; \mathbf{u}^h, \hat{\mathbf{u}}, \hat{p}_{\mathrm{kin}}) + \mathcal{B}^2_{\mathrm{NS}}(\mathbf{v}'^h; \hat{\mathbf{u}}) \\ &= \ell_{\mathrm{NS}}(\mathbf{v}'^h) \end{aligned} \tag{43}$$

for all $(\mathbf{v}'^h, q'^h) \in \mathcal{V}'^h_{\mathbf{u}} \times \mathcal{V}'^h_{p}$, which determines $(\mathbf{u}'^h, p'^h_{\mathrm{kin}}) \in \mathcal{S}'^h_{\mathbf{u}} \times \mathcal{S}'^h_{p}$. In (42) and (43) (as well as the unresolved-scale equation (33)), the resolved parts of velocity and pressure may be further separated into a large- and a small-scale part, as given in (38) and (39).

4 Residual-Based and Stabilized Methods

Stabilized FEMs have been developed for and applied to various problems of computational mechanics, among others, Computational Fluid Dynamics (CFD). In fact, flow problems have always been and remain one of the main applications of residual-based and stabilized methods. In the following, residual-based stabilization methods leading to the RBVMM for LES of turbulent flow will be reviewed in detail. Similar stabilized methods may be derived via Finite Increment Calculus (FIC), as originally demonstrated in [161]. Applications of FIC-based methods to turbulent flows were reported, e.g., in [162]. Other approaches to stabilization are provided by so-called Face- (or edge-) Oriented Stabilization (FOS) methods, originally proposed in [29] for convection–diffusion problems, and Local-Projection Stabilization (LPS) methods, which were originally introduced for the Stokes equations in [12]. Later, FOS and LPS methods were further developed for the Oseen problem in [28] and [20], respectively. A review of residual-based stabilization methods comparing them to FOS and LPS methods can be found in [21].

4.1 Overview

The foundations of residual-based stabilization methods were laid towards the end of the 1970s, that is, almost four decades ago. The Streamline/Upwind Petrov-Galerkin (SUPG) method was developed at that time and later published in detail in [26]. This approach was alternatively termed streamline diffusion method in [123]. The respective SUPG term is added to prevent numerical instabilities due to dominant convection by introducing dissipation in streamline direction. The Pressure Stabilizing Petrov–Galerkin (PSPG) method was originally proposed in [108] (and later named this way in [208]). The presence of a PSPG term allows for circumventing the inf-sup condition (see, e.g., [24]), a mixed finite element formulation is subject to, and enables the convenient choice of equal-order interpolated elements for velocity and pressure. The inclusion of a bulk-viscosity term was suggested for the first time in [62]. This term, which is also referred to as grad-div term (see, e.g., [21]) or least-squares incompressibility constraint (see, e.g., [209]), was more closely investigated in [54]. Among other things, it provides improved discrete mass conservation, which comes along with an additional numerical dissipation; see, e.g., [165]. The benefits and drawbacks related to this term are still discussed in the literature, both from a mathematical and an engineering point of view; see, e.g., [165] and [147] for recent contributions to this discussion.

After initial considerations with a view on the suitability of residual-based stabilization methods for LES had already been outlined in [47], the RBVMM was eventually proposed in [9], founding on the original idea of the VMM and thus on the concept of ILES. This method takes the non-linearity of the Navier–Stokes equations particularly into account and may thus be considered an advanced stabilized method. After all, two further stabilizing terms, a cross- and a subgrid-scale Reynolds-stress term, were introduced by this approach. Extending the aforementioned quasi-static residual-based stabilization methods, time-dependent residual-based subgrid-scale approximations were originally introduced in [49] and later investigated for

LES for the first time in [68]. In [96, 147], bubble functions were defined on the element interior for devising a more sophisticated stabilization operator for RBVMMs (see also, e.g., [25] for details on residual-free bubble functions). A specific edge-based implementation of residual-based stabilization methods was proposed in [142]. Furthermore, it is remarked that the application of residual-based subgrid-scale approximations, apart from stabilized methods, was recently proposed for a (two-scale) subgrid-viscosity approach in [163]. In that study, the subgrid viscosity was determined using a residual-based approximation for the subgrid-scale velocity.

4.2 Evolution of Subgrid Scales

Starting point of the derivation of RBVMMs is the two-scale decomposition introduced in Sect. 3.3. Equation (33), governing the evolution of the unresolved scales, enables an estimation of the subgrid-scale quantities based on mathematical considerations without any explicit physically-motivated modeling. Various strategies to recover the subgrid-scale quantities from Eq. (33), ranging from the elementwise numerical solution of local subproblems to approximate analytical expressions for $\hat{\mathbf{u}}$ and $\hat{p}_{\text{kin}}$, have been proposed in the literature; see, e.g., [107] for an overview and the relationship between them.

Rearranging Eq. (33) and splitting again into momentum and continuity equation yields

$$\begin{aligned}&\left(\hat{\mathbf{v}}, \frac{\partial \hat{\mathbf{u}}}{\partial t}\right)_{\Omega} + \left(\hat{\mathbf{v}}, \mathbf{u}^h \cdot \nabla \hat{\mathbf{u}} + \hat{\mathbf{u}} \cdot \nabla \mathbf{u}^h + \hat{\mathbf{u}} \cdot \nabla \hat{\mathbf{u}}\right)_{\Omega} \\ &+ (\boldsymbol{\varepsilon}(\hat{\mathbf{v}}), 2\nu\boldsymbol{\varepsilon}(\hat{\mathbf{u}}))_{\Omega} - \left(\nabla \cdot \hat{\mathbf{v}}, \hat{p}_{\text{kin}}\right)_{\Omega} = \\ &- \mathcal{B}_{\text{M}}(\hat{\mathbf{v}}; \mathbf{u}^h, p^h_{\text{kin}}) + \ell_{\text{NS}}(\hat{\mathbf{v}}),\end{aligned} \tag{44}$$

$$(\hat{q}, \nabla \cdot \hat{\mathbf{u}})_{\Omega} = -\mathcal{B}_{\text{C}}(\hat{q}, \mathbf{u}^h). \tag{45}$$

where the projections of the resolved-scale residuals onto the space of unresolved scales constitute the right-hand sides and drive the unresolved-scale equations.

While the subgrid-scale velocity $\hat{\mathbf{u}}$ is directly obtained from momentum equation (44), the subgrid-scale pressure $\hat{p}_{\text{kin}}$ is governed by a Poisson equation resulting from taking the divergence of the momentum equation and using the continuity equation. Assuming the influence of $\hat{p}_{\text{kin}}$ on the evolution of $\hat{\mathbf{u}}$ negligible as well as the residual of the momentum equation divergence-free and simplifying other terms, the following projected equations are obtained for $\hat{\mathbf{u}}$ and $\hat{p}_{\text{kin}}$:

$$\frac{\partial \hat{\mathbf{u}}}{\partial t} + \left(\mathbf{u}^h + \hat{\mathbf{u}}\right) \cdot \nabla \hat{\mathbf{u}} - \nu \Delta \hat{\mathbf{u}} = -\mathbf{r}_{\text{M}}^{h,\hat{}}, \tag{46}$$

$$-\Delta \hat{p}_{\text{kin}} = -\frac{\partial r_{\text{C}}^h}{\partial t} - (\mathbf{u}^h + \hat{\mathbf{u}}) \cdot \nabla r_{\text{C}}^h + \nu \Delta r_{\text{C}}^h, \tag{47}$$

where

$$\begin{aligned}\mathbf{r}_{\text{M}}^{h,\hat{}} &= \frac{\partial \mathbf{u}^h}{\partial t} + (\mathbf{u}^h + \hat{\mathbf{u}}) \cdot \nabla \mathbf{u}^h + \nabla p^h_{\text{kin}} \\ &- 2\nu \nabla \cdot \boldsymbol{\varepsilon}(\mathbf{u}^h) - \mathbf{f},\end{aligned} \tag{48}$$

$$r_{\text{C}}^h = \nabla \cdot \mathbf{u}^h \tag{49}$$

denote the residual of momentum and continuity equation, respectively. Here, $\mathbf{r}_{\text{M}}^{h,\hat{}}$ additionally includes the convective term $\hat{\mathbf{u}} \cdot \nabla \mathbf{u}^h$, which depends on the subgrid-scale velocity, in contrast to the discrete residual $\mathbf{r}_{\text{M}}^h$ of the momentum equation, which will also be used below. Instead of a direct inclusion of the residuals, as done in Eqs. (46) and (47), L_2-projections of the residuals orthogonal to the finite element space were suggested in [47], leading to so-called orthogonal subgrid scales.

For every term in Eqs. (46) and (47), a corresponding algebraic scaling can be deduced. The scaling of the transient term of the unresolved scale momentum equation is given by

$$\frac{\partial \hat{\mathbf{u}}}{\partial t}: \quad \sim \frac{1}{\Delta t} \hat{\mathbf{u}}. \tag{50}$$

The convective term scales as

$$\left(\mathbf{u}^h + \hat{\mathbf{u}}\right) \cdot \nabla \hat{\mathbf{u}}: \quad \sim \frac{\|\mathbf{u}^h + \hat{\mathbf{u}}\|}{h} \hat{\mathbf{u}} \tag{51}$$

and the viscous term as

$$\nu \Delta \hat{\mathbf{u}}: \quad \sim \frac{\nu}{h^2} \hat{\mathbf{u}}. \tag{52}$$

The scalings of the respective terms of the pressure Poisson equation read analogously, with $\hat{\mathbf{u}}$ being replaced by r_{C}^h. For the Laplacian of the subgrid-scale pressure, it is given by

$$\Delta \hat{p}_{\text{kin}}: \quad \sim \frac{1}{h^2} \hat{p}_{\text{kin}}. \tag{53}$$

4.3 Subgrid-Scale Approximation

Residual-based subgrid-scale modeling aims at providing an approximate analytical solution for $\hat{\mathbf{u}}$ and $\hat{p}_{\text{kin}}$; see, e.g., [9, 47]. For this purpose, the scalings introduced above are used to approximate the partial differential equations (46) and (47) for the unresolved-scale quantities by ordinary differential equations or algebraic relations. As a result of the respective procedure, algebraic scalings are combined to one scaling parameter for each equation, which can be identified as the inverse stabilization parameter of classical stabilized FEMs, reviewed in Sect. 4.1. That is,

$$\frac{\partial}{\partial t}(\cdot) + \left(\left(\mathbf{u}^h + \hat{\mathbf{u}}\right) \cdot \nabla\right)(\cdot) - \nu \Delta(\cdot) \sim \tau_{\text{M}}^{-1}, \tag{54}$$

$$\left(\left(\mathbf{u}^h + \hat{\mathbf{u}}\right) \cdot \nabla\right)(\cdot) - \nu\Delta(\cdot) \sim \tau_{\mathrm{M}/\Delta t}^{-1}, \tag{55}$$

depending on whether the time derivative is included or not. Furthermore, the parameter τ_{C} is introduced, which scales as

$$\tau_{\mathrm{C}}^{-1} \sim \frac{\tau_{\mathrm{M}}}{h^2}. \tag{56}$$

The parameter $\tau_{\mathrm{C}/\Delta t}$ is defined analogously based on $\tau_{\mathrm{M}/\Delta t}$.

Using the approximations excluding the time derivative, the following ordinary differential equations for the subgrid-scale velocity and pressure are obtained:

$$\frac{\partial \hat{\mathbf{u}}}{\partial t} + \tau_{\mathrm{M}/\Delta t}^{-1}\hat{\mathbf{u}} = -\mathbf{r}_{\mathrm{M}}^{h,\hat{}}, \tag{57}$$

$$\tau_{\mathrm{C}/\Delta t}^{-1}\hat{p}_{\mathrm{kin}} = -r_{\mathrm{C}}^h - \tau_{\mathrm{M}/\Delta t}\frac{\partial r_{\mathrm{C}}^h}{\partial t}. \tag{58}$$

In [49], the subgrid scales were considered this way for the first time, and it was referred to this strategy as time-dependent residual-based subgrid-scale modeling.

Quasi-static subgrid-scales are obtained when considering the time derivatives as a part of the differential operator as in equation (54) (or when omitting them completely and using $\tau_{\mathrm{M}/\Delta t}$ and $\tau_{\mathrm{C}/\Delta t}$). As a result, algebraic relations for $\hat{\mathbf{u}}$ and $\hat{p}_{\mathrm{kin}}$ are obtained as

$$\hat{\mathbf{u}} = -\tau_{\mathrm{M}}\mathbf{r}_{\mathrm{M}}^h, \tag{59}$$

$$\hat{p}_{\mathrm{kin}} = -\tau_{\mathrm{C}}r_{\mathrm{C}}^h. \tag{60}$$

The convective terms $\hat{\mathbf{u}} \cdot \nabla\hat{\mathbf{u}}$ and $\hat{\mathbf{u}} \cdot \nabla\mathbf{u}^h$ of equation (46) are typically neglected; that is, $\hat{\mathbf{u}}$ is not considered in the velocity magnitude of scaling (51) and the residual of the momentum equation (48). The consideration of these terms in the context of quasi-static subgrid scales was discussed, e.g., in [38].

Various definitions for the stabilization parameters τ_{M} and τ_{C} can be found in the literature, e.g., the following ones proposed in [206, 220]:

$$\tau_{\mathrm{M}} = \frac{1}{\sqrt{\frac{4}{\Delta t^2} + \mathbf{u}^h \cdot \mathbf{G}\mathbf{u}^h + C_{\mathrm{I}}\nu^2\mathbf{G}:\mathbf{G}}}, \tag{61}$$

$$\tau_{\mathrm{C}} = \frac{1}{\tau_{\mathrm{M}}\mathrm{tr}(\mathbf{G})}, \tag{62}$$

where

$$G_{ij} = \sum_{k=1}^{3}\frac{\partial\xi_k}{\partial x_i}\frac{\partial\xi_k}{\partial x_j} \tag{63}$$

is the covariant metric tensor related to the mapping between global coordinates $\mathbf{x}$ and local element coordinates $\boldsymbol{\xi}$. The time-step length of the temporal discretization is denoted by Δt, and C_{I} is a positive constant independent of the characteristic element length. The alternative definitions of the stabilization parameters, $\tau_{\mathrm{M}/\Delta t}$ and $\tau_{\mathrm{C}/\Delta t}$, respectively, are obtained by omitting the term depending on Δt in τ_{M}.

It is remarked that, for quasi-static subgrid scales, Δt and h cannot be chosen independent of each other if the dependency on the time-step length is omitted in the definition of the stabilization parameters, i.e., if $\tau_{\mathrm{M}/\Delta t}$ and $\tau_{\mathrm{C}/\Delta t}$ are applied. However, if Δt is included, $\tau_{\mathrm{M}} \to 0$ and $\tau_{\mathrm{C}} \to \infty$ for $\Delta t \to 0$. For small time-step lengths, chosen independent of the resolution, time-dependent subgrid-scales demonstrated good performance in various numerical studies; see, e.g., [49, 68]. Aside from this brief remark, we would merely like to refer the reader to the literature on the topic of small time-step lengths in the context of semi-discrete stabilized finite element methods, such as [16, 99].

4.4 Final Residual-Based Variational Multiscale Formulation

In the following, merely the algebraic relations (59) and (60) are considered exemplarily. An elaborate presentation of the closed variational multiscale formulation with time-dependent subgrid-scales may be found, e.g., in [49]. Introducing the subgrid-scale approximations (59) and (60) into the unclosed terms (35) to (37) of the variational multiscale formulation (34), integrating by parts some terms and omitting some other terms, the following residual-based stabilization (or multiscale) terms are obtained:

$$\begin{aligned}&\mathcal{C}(\mathbf{v}^h;\mathbf{u}^h,\hat{\mathbf{u}}) \approx \\ &\left(\mathbf{u}^h \cdot \nabla\mathbf{v}^h, \tau_{\mathrm{M}}\mathbf{r}_{\mathrm{M}}^h\right)_{\Omega^*} - \left(\mathbf{v}^h, \tau_{\mathrm{M}}\mathbf{r}_{\mathrm{M}}^h \cdot \nabla\mathbf{u}^h\right)_{\Omega^*},\end{aligned} \tag{64}$$

$$\mathcal{R}(\mathbf{v}^h;\hat{\mathbf{u}}) \approx -\left(\tau_{\mathrm{M}}\mathbf{r}_{\mathrm{M}}^h \cdot \nabla\mathbf{v}^h, \tau_{\mathrm{M}}\mathbf{r}_{\mathrm{M}}^h\right)_{\Omega^*}, \tag{65}$$

$$\begin{aligned}&\mathcal{B}_{\mathrm{NS}}^{1,\mathrm{lin}}(\mathbf{v}^h, q^h;\hat{\mathbf{u}},\hat{p}_{\mathrm{kin}}) \approx \\ &\left(\nabla \cdot \mathbf{v}^h, \tau_{\mathrm{C}}r_{\mathrm{C}}^h\right)_{\Omega^*} + \left(\nabla q^h, \tau_{\mathrm{M}}\mathbf{r}_{\mathrm{M}}^h\right)_{\Omega^*}.\end{aligned} \tag{66}$$

It is assumed that the domain Ω is partitioned into n_{el} non-overlapping elements e with domain Ω^e and characteristic element length h. The resulting triangulation is denoted by $\mathcal{T}^h$. Moreover, Ω^* represents the union of all element interiors, i.e., $\Omega^* := \bigcup_{e=1}^{n_{\mathrm{el}}}\Omega^e$, and $(\cdot,\cdot)_{\Omega^*} := \sum_{e\in\mathcal{T}^h}(\cdot,\cdot)_{\Omega^e}$. To eliminate potential boundary terms arising from integration by parts, it is assumed that the subgrid-scale quantities vanish on the element boundaries; see, e.g., [106] for elaboration.

The first cross-stress term constitutes the SUPG term. Moreover, the grad-div term, the first term of the modeled form of $\mathcal{B}_{\mathrm{NS}}^{1,\mathrm{lin}}(\mathbf{v}^h, q^h;\hat{\mathbf{u}},\hat{p}_{\mathrm{kin}})$, and the PSPG term, the second term, arise. For the present quasi-static subgrid scales, the transient term of $\mathcal{B}_{\mathrm{NS}}^{1,\mathrm{lin}}(\mathbf{v}^h, q^h;\hat{\mathbf{u}},\hat{p}_{\mathrm{kin}})$ is neglected. The

viscous term of $\mathcal{B}_{\mathrm{NS}}^{1,\mathrm{lin}}(\mathbf{v}^h, q^h; \hat{\mathbf{u}}, \hat{p}_{\mathrm{kin}})$ is likewise omitted in the present form, following, e.g., [9]. Note that, for orthogonal subgrid scales, independent of whether they are considered quasi-static or time-dependent, both terms vanish anyway. Deriving the aforementioned stabilization terms in the context of the VMM gives rise to two further terms: the second cross-stress term as well as the subgrid-scale Reynolds-stress term. As analyzed in [112], the second cross-stress term enables global momentum conservation for the convective form of the momentum equation. The subgrid-scale Reynolds-stress term may be interpreted as a convective stabilization of the second cross-stress term, acting analogously to the SUPG term for the standard Galerkin convective term. Since all residual-based stabilization terms vanish for the exact solution, consistency is ensured for the overall approach.

The formulation incorporating terms (64) to (66) eventually constitutes a complete RBVMM: find $(\mathbf{u}^h, p_{\mathrm{kin}}^h) \in \mathcal{S}_{\mathbf{u}}^h \times \mathcal{S}_p^h$ such that

$$\begin{aligned} &\mathcal{B}_{\mathrm{NS}}(\mathbf{v}^h, q^h; \mathbf{u}^h, p_{\mathrm{kin}}^h) + \left(\mathbf{u}^h \cdot \nabla \mathbf{v}^h, \tau_{\mathrm{M}} \mathbf{r}_{\mathrm{M}}^h\right)_{\Omega^*} \\ &- \left(\mathbf{v}^h, \tau_{\mathrm{M}} \mathbf{r}_{\mathrm{M}}^h \cdot \nabla \mathbf{u}^h\right)_{\Omega^*} - \left(\tau_{\mathrm{M}} \mathbf{r}_{\mathrm{M}}^h \cdot \nabla \mathbf{v}^h, \tau_{\mathrm{M}} \mathbf{r}_{\mathrm{M}}^h\right)_{\Omega^*} \\ &+ \left(\nabla q^h, \tau_{\mathrm{M}} \mathbf{r}_{\mathrm{M}}^h\right)_{\Omega^*} + \left(\nabla \cdot \mathbf{v}^h, \tau_{\mathrm{C}} r_{\mathrm{C}}^h\right)_{\Omega^*} = \ell_{\mathrm{NS}}(\mathbf{v}^h) \end{aligned} \tag{67}$$

for all $(\mathbf{v}^h, q^h) \in \mathcal{V}_{\mathbf{u}}^h \times \mathcal{V}_p^h$.

5 Small-Scale Subgrid Viscosity

Subgrid-scale modeling in form of a small-scale subgrid-viscosity term within a VMM for LES was originally proposed in [110]. It was later pointed out, e.g., in [51] that a three-scale separation as given by (38) to (41) represents the basis for this approach, which was reviewed in [1, 80, 118]. The basic idea of adding an artificial diffusion term for stability reasons on the second level of a two-scale decomposition goes back to [94], though, with an interesting, more general variant of this idea later proposed in [136]. Two solution strategies were distinguished in [80]: either explicitly solving both constituents of the two-equation system [i.e., the large-scale equation (42) and the small-scale equation (43)] or solving a formally reunified resolved-scale equation, for which the separation of scales remains identifyable merely due to the subgrid-viscosity term still acting directly only on the smaller resolved scales. These two strategies will be described in the following two subsections. Finally, small-scale subgrid-viscosity models which are usually applied are discussed.

5.1 Explicit Solution of Large- and Small-Scale Equation

Methods for an explicit solution strategy appear to have only been developed in the context of FEMs: one in [91] using residual-free bubble functions on the small-scale level as earlier proposed, e.g., in [63, 90] and one in [144] using spectral elements on the small-scale level. The former approach will be briefly outlined in the following.

Large- and small-scale equation (42) and (43) are modeled as follows: find $(\overline{\mathbf{u}}^h, \overline{p}_{\mathrm{kin}}^h) \in \overline{\mathcal{S}}_{\mathbf{u}}^h \times \overline{\mathcal{S}}_p^h$ such that

$$\mathcal{B}_{\mathrm{NS}}(\overline{\mathbf{v}}^h, \overline{q}^h; \overline{\mathbf{u}}^h + \mathbf{u}'^h, \overline{p}_{\mathrm{kin}}^h + p_{\mathrm{kin}}'^h) = \ell_{\mathrm{NS}}(\overline{\mathbf{v}}^h) \tag{68}$$

for all $(\overline{\mathbf{v}}^h, \overline{q}^h) \in \overline{\mathcal{V}}_{\mathbf{u}}^h \times \overline{\mathcal{V}}_p^h$, and find $(\mathbf{u}'^h, p_{\mathrm{kin}}'^h) \in \mathcal{S}_{\mathbf{u}}'^h \times \mathcal{S}_p'^h$ such that

$$\begin{aligned} &\mathcal{B}_{\mathrm{NS}}(\mathbf{v}'^h, q'^h; \overline{\mathbf{u}}^h + \mathbf{u}'^h, \overline{p}_{\mathrm{kin}}^h + p_{\mathrm{kin}}'^h) \\ &+ \left(\boldsymbol{\varepsilon}(\mathbf{v}'^h), 2\nu_{\mathrm{sgs}}' \boldsymbol{\varepsilon}(\mathbf{u}'^h)\right)_{\Omega} = \ell_{\mathrm{NS}}(\mathbf{v}'^h) \end{aligned} \tag{69}$$

for all $(\mathbf{v}'^h, q'^h) \in \mathcal{V}_{\mathbf{u}}'^h \times \mathcal{V}_p'^h$, where ν_{sgs}' denotes the small-scale subgrid viscosity. Note that both large- and small-scale equation are modeled equations. While the modeling of the small-scale equation via the subgrid-viscosity term is obvious, the modeling assumption for the large-scale equation reads

$$\mathcal{B}_{\mathrm{NS}}^1(\overline{\mathbf{v}}^h, \overline{q}^h; \mathbf{u}^h, \hat{\mathbf{u}}, \hat{p}_{\mathrm{kin}}) + \mathcal{B}_{\mathrm{NS}}^2(\overline{\mathbf{v}}^h; \hat{\mathbf{u}}) \approx 0, \tag{70}$$

based on the assumption of a clear separation of the large-scale space and the space of unresolved scales. Equations (68) and (69) are a pair of coupled non-linear variational equations. As a result of an iterative solution procedure, the large- and the small-scale part of the solution are obtained, their sum representing the complete solution.

For the particular method presented here, residual-free bubbles are used for a localized solution of the small-scale equation. The reasonability of a localization strategy for the smaller resolved scales is supported by perceptions from turbulence theory, that is, the tendency of decorrelation in a turbulent flow with increasing spatial separation of two points in the flow domain. This tendency was revealed by analyzing two-point correlations in turbulent flows (see, e.g., [173]). The smaller the scales are, the shorter is the distance over which a rather strong correlation of the scales has to be expected. Therefore, a locally confined resolution of the smaller scales appears to be a reasonable strategy.

By using residual-free bubbles (see, e.g., [25]), it is aimed at satisfying the respective governing partial differential equation by the complete solution in strong form on each individual element domain Ω^e of the basic discretization. For this purpose, zero Dirichlet boundary conditions are assumed for the small-scale part of the solution on the boundaries of Ω^e. For the underlying case of a separation of the resolved solution into a large- and a small-scale part, it is solved for the small-scale bubble part of the solution, while the residual of the large-scale part of the solution appears on the right-hand side of the residual-free bubble

equation, representing the driving force of this equation. Residual-free bubbles for the stabilization of a linearized stationary Navier–Stokes problem were first proposed in [187]. According to [187], the bubble space exclusively enhances the velocity approximation, that is, it is assumed that $p'^h_{\mathrm{kin}} = 0$. Among other things, it is aimed at the fulfillment of the inf-sup condition by this assumption.

Consequently, the strong form of the small-scale momentum equation is given by

$$\frac{\partial \mathbf{u}'^h}{\partial t} + \mathbf{u}^h \cdot \nabla \mathbf{u}'^h - \nabla \cdot \left(2\left(\nu + \nu'_{\mathrm{sgs}} \right) \boldsymbol{\varepsilon}(\mathbf{u}'^h) \right) = -\bar{\mathbf{r}}^h_{\mathrm{M}}, \quad (71)$$

where $\bar{\mathbf{r}}^h_{\mathrm{M}}$ denotes the aforementioned residual of the large-scale part of the solution. Equation (71) is similar to equation (46) for the unresolved scales in the context of residual-based stabilization methods. When numerically solving equation (71) in the present context, further residual-based stabilization terms, as described in Sect. 4, may be added for additional stabilization besides the subgrid-viscosity term. Having solved equation (71) for $\mathbf{u}'^h$, this small-scale solution may then be inserted into the variational large-scale equation (68), to obtain the large-scale part of the solution.

Despite the aforementioned assumption $p'^h_{\mathrm{kin}} = 0$, enabling formulation (71), it turned out to be advantageous to include a small-scale pressure which is completely independent of the small-scale momentum equation (71) in the large-scale equation (68). However, it is not advisable to solve, for instance, a Poisson equation for the pressure aside from momentum equation (71) on the small-scale level; it is rather intended to incorporate the effect of the small-scale pressure into the final large-scale equation via an additional term in the form of a residual-based stabilization term. Thus, p'^h_{kin} is approximated analogously to (60) as

$$p'^h_{\mathrm{kin}} = -\tau_{\mathrm{C}} \bar{r}^h_{\mathrm{C}}. \quad (72)$$

In general, the fulfillment of the continuity condition is well known to become more important with increasing Reynolds number (see, e.g., [93, 209]). Therefore, approximation (72) is a crucial ingredient of the overall solution strategy, particularly for the simulation of flows at high Reynolds numbers.

In summary, residual-free bubbles are used to solve the small-scale momentum equation. Additionally, the effect of the small-scale pressure is taken into account via a residual-based stabilization term in the final large-scale equation. Thus, it amounts to a combined residual-free bubble/stabilizing strategy. After all, the main assumption $p'^h_{\mathrm{kin}} = 0$ in the small-scale momentum equation results in the fact that, analogously to residual-based stabilization methods as addressed in Sect. 4, the small-scale velocity is exclusively driven by the residual of the large-scale momentum equation and not by the residual of the continuity equation; see, e.g., [47]. Further discussion of this assumption may also be found in [90].

To obtain the discrete solution of the small-scale momentum equation, a submesh is introduced on each individual element domain Ω^e of the basic discretization. The characteristic element length of the latter is denoted by $\bar{h}$. The submesh on a second level or, more precisely, the number of n_{el} discretizations on a second level, where n_{el} denotes the number of elements of the basic discretization, is the support for the small-scale part of the solution (i.e., the small-scale momentum equation (71) subject to the residual-free bubble assumption). Its characteristic element length is denoted by h'. Details of a particular approach which aims at solving directly for shape-function components of the small-scale velocity as well as further assumptions which enable such a separation into shape function components are described in [90]. The resulting shape-function components of the small-scale velocity are eventually substituted into the large-scale equation in the course of a static condensation procedure.

5.2 Solution of a Monolithic Equation System

Reunifying the modeled large- and small-scale equation (68) and (69) results in: find $(\mathbf{u}^h, p^h_{\mathrm{kin}}) \in \mathcal{S}^h_{\mathbf{u}} \times \mathcal{S}^h_p$ such that

$$\mathcal{B}_{\mathrm{NS}}(\mathbf{v}^h, q^h; \mathbf{u}^h, p^h_{\mathrm{kin}}) - \left(\mathbf{v}'^h, \nabla \cdot \left(2\nu'_{\mathrm{sgs}} \boldsymbol{\varepsilon}(\mathbf{u}'^h) \right) \right)_{\Omega} = \ell_{\mathrm{NS}}(\mathbf{v}^h) \quad (73)$$

for all $(\mathbf{v}^h, q^h) \in \mathcal{V}^h_{\mathbf{u}} \times \mathcal{V}^h_p$. Note that the small-scale subgrid-viscosity term in Eq. (73) is given in weighted residual form and not yet integrated by parts, allowing for different subsequent integration by parts for, e.g., an FEM or FVM. The majority of methods which include a small-scale subgrid viscosity follow this second strategy of solving Eq. (73), and they have been developed based on a variety of numerical methods. Examples are (continuous Galerkin) FEMs as addressed, for instance, in [40, 83, 114, 119, 135], discontinuous Galerkin methods as, e.g., in [50], combined finite element/volume methods as in [129], FVMs as in [79], combined finite volume/spectral methods as in [175], spectral methods as in [111, 216], and spectral element methods as in [158, 219].

Most of the method developments were done for the incompressible Navier–Stokes equations; exceptions are [50, 129, 158], wherein the compressible Navier-Stokes equations were addressed, though the respective numerical examples often considered flow at lower Mach numbers. A theoretical investigation of the three-scale variational multiscale approach to the compressible Navier–Stokes equations (i.e., without supporting numerical examples) was provided in [19]. A method with small-scale subgrid viscosity for variable-density turbulent flow at low Mach

number, which will be focused on in Sect. 9, was proposed in [87].

Besides the numerical method, another important issue is how the resolved scales are separated into larger and smaller ones. Different approaches to scale separation for the reunified resolved-scale equation (73) were proposed. In [80], two different scale-separating approaches were distinguished: a p-type scale separation and an h-type scale separation. The former refers to scale separation based on the polynomial order of the shape functions (e.g., in FEMs) and the latter to scale separation based on a coarser grid. Some of them will be briefly presented in the following two subsections. Before, however, it is noted that analogous filter-based methods were also proposed, which aim at subgrid-scale modeling via a small-scale subgrid-viscosity term, while using a more traditional filtering approach instead of variational projection. This idea was outlined in [214] and used therein based on FDMs. Further examples can be found in the context of FDMs in [116, 127]. This strategy was also considered, for instance, based on FVMs (see, e.g., [189]) and spectral methods (see, e.g., [205]).

5.2.1 *p-Type Scale Separation*

In this section, two approaches to p-type scale separation for continuous Galerkin FEMs are presented, and the reader is referred to, e.g., [50] for similar ideas in the context of discontinuous Galerkin FEMs.

In [114], hierarchical shape functions within a (continuous) FEM, an alternative concept compared to (standard) Lagrangian shape functions, were exploited for scale separation in the context of VMMs for LES. More details on hierarchical shape functions can be found in textbooks on the FEM such as [223]. The essential feature in this context is a natural scale separation within the set of shape functions of order k. All polynomials up to a certain order $\overline{k}$ are chosen for the polynomial representation of the space of larger resolved scales. These large-scale polynomials and further polynomials up to a necessarily higher order k are then chosen for the representation of the complete range of resolved scales. The polynomial(s) of order k' defined by

$$\overline{k} < k' \leq k, \tag{74}$$

where $[\overline{k}, k', k] \in \mathbb{N}$, are then assigned to the smaller resolved scales. Note that both large- and small-scale parts of the solution are subject to the same discretization with characteristic element length h, merely distinguished by the shape functions of the respective polynomial order.

L_2-projections based on velocity-deformation tensors were proposed as a p-type scale separation in [119], among others, based on ideas published earlier in [136]. In that approach, in contrast to (73), where the subgrid-viscosity term is directly applied to the smaller resolved scales, the subgrid-viscosity term is first applied to all scales and then subtracted from the larger resolved scales, resulting in the following system of equations: find $(\mathbf{u}^h, p^h_{\text{kin}}) \in \mathcal{S}^h_{\mathbf{u}} \times \mathcal{S}^h_p$ and $\overline{\boldsymbol{\gamma}}^h \in \overline{\mathcal{S}}^h_{\boldsymbol{\gamma}}$ such that

$$\begin{aligned} &\mathcal{B}_{\text{NS}}(\mathbf{v}^h, q^h; \mathbf{u}^h, p^h_{\text{kin}}) + \left(\boldsymbol{\varepsilon}(\mathbf{v}^h), 2\nu'_{\text{sgs}}\boldsymbol{\varepsilon}(\mathbf{u}^h)\right)_\Omega \\ &- \left(\boldsymbol{\varepsilon}(\mathbf{v}^h), 2\nu'_{\text{sgs}}\overline{\boldsymbol{\gamma}}^h\right)_\Omega = \ell_{\text{NS}}(\mathbf{v}^h) \end{aligned} \tag{75}$$

$$\left(\overline{\boldsymbol{\lambda}}^h, \overline{\boldsymbol{\gamma}}^h - \boldsymbol{\varepsilon}(\mathbf{u}^h)\right)_\Omega = 0 \tag{76}$$

for all $(\mathbf{v}^h, q^h) \in \mathcal{V}^h_{\mathbf{u}} \times \mathcal{V}^h_p$ and $\overline{\boldsymbol{\lambda}}^h \in \overline{\mathcal{V}}^h_{\boldsymbol{\gamma}}$, where appropriate solution and weighting function spaces $\overline{\mathcal{S}}^h_{\boldsymbol{\gamma}}$ and $\overline{\mathcal{V}}^h_{\boldsymbol{\gamma}}$ for $\overline{\boldsymbol{\gamma}}^h$ and the corresponding weighting function $\overline{\boldsymbol{\lambda}}^h$ are assumed. Furthermore, it is assumed: if the L_2-projection onto the large-scale space $\mathcal{P}_{\overline{\mathcal{V}}^h_{\boldsymbol{\gamma}}}: \mathcal{V}_{\boldsymbol{\gamma}} \rightarrow \overline{\mathcal{V}}^h_{\boldsymbol{\gamma}}$ is defined for $\boldsymbol{\varepsilon}(\mathbf{v}) \rightarrow \mathcal{P}_{\overline{\mathcal{V}}^h_{\boldsymbol{\gamma}}}[\boldsymbol{\varepsilon}(\mathbf{v})]$ with

$$\left(\overline{\boldsymbol{\lambda}}^h, \mathcal{P}_{\overline{\mathcal{V}}^h_{\boldsymbol{\gamma}}}[\boldsymbol{\varepsilon}(\mathbf{v})] - \boldsymbol{\varepsilon}(\mathbf{v})\right)_\Omega = 0 \quad \forall\, \overline{\boldsymbol{\lambda}}^h \in \overline{\mathcal{V}}^h_{\boldsymbol{\gamma}}, \tag{77}$$

then it holds that

$$\overline{\boldsymbol{\gamma}}^h = \mathcal{P}_{\overline{\mathcal{V}}^h_{\boldsymbol{\gamma}}}\left[\boldsymbol{\varepsilon}(\mathbf{u}^h)\right], \tag{78}$$

that is, $\overline{\boldsymbol{\gamma}}^h$ is indeed the large-scale part of the rate-of-deformation tensor $\boldsymbol{\varepsilon}(\mathbf{u}^h)$.

Inserting (78) into (75) yields: find $(\mathbf{u}^h, p^h_{\text{kin}}) \in \mathcal{S}^h_{\mathbf{u}} \times \mathcal{S}^h_p$ such that

$$\begin{aligned} &\mathcal{B}_{\text{NS}}(\mathbf{v}^h, q^h; \mathbf{u}^h, p^h_{\text{kin}}) + \Bigg(\boldsymbol{\varepsilon}(\mathbf{v}^h) - \mathcal{P}_{\overline{\mathcal{V}}^h_{\boldsymbol{\gamma}}}\left[\boldsymbol{\varepsilon}(\mathbf{v}^h)\right], \\ &2\nu'_{\text{sgs}}\left(\boldsymbol{\varepsilon}(\mathbf{u}^h) - \mathcal{P}_{\overline{\mathcal{V}}^h_{\boldsymbol{\gamma}}}\left[\boldsymbol{\varepsilon}(\mathbf{u}^h)\right]\right)\Bigg)_\Omega = \ell_{\text{NS}}(\mathbf{v}^h) \end{aligned} \tag{79}$$

for all $(\mathbf{v}^h, q^h) \in \mathcal{V}^h_{\mathbf{u}} \times \mathcal{V}^h_p$. The definition of the large scales by an L_2-projection commutes with differentiation, as proven in [119], that is,

$$\mathcal{P}_{\overline{\mathcal{V}}^h_{\boldsymbol{\gamma}}}[\boldsymbol{\varepsilon}(\mathbf{v})] = \boldsymbol{\varepsilon}(\mathcal{P}_{\overline{\mathcal{V}}^h_{\boldsymbol{\gamma}}}[\mathbf{v}]). \tag{80}$$

Note that such a commutation as defined by (80) cannot be proven for traditional filtering approaches in general. As a result of (80), Eq. (79) may be simplified to

$$\begin{aligned} &\mathcal{B}_{\text{NS}}(\mathbf{v}^h, q^h; \mathbf{u}^h, p^h_{\text{kin}}) \\ &+ \left(\boldsymbol{\varepsilon}(\mathbf{v}^h - \overline{\mathbf{v}}^h), 2\nu'_{\text{sgs}}\boldsymbol{\varepsilon}(\mathbf{u}^h - \overline{\mathbf{u}}^h)\right)_\Omega \\ &= \mathcal{B}_{\text{NS}}(\mathbf{v}^h, q^h; \mathbf{u}^h, p^h_{\text{kin}}) \\ &+ \left(\boldsymbol{\varepsilon}(\mathbf{v}'^h), 2\nu'_{\text{sgs}}\boldsymbol{\varepsilon}(\mathbf{u}'^h)\right)_\Omega = \ell_{\text{NS}}(\mathbf{v}^h), \end{aligned} \tag{81}$$

where it is taken advantage of the following definitions: $\overline{\mathbf{v}}^h = \mathcal{P}_{\overline{\mathcal{V}}^h_{\boldsymbol{\gamma}}}\left[\mathbf{v}^h\right]$ and $\overline{\mathbf{u}}^h = \mathcal{P}_{\overline{\mathcal{V}}^h_{\boldsymbol{\gamma}}}\left[\mathbf{u}^h\right]$. It is easily observable that

(the second part of) Eq. (81) is equal to Eq. (73) when being integrated by parts.

The space $\overline{\mathcal{V}}_\gamma^h$ represents the large scales in this approach. There are two options for defining $\overline{\mathcal{V}}_\gamma^h$: either it may be defined on a coarser grid, which would amount to an h-type scale separation, or it may be defined by the respective polynomial orders (i.e., a p-type scale separation). In the numerical simulations presented in the original publication [119], the authors chose the second option, which is the reason to address it here in the context of the p-type scale separation. In fact, they used hexahedral elements with continuous triquadratic functions for the velocity approximation and discontinuous linear functions for the pressure approximation. This is an element definition well known to fulfill the inf-sup condition; see [93]. Discontinuous constant and linear functions are then chosen to represent the large-scale space $\overline{\mathcal{V}}_\gamma^h$, using L_2-orthogonal bases of piecewise Legendre polynomials. Mathematical analysis of such projection-based methods as described above was provided, e.g., in [40, 120, 186].

5.2.2 *h*-Type Scale Separation

An h-type scale separation relies on a level of complete resolution indicated by the characteristic discretization length h. With respect to this complete resolution level, a large-scale resolution level is identified a priori. This level is characterized by the length $\overline{h}$, where $\overline{h} > h$. Usually, this large-scale resolution level is a multiple of the complete resolution level, that is, $\overline{h} = \alpha h$, with typical values for the factor α being two or three, respectively. The separation of the velocity in the three-scale decomposition (38) is specified for this particular case of an h-type scale separation to be

$$\mathbf{u} = \underbrace{\overline{\mathbf{u}}^h + \delta\mathbf{u}^h}_{\mathbf{u}^h} + \hat{\mathbf{u}}, \tag{82}$$

where, according to Harten's notation [101], $\delta\mathbf{u}^h$ denotes the small-scale part, highlighting the fact that this small-scale part is indeed obtained as the difference between the complete resolved and the larger resolved scale:

$$\delta\mathbf{u}^h = \mathbf{u}^h - \overline{\mathbf{u}}^h. \tag{83}$$

Note that, typically, the h-type three-scale decomposition defined by (82) is merely applied to the velocity solution and weighting functions for the methods presented below, and a two-scale decomposition is kept up for the pressure solution and weighting function.

Three different variants of h-type scale separations for LES within the variational multiscale framework were proposed in the literature:

- a Volume-Agglomeration (VA) procedure according to [129] (realized within a mixed FEM/FVM),
- a Geometric MultiGrid (GMG) method as proposed in [79] (realized within an FVM) and
- an Algebraic MultiGrid (AMG) method as presented in [83] (realized within an FEM).

Crucial aspects for such h-type scale separations are, among others, the generation of grids and the actual way of separating the scales based on the generated grids, which will be detailed in the following. Although the aforementioned approaches were realized on the basis of a particular computational method, they are typically not restricted to that one.

Two alternative techniques for generating grids may be distinguished in principle: one generating the grid for the large-scale resolution level from the grid for the complete resolution level and one proceeding in the opposite direction (i.e., from the grid for the large-scale resolution level to the grid for the complete resolution level). For the VA procedure in [129], the problem domain is initially discretized by a grid with tetrahedral elements, from which a dual grid defined by control volumes is derived. This dual grid represents the grid for the complete resolution level. By a VA procedure as proposed in [132], macro-volumes are created. The characteristic large-scale length $\overline{h}$ and, hence, the ratio of $\overline{h}$ and h may be varied by varying the extension of the macro-volumes, which depends on the number of subsets of neighbors included in the macro-volumes.

For the GMG method in [79], two grids are created as well: a coarser grid, called the parent grid, and a finer grid, called the child grid, proceeding in the opposite direction, though. Starting from the parent grid, the child grid is obtained by an isotropic hierarchical subdivision of the parent grid. Typically, the factor α is chosen to be two, such that $\overline{h} = \alpha h = 2h$. The denotation "parent" and "child" mirrors usual namings in multigrid methods. However, in contrast to a usual parent-child relationship in multigrid solvers, where the parent needs to know only the number of its children, a complete parent-child data base needs to be set up. As a result, every parent knows about every child and vice versa.

The AMG-based method originally proposed in [84] and later used for LES within the variational multiscale framework for the first time in [83] makes use of aggregation- or agglomeration-based AMG as published in [212]. More precisely, the scale separation is based on level-transfer operators arising in Plain Aggregation Algebraic MultiGrid (PA-AMG); see, e.g., [141]. Though conceptually different, PA-AMG is closely related to the aforementioned VA methods; see, e.g., [132, 148]. Compared to GMG methods, AMG methods obviate the usually challenging generation of additional grids besides the basic one due to the

use of algebraic principles for the generation of prolongation and restriction (i.e., level-transfer) operator matrices. Here, a factor $\alpha = 3$ is usually chosen for the generation of aggregates, which will be described below, such that $\overline{h} = \alpha h = 3h$.

In [79], a general class of scale-separating operators based on multigrid operators was defined:

$$\overline{\mathbf{u}}^{h} = S^{\mathrm{m}}\left[\mathbf{u}^{h}\right] = P \circ R\left[\mathbf{u}^{h}\right] = P\left[\overline{\mathbf{u}}^{\overline{h}}\right], \tag{84}$$

where the multigrid scale-separating operator S^{m} consists of the sequential application of a restriction operator R and a prolongation operator P. Applying the restriction operator to $\mathbf{u}^{h}$ yields a large-scale velocity $\overline{\mathbf{u}}^{\overline{h}}$ defined at the degrees of freedom of the coarser grid, which is then prolongated to obtain a large-scale velocity $\overline{\mathbf{u}}^{h}$ defined at the degrees of freedom of the finer grid. Different restriction as well as prolongation operators were used for the aforementioned scale-separating approaches.

The restriction operator for the GMG method in [79] was defined to be a volume-weighted average over all child control volumes of one parent control volume subject to

$$\overline{\mathbf{u}}_{\overline{c}}^{\overline{h}} = R\left[\mathbf{u}_{c}^{h}\right]_{\overline{c}} = \frac{\sum_{c=1}^{n_{\mathrm{cop}}} V(\Omega^{c})\mathbf{u}_{c}^{h}}{\sum_{c=1}^{n_{\mathrm{cop}}} V(\Omega^{c})}, \tag{85}$$

where $\overline{\mathbf{u}}_{\overline{c}}^{\overline{h}}$ denotes the large-scale velocity at the center of the parent control volume $\overline{c}$ with domain $\overline{\Omega}^{\overline{c}}$, n_{cop} the number of child control volumes c with domain Ω^{c} in $\overline{\Omega}^{\overline{c}}$ and volume $V(\Omega^{c})$. Compared to a non-projective smoothed prolongation operator, superior results were obtained in [79] when using a projective prolongation operator in form of a constant prolongation defined by

$$\overline{\mathbf{u}}_{c}^{h} = P^{\mathrm{p}}\left[\overline{\mathbf{u}}_{\overline{c}}^{\overline{h}}\right]_{c} = \overline{\mathbf{u}}_{\overline{c}}^{\overline{h}} \tag{86}$$

for all $\Omega^{c} \subset \overline{\Omega}^{\overline{c}}$ and zero elsewhere. It was shown in [79] that the scale-separating operator defined as $S^{\mathrm{pm}} := P^{\mathrm{p}} \circ R$ is indeed a projector, indicated by the additional superscript "p". This projector is exactly the operator also used for the VA procedure in [129], although it was not derived from the general formulation (84) and hence not split up into a restriction and prolongation operator there. Moreover, this operator was also addressed in [215].

For the AMG method, PA-AMG is used for generating level-transfer operator matrices based on algebraic multigrid principles. The plain aggregation prolongation operator matrix is denoted by $\mathbf{P}_{3h}^{h}$, where the aforementioned factor $\alpha = 3$ is already made apparent by the subscript. It consists of first deriving its sparsity pattern and then specifying its non-zero values. The sparsity pattern is specified by decomposing the set of degrees of freedom associated with the respective system matrix on the basic grid level h, denoted here by $\mathbf{K}^{hh}$, into a set of so-called aggregates $\mathcal{A}_{i}^{h}$ such that

$$\bigcup_{i=1}^{n_{\mathrm{nb}}^{3h}} \mathcal{A}_{i}^{h} = \{1, ..., n_{\mathrm{dof}}^{h}\}, \ \mathcal{A}_{i}^{h} \cap \mathcal{A}_{j}^{h} = \emptyset \tag{87}$$

for all $1 \leq i, j \leq n_{\mathrm{nb}}^{3h}$ with $i \neq j$, where n_{dof}^{h} denotes the total number of degrees of freedom on level h and n_{nb}^{3h} is the total number of nodal blocks on level $3h$. A symbolic visualization of resulting aggregates is given in Fig. 1.

Each aggregate $\mathcal{A}_{i}^{h}$ is defined by its root node with all its associated degrees of freedom $d_{j}^{\mathcal{A}_{i}^{h}} \in \{1, ..., n_{\mathrm{dof}}^{h}\}$ and all adjacent degrees of freedom that share a non-zero off-diagonal entry with $d_{j}^{\mathcal{A}_{i}^{h}}$. Aggregates can be formed based on the connectivity and the strength of connections in $\mathbf{K}^{hh}$. For an overview of serial and parallel aggregation strategies, the reader is referred to [211, 212]. Populating the sparsity structure of $\mathbf{P}_{3h}^{h}$ derived from aggregation with appropriate values is the second step, which will not be outlined here for brevity, though. The reader is referred to [84] for more details.

The restriction operator matrix $\mathbf{R}_{h}^{3h}$ is chosen to be the transpose of the prolongation operator matrix:

$$\mathbf{R}_{h}^{3h} = \left(\mathbf{P}_{3h}^{h}\right)^{\mathrm{T}}. \tag{88}$$

It holds that

$$\mathbf{R}_{h}^{3h}\,\mathbf{P}_{3h}^{h} = \mathbf{I} \tag{89}$$

due to the disjoint construction of the adjacent aggregates (87), among others. A coarse-scale system matrix may then

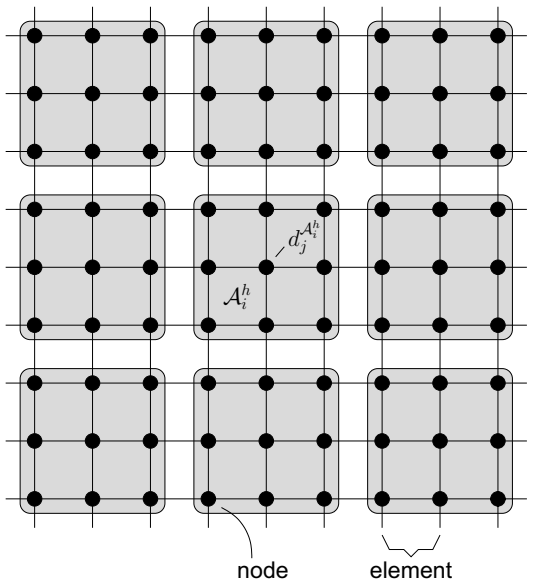

Fig. 1 Symbolic visualization of (plain) aggregates on a structured grid by *grey boxes*

be computed via the Galerkin product $\mathbf{K}^{3h3h} = \mathbf{R}_h^{3h}\mathbf{K}^{hh}\mathbf{P}_{3h}^h$ in a variationally consistent way.

A scale-separating operator matrix yielding the larger resolved scales is eventually defined as

$$\mathbf{S}_h^{3h} = \mathbf{P}_{3h}^h\mathbf{R}_h^{3h}. \tag{90}$$

The scale-separating operator matrix is applied to the discrete (i.e., nodal) values of the resolved velocity field. Using the usual finite element expansion of the resolved velocity field, which can be written as

$$\mathbf{u}^h = \sum_{A\in\mathcal{E}} N_A\mathbf{u}_A = \mathbf{N}\mathbf{U}^h, \tag{91}$$

the small-scale velocity field is obtained as

$$\delta\mathbf{u}^h = \sum_{\mathrm{A}\in\mathcal{E}} N_\mathrm{A}\delta\mathbf{u}_\mathrm{A}^h = \mathbf{N}\delta\mathbf{U}^h = \mathbf{N}\big[\mathbf{I} - \mathbf{S}_h^{3h}\big]\mathbf{U}^h. \tag{92}$$

Here, $\mathbf{U}^h$ denotes the vector of resolved velocity degrees of freedom $\mathbf{u}_A$, $\delta\mathbf{U}^h$ the vector of nodal values $\delta\mathbf{u}_\mathrm{A}^h$ of the small-scale velocity field, $\mathbf{N}$ a matrix containing the shape functions N_A and $\mathcal{E}$ the set of all nodes A of the discretization. The method with AMG-based h-type scale separation was named Algebraic Variational Multiscale–Multigrid Method (AVM^3) in [83], expressing its roots from both the VMM and AMG methods.

5.3 Small-Scale Subgrid-Viscosity Models

The majority of the aforementioned references used the rather simple constant-coefficient Smagorinsky model originally proposed in [196], one of the most popular functional models, as already mentioned in Sect. 2.3. Adopting the usual filter-based notation with filter width Δ to the present situation, where the resolved part of the velocity is defined by the discretization with characteristic length scale h, the subgrid viscosity can be expressed as

$$\nu_\mathrm{sgs} = \big(C_\mathrm{S}h\big)^2\|\boldsymbol{\varepsilon}(\mathbf{u}^h)\|, \tag{93}$$

where C_S denotes the constant parameter of the Smagorinsky model. There are several well-known weak points related to the Smagorinsky model, as already addressed in Sect. 2.3, which are related to the fact that it depends on this a priori unknown constant parameter C_S. Among others, the constant-coefficient Smagorinsky model is not a reasonable approach for the simulation of transitional flows, since it does not vanish in laminar regimes. Another problem with this model is the complete exclusion of any backscatter mechanism due to the strictly dissipative character of the model, which results in $\nu_\mathrm{sgs} \geq 0$ everywhere in the flow domain at any point in time.

Despite all these well-known flaws of the constant-coefficient Smagorinsky model, the integration of this simple model into the framework of the VMM has led to very good results for a number of test cases. The specific modification of the model restricting the dependence on the small scales as

$$\nu'_\mathrm{sgs} = \big(C_\mathrm{S}h\big)^2\|\boldsymbol{\varepsilon}(\mathbf{u}'^h)\|, \tag{94}$$

which was named small-small model in [110], appears to be the most natural version within the present multiscale framework. Other versions are a large-small model using only the large-scale part of the velocity for the calculation of the rate-of-deformation tensor $\boldsymbol{\varepsilon}$ in (94), which was mainly introduced for achieving some gain in computational efficiency in [110], and the use of the complete velocity as an all-small model.

The aforementioned drawbacks of the Smagorinsky model can be traced back to the preliminary fixing of the constant C_S. Therefore, it was proposed in [73] to "unfix" the constant and allow it to change in space and time (i.e., $C_\mathrm{S} = C_\mathrm{S}(\mathbf{x}, t)$) by way of a dynamic algorithm. The original idea was slightly modified in [140] and generalized to inhomogeneous flows in [76] by the introduction of a dynamic localization model. A consistent version for this dynamic localization model based on a variational formulation as given above was proposed in [78]. In [164], the so-called variational Germano identity for dynamic modeling was proposed in the context of turbulent incompressible flow; this idea was also later adopted in [60].

6 Multifractal Subgrid-Scale Modeling

The form of the cross- and subgrid-scale Reynolds-stress terms, (35) and (36), respectively, of the variational multiscale formulation (34) also suggests closure by a structural subgrid-scale model that directly provides an approximation for the subgrid-scale velocity. Therefore, the consideration of the multifractal subgrid-scale modeling approach, originally presented in [35, 36], was proposed in [180]. The resulting method is reviewed in the following, starting with a brief introduction into multifractal structures in turbulent flows.

6.1 Multifractals in Turbulent Flows

Gradient-magnitude fields in high-Reynolds-number flows, such as the kinetic-energy dissipation rate, the enstrophy and the scalar-variance diffusion rate, are subject to the repeated stretching and folding mechanism of the strain-rate and vorticity field. As a result of this multiplicative process, these fields show multifractal structures in the inertial subrange, which were identified both experimentally and numerically (see, e.g., [33, 151, 157, 174]). The

multifractal properties are reflected by the significant intermittent features observed for these fields. A comprehensive review of multifractal structures in turbulent flows as well as the related mathematical formalism can be found, e.g., in [201].

Multifractal structures emerge from the repeated application of a scale-invariant multiplicative process on an initial field. This process can be described by deterministic or stochastic multiplicative cascades. The considered field is mapped from one cell to smaller subcells in consecutive cascade steps. The set of multipliers $\mathcal{M}$, with $0 < \mathcal{M} < 1$, governing the (unequal) distribution of the field of interest contained in one cell among the corresponding subcells, can be either prescribed a priori or obtained randomly from a scale-invariant distribution $P(\mathcal{M})$, depending on whether a deterministic or stochastic cascade is considered. After a sufficient number of cascade steps, the generated field becomes highly intermittent and exhibits multifractal scaling properties. Furthermore, all fields obtained from one multiplier distribution $P(\mathcal{M})$ are statistically indistinguishable from each other.

The multiplicative cascade for an (integral) measure Θ, for instance, mass, is mathematically expressed as

$$\Theta(\mathbf{x}) = \Theta_0 \prod_{n=1}^{\mathcal{N}} \mathcal{M}_n(\mathbf{x}), \tag{95}$$

where Θ_0 denotes the total amount of the measure to be distributed within the considered domain and $\mathcal{N}$ the number of cascade steps. At each stage of the cascade, an n_{sd}-dimensional parent cell of size ϱ_{n-1} (e.g., the edge length for a square or a cube) is split into $n_{\mathrm{sc}}^{n_{\mathrm{sd}}}$ subcells of equal size ϱ_n, where n_{sc} is also called the base of the process. After $\mathcal{N}$ steps, the size $\varrho_{\mathcal{N}}$ of the smallest subcells is related to the size ϱ_0 of the initial cell via

$$\frac{\varrho_0}{\varrho_{\mathcal{N}}} = n_{\mathrm{sc}}^{\mathcal{N}}. \tag{96}$$

Expressed for a cell-averaged distributed measure ϑ (i.e., $\vartheta_n = \Theta_n/(\varrho_n)^{n_{\mathrm{sd}}}$), for instance, density, the multiplicative cascade reads

$$\vartheta(\mathbf{x}) = \vartheta_0 \left(n_{\mathrm{sc}}^{\mathcal{N}}\right)^{n_{\mathrm{sd}}} \prod_{n=1}^{\mathcal{N}} \mathcal{M}_n(\mathbf{x}). \tag{97}$$

For illustration, a one-dimensional stochastic binomial cascade, displayed in Fig. 2, is considered. In each step of

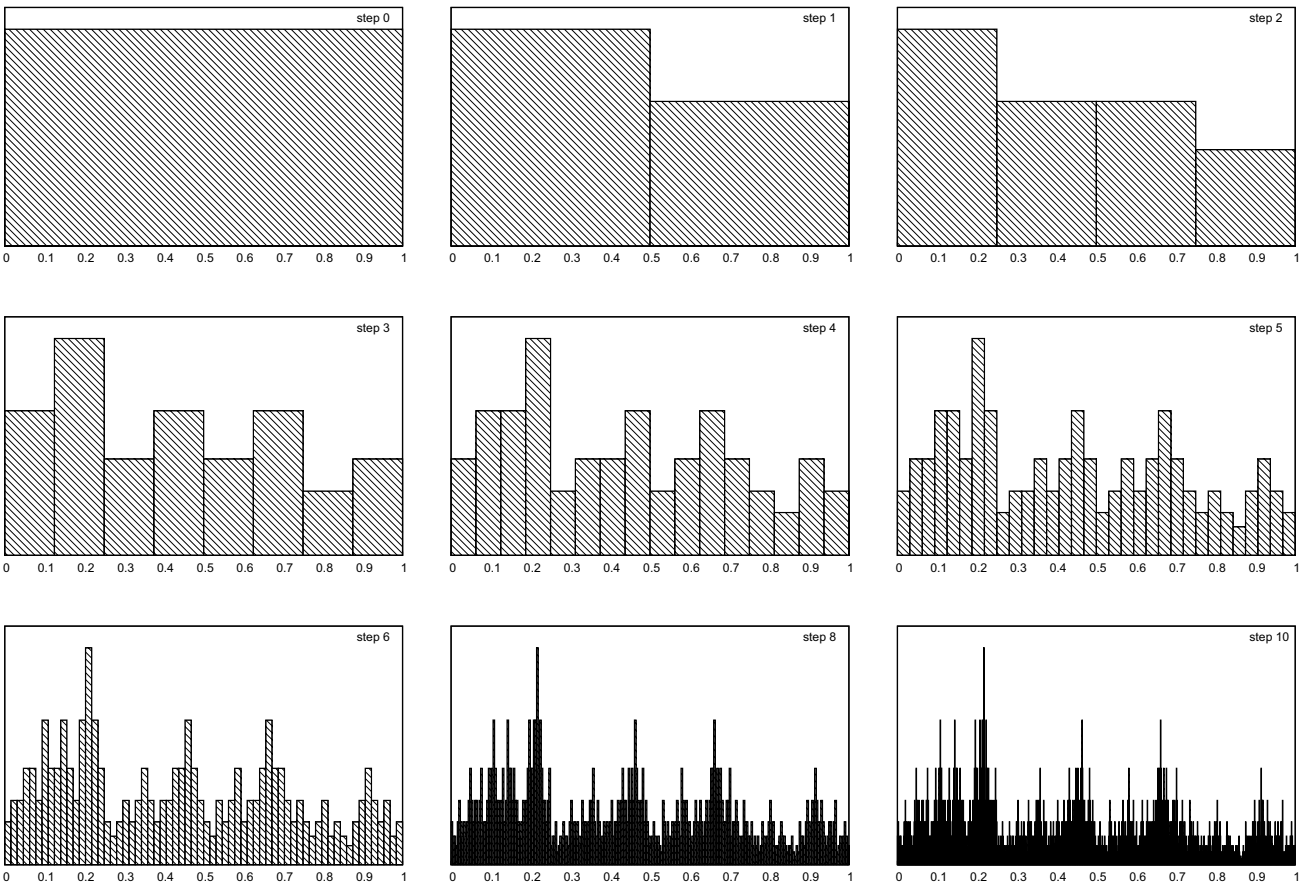

Fig. 2 One-dimensional stochastic binomial cascade with imposed conservation of the measure: initial field as well as resulting fields after $\mathcal{N} = 1, 2, 3, 4, 5, 6, 8$ and 10 cascade steps normalized by the respective maximum values

the process, the measure contained in one cell is divided between two subcells, each half the size of the parent cell. The scale-invariant distribution of the multipliers is given by δ-functions as

$$P(\mathcal{M}) = 0.5(\delta(\mathcal{M} - 0.4) + \delta(\mathcal{M} - 0.6)), \tag{98}$$

such that only two values are possible for $\mathcal{M}$. In every cascade step, conservation of the measure is enforced by randomly selecting the multiplier $\mathcal{M}_n$ for the first subcell and assigning the multiplier $1 - \mathcal{M}_n$ to the second one. Figure 2 depicts the initial field as well as the resulting fields after 1, 2, 3, 4, 5, 6, 8 and 10 cascade steps. All fields are scaled by their maximum value. When passing through the cascade, the intermittency is increased, and the field becomes concentrated onto successively smaller parts of the domain.

6.2 Modeling Strategy

The multifractal subgrid-scale modeling approach makes use of the vorticity $\boldsymbol{\omega}(\mathbf{x}, t)$, which is defined as

$$\boldsymbol{\omega} = \nabla \times \mathbf{u}, \tag{99}$$

and the enstrophy $Q(\mathbf{x}, t)$, given by

$$Q = \boldsymbol{\omega} \cdot \boldsymbol{\omega}. \tag{100}$$

Using a multifractal reconstruction of the subgrid-scale vorticity $\hat{\boldsymbol{\omega}}$ over inertial-subrange scales, the associated subgrid-scale velocity $\hat{\mathbf{u}}$ is recovered via the Biot–Savart operator:

$$\hat{\mathbf{u}}(\mathbf{x}, t) = \frac{1}{4\pi} \int \hat{\boldsymbol{\omega}}(\check{\mathbf{x}}, t) \times \frac{\mathbf{x} - \check{\mathbf{x}}}{\|\mathbf{x} - \check{\mathbf{x}}\|^3} \mathrm{d}\check{\mathbf{x}}. \tag{101}$$

The reconstruction of the subgrid-scale vorticity field, expressed via its magnitude $\|\hat{\boldsymbol{\omega}}\|(\mathbf{x}, t)$ and orientation vector $\hat{\mathbf{e}}_{\boldsymbol{\omega}}(\mathbf{x}, t)$ of unit length as

$$\hat{\boldsymbol{\omega}} = \|\hat{\boldsymbol{\omega}}\| \hat{\mathbf{e}}_{\boldsymbol{\omega}}, \tag{102}$$

consists of two steps. First, the magnitude $\|\hat{\boldsymbol{\omega}}\|$ of the subgrid-scale vorticity field is derived by a multiplicative cascade distributing the total subgrid-scale enstrophy within each element. In a second step, the orientation $\hat{\mathbf{e}}_{\boldsymbol{\omega}}$ of the subgrid-scale vorticity field is determined using an additive decorrelation cascade.

Both cascades start at a scale of the size of the element length h and proceed down to the viscous (or inner) length scale λ_ν. The viscous length scale λ_ν defines the scale at which the competing effects of local strain rates and viscous diffusion are in equilibrium; see, e.g., [27, 157]. Assuming that each parent element decays into two child elements per spatial direction, i.e., $n_{\mathrm{sc}} = 2$, which is a reasonable value for turbulent flow (see, e.g., [64, 202]), the number of steps $\mathcal{N}_{\mathbf{u}}$ of both cascades is given by the ratio of the element length h to the viscous length scale λ_ν via

$$\mathcal{N}_{\mathbf{u}} = \log_2 \left(\frac{h}{\lambda_\nu} \right), \tag{103}$$

which follows directly from Eq. (96). The local element Reynolds number Re_h enables a scaling for the ratio of the element length to the viscous length scale as

$$\frac{h}{\lambda_\nu} \sim \mathrm{Re}_h^{\frac{3}{4}}. \tag{104}$$

6.3 Vorticity-Magnitude Cascade

The magnitude of the subgrid-scale vorticity $\|\hat{\boldsymbol{\omega}}\|$ in each subelement of the size of the viscous length scale is derived from the distribution of the total subgrid-scale enstrophy contained in the considered element. Therefore, the average subgrid-scale enstrophy $\hat{Q}$ over the element is estimated using the inertial-subrange scaling of the enstrophy spectrum:

$$Z_Q(k) \sim \varepsilon^{\frac{2}{3}} k^{\frac{1}{3}}. \tag{105}$$

The required proportionality constant in relation (105) is eliminated by determining $\hat{Q}$ as a function of the average enstrophy δQ^h at the smaller resolved scales, i.e., a scale range between h and a larger length scale $\overline{h} = \alpha h$, where $\alpha > 1$, which is assumed to be located in the inertial subrange. As in Sect. 5.2.2, quantities corresponding to the larger resolved scales are marked by $\overline{(\cdot)}^h$ and quantities associated with the smaller resolved scales by $\delta(\cdot)^h$. Figure 3 depicts the enstrophy spectrum, including the inertial-subrange scaling, as well as its decomposition according to the introduced scale ranges. The enstrophy spectrum is integrated both from the wave number k_h associated with the basic discretization to the viscous wave number k_ν

$$\hat{Q} = \int_{k_h}^{k_\nu} c_Q \varepsilon^{\frac{2}{3}} k^{\frac{1}{3}} \mathrm{d}k, \tag{106}$$

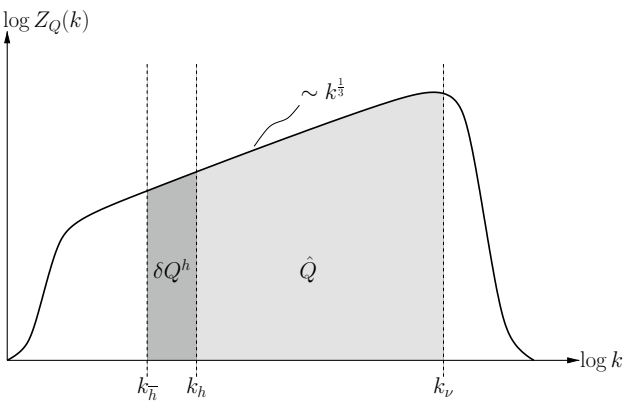

Fig. 3 Decomposition of enstrophy spectrum

where $c_Q > 0$ is the associated proportionality constant, and from the smaller wave number $k_{\overline{h}}$ to k_h

$$\delta Q^h = \int_{k_{\overline{h}}}^{k_h} c_Q \varepsilon^{\frac{2}{3}} k^{\frac{1}{3}} \mathrm{d}k, \tag{107}$$

which enables a formulation for the subgrid-scale enstrophy depending on the enstrophy of the smaller resolved scales:

$$\hat{Q} = \left(1 - \alpha^{-\frac{4}{3}}\right)^{-1} \left[\left(\frac{k_\nu}{k_h}\right)^{\frac{4}{3}} - 1\right] \delta Q^h. \tag{108}$$

The enstrophy at the smaller resolved scales is obtained from the resolved velocity field. Therefore, the resolved velocity $\mathbf{u}^h$ is further decomposed as given in Eq. (82), where the larger resolved velocity scales $\overline{\mathbf{u}}^h$ are obtained by explicitly separating the velocity field at a scale $\overline{h} = \alpha h$. By this decomposition, the enstrophy is formally split up as

$$\begin{aligned} Q = {} & \overline{\boldsymbol{\omega}}^h \cdot \overline{\boldsymbol{\omega}}^h + \delta\boldsymbol{\omega}^h \cdot \delta\boldsymbol{\omega}^h + \hat{\boldsymbol{\omega}} \cdot \hat{\boldsymbol{\omega}} \\ & + 2\left(\overline{\boldsymbol{\omega}}^h \cdot \delta\boldsymbol{\omega}^h + \overline{\boldsymbol{\omega}}^h \cdot \hat{\boldsymbol{\omega}} + \delta\boldsymbol{\omega}^h \cdot \hat{\boldsymbol{\omega}}\right). \end{aligned} \tag{109}$$

The enstrophies $\overline{Q}^h$, δQ^h and $\hat{Q}$, associated with the three scale ranges, are identified as

$$\overline{Q}^h = \overline{\boldsymbol{\omega}}^h \cdot \overline{\boldsymbol{\omega}}^h, \tag{110}$$

$$\delta Q^h = \delta\boldsymbol{\omega}^h \cdot \delta\boldsymbol{\omega}^h, \tag{111}$$

$$\hat{Q} = \hat{\boldsymbol{\omega}} \cdot \hat{\boldsymbol{\omega}}. \tag{112}$$

Averages over the cross terms are neglected owing to the decorrelation of widely separated scales in the vorticity field.

A three-dimensional stochastic multiplicative cascade (97) distributes the average subgrid-scale enstrophy as given in Eq. (108) along with Eqs. (110) and (112) over each element. This results in the following expression for the magnitude of the subgrid-scale vorticity in each subelement of the size of the viscous length scale:

$$\begin{aligned} \|\hat{\boldsymbol{\omega}}\|(\mathbf{x}, t) = {} & \left[\left(1 - \alpha^{-\frac{4}{3}}\right)^{-1} \left(\left(\frac{k_\nu}{k_h}\right)^{\frac{4}{3}} - 1\right)\right. \\ & \left. \times \left(2^{\mathcal{N}_\mathbf{u}}\right)^3 \prod_{n=1}^{\mathcal{N}_\mathbf{u}} \mathcal{M}_n(\mathbf{x}, t)\right]^{\frac{1}{2}} \|\delta\boldsymbol{\omega}^h\|. \end{aligned} \tag{113}$$

6.4 Vorticity-Orientation Cascade

The second cascade, which describes the reconstruction of the orientation $\hat{\mathbf{e}}_{\boldsymbol{\omega}}$ of the subgrid-scale vorticity, is likewise based on physical reasoning. Various experimental and computational studies indicate that the velocity fields of adjacent scale ranges are highly correlated; see, e.g, [6, 7] for early investigations of scale similarities in the context of LES, [143] for a comprehensive experimental study and [150] for a review. Building on these findings, the orientation $\hat{\mathbf{e}}_{\boldsymbol{\omega}}$ in the subgrid-scale vorticity field is assumed to decorrelate at successively smaller scales from the local orientation $\delta\mathbf{e}^h_{\boldsymbol{\omega}}$ of the smaller resolved scales. Accordingly, the additive cascade is given as

$$\hat{\mathbf{e}}_{\boldsymbol{\omega}}(\mathbf{x}, t) = \delta\mathbf{e}^h_{\boldsymbol{\omega}} + \sum_{n=1}^{\mathcal{N}_\mathbf{u}} \boldsymbol{\delta}_n(\mathbf{x}, t), \tag{114}$$

where $\boldsymbol{\delta}_n$ denotes stochastic-decorrelation increments between adjoining scale ranges. Consistent with the isotropy observed at the smallest scales in high-Reynolds-number flows, the cascade leads to an increasingly isotropic decorrelation of the subgrid-scale orientations from the element length scale to the viscous length scale. At each stage n of the cascade, $\boldsymbol{\delta}_n$ is defined by two stochastic spherical decorrelation angles ψ and β. Figure 4 shows a single step of the additive decorrelation cascade, leading to $\hat{\mathbf{e}}_{\boldsymbol{\omega},n}$ at the current stage n. Assuming $\hat{\mathbf{e}}_{\boldsymbol{\omega},n-1} = (0, 0, 1)^\mathrm{T}$ for the orientation vector of the preceding stage $n-1$, the components of $\boldsymbol{\delta}_n$ are given by

$$\boldsymbol{\delta}_n = \begin{pmatrix} \sin\psi \cos\beta \\ \sin\psi \sin\beta \\ \cos\psi - 1 \end{pmatrix}. \tag{115}$$

An isotropic probability distribution is assumed for β, as also implied in Fig. 4, such that ψ quantifies the decorrelation of the vorticity orientation at two adjoining scales in the subgrid-scale field. Evaluation of DNS data in [35] revealed correlations between the probability distribution of ψ and the value of the multiplier $\mathcal{M}_n$. While there is only a weak correlation between the orientation vectors at two successive scales for lower multiplier values, the vectors $\hat{\mathbf{e}}_{\boldsymbol{\omega},n-1}$ and $\hat{\mathbf{e}}_{\boldsymbol{\omega},n}$ are almost identical for higher ones. This behavior reflects the observation that the strongest vortical structures, which are identified by larger multiplier values,

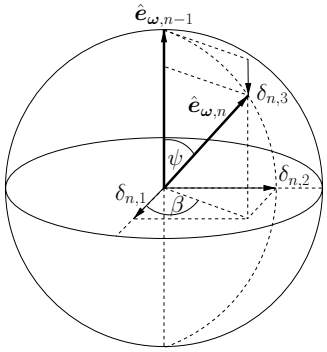

Fig. 4 Single step of additive decorrelation cascade

display a preferred alignment with the local strain rate tensor over a relatively large range of scales.

As a result of these considerations, an intermittency factor $\mathcal{I}_{\boldsymbol{\omega}}$ can be defined from a correlation between $\hat{\boldsymbol{\omega}}$ and $\delta\boldsymbol{\omega}^h$ as

$$\mathcal{I}_{\boldsymbol{\omega}} = \frac{\int \hat{\boldsymbol{\omega}} \cdot \delta\boldsymbol{\omega}^h \mathrm{d}\mathbf{x}}{\int \|\hat{\boldsymbol{\omega}}\| \, \|\delta\boldsymbol{\omega}^h\| \mathrm{d}\mathbf{x}}, \tag{116}$$

where $\mathcal{I}_{\boldsymbol{\omega}}$ is expected to depend on the number of cascade steps $\mathcal{N}_{\mathbf{u}}$ in the decorrelation cascade. The orientation of the subgrid-scale vorticity after $\mathcal{N}_{\mathbf{u}}$ cascade steps can then be reformulated using the intermittency factor $\mathcal{I}_{\boldsymbol{\omega}}$:

$$\hat{\mathbf{e}}_{\boldsymbol{\omega}}(\mathbf{x}, t) = \mathcal{I}_{\boldsymbol{\omega}} \delta\mathbf{e}^h_{\boldsymbol{\omega}} + \left(1 - \mathcal{I}_{\boldsymbol{\omega}}\right) \sum_{n=1}^{\mathcal{N}_{\mathbf{u}}} \boldsymbol{\delta}^*_n(\mathbf{x}, t), \tag{117}$$

where $\boldsymbol{\delta}^*_n$ are modified decorrelation increments due to the introduction of the intermittency factor $\mathcal{I}_{\boldsymbol{\omega}}$, which will be further specified below.

6.5 Subgrid-Scale Velocity Approximation

The combination of cascades (113) and (117) yields the subgrid-scale vorticity $\hat{\boldsymbol{\omega}}$, which is a stochastic field due to the stochastic nature of both the multipliers and the modified decorrelation increments. Assuming that (i) the correlations between $\mathcal{M}_n$ and $\boldsymbol{\delta}^*_n$ are sufficiently weak, (ii) the decorrelation cascade is isotropic (i.e., the expectation value of $\boldsymbol{\delta}^*_n$ vanishes) and (iii) the multipliers are statistically independent, the subgrid-scale vorticity $\hat{\boldsymbol{\omega}}$, which is taken to be approximately equal to its expectation value, may be simplified as

$$\begin{aligned}\hat{\boldsymbol{\omega}}(\mathbf{x}, t) = &\left[\left(1 - \alpha^{-\frac{4}{3}}\right)^{-1} \left(\left(\frac{k_\nu}{k_h}\right)^{\frac{4}{3}} - 1\right)\right. \\ &\left. \times \left(2^{\mathcal{N}_{\mathbf{u}}}\right)^3\right]^{\frac{1}{2}} \left\langle \mathcal{M}^{\frac{1}{2}} \right\rangle^{\mathcal{N}_{\mathbf{u}}} \mathcal{I}_{\boldsymbol{\omega}} \delta\boldsymbol{\omega}^h(\mathbf{x}, t),\end{aligned} \tag{118}$$

with the expectation value $\langle \mathcal{M}^{\frac{1}{2}} \rangle$ for the square root of the multipliers. After introducing expression (118) into the Biot–Savart operator (101), the subgrid-scale velocity can be computed as

$$\begin{aligned}\hat{\mathbf{u}}(\mathbf{x}, t) = &\left(1 - \alpha^{-\frac{4}{3}}\right)^{-\frac{1}{2}} 2^{\frac{3\mathcal{N}_{\mathbf{u}}}{2}} \left(2^{\frac{4\mathcal{N}_{\mathbf{u}}}{3}} - 1\right)^{\frac{1}{2}} \\ &\times \left\langle \mathcal{M}^{\frac{1}{2}} \right\rangle^{\mathcal{N}_{\mathbf{u}}} \mathcal{I}_{\boldsymbol{\omega}} \delta\mathbf{u}^h(\mathbf{x}, t),\end{aligned} \tag{119}$$

where it is assumed that the distribution $P(\mathcal{M})$ is independent of $\mathbf{x}$. Moreover, k_ν/k_h is replaced by using Eq. (103). In the high-Reynolds-number limit, a proper behavior of the model has to be ensured. Therefore, the subgrid-scale velocity $\hat{\mathbf{u}}$ should become independent of Re_h for $\mathrm{Re}_h \to \infty$ and, consequently, $\mathcal{N}_{\mathbf{u}} \to \infty$, implying the following scaling for the intermittency factor subject to $\mathcal{N}_{\mathbf{u}}$:

$$\mathcal{I}_{\boldsymbol{\omega}}(\mathcal{N}_{\mathbf{u}}) \sim 2^{-\left(\frac{2}{3}+\frac{3}{2}\right)\mathcal{N}_{\mathbf{u}}} \left\langle \mathcal{M}^{\frac{1}{2}} \right\rangle^{-\mathcal{N}_{\mathbf{u}}}. \tag{120}$$

Finally, the subgrid-scale velocity $\hat{\mathbf{u}}$ reads as

$$\hat{\mathbf{u}}(\mathbf{x}, t) = B \delta\mathbf{u}^h(\mathbf{x}, t), \tag{121}$$

where

$$B = C^B_{\mathrm{sgs}} \left(1 - \alpha^{-\frac{4}{3}}\right)^{-\frac{1}{2}} 2^{-\frac{2\mathcal{N}_{\mathbf{u}}}{3}} \left(2^{\frac{4\mathcal{N}_{\mathbf{u}}}{3}} - 1\right)^{\frac{1}{2}}. \tag{122}$$

The parameter C^B_{sgs} is the associated proportionality constant. Approximation (121) depends on the smaller resolved velocity $\delta\mathbf{u}^h$, covering the scales between h and a larger length scale $\bar{h} = \alpha h$. To extract the smaller resolved velocity from $\mathbf{u}^h$, the application of level-transfer operators from PA-AMG as introduced in Sect. 5.2.2 was suggested in [180]. Hence, $\alpha = 3$ is chosen in this case.

Using approximation (121), the modeled forms of the cross- and subgrid-scale Reynolds-stress terms, (35) and (36), read

$$\begin{aligned}&C(\mathbf{v}^h;\mathbf{u}^h, \hat{\mathbf{u}}) \approx \\ &\left(\mathbf{v}^h, \mathbf{u}^h \cdot \nabla\left(B\delta\mathbf{u}^h\right) + B\delta\mathbf{u}^h \cdot \nabla\mathbf{u}^h\right)_{\Omega^*},\end{aligned} \tag{123}$$

$$\mathcal{R}(\mathbf{v}^h;\hat{\mathbf{u}}) \approx \left(\mathbf{v}^h, B\delta\mathbf{u}^h \cdot \nabla\left(B\delta\mathbf{u}^h\right)\right)_{\Omega^*}. \tag{124}$$

The remaining terms containing unresolved-scale quantities are not incorporated by multifractal subgrid-scale modeling.

6.6 Number of Cascade Steps and Model Parameters

To compute the subgrid-scale velocity from Eqs. (121) and (122), the necessary number of cascade steps has to be defined, and a proper value for the proportionality constant C^B_{sgs} has to be chosen. According to Eq. (103), the number of cascade steps is given by the ratio of the element length to the viscous length scale, which in turn can be approximated by the local element Reynolds number Re_h. The respective relation (104) requires a proper definition of Re_h as well as the introduction of a proportionality constant c_ν, i.e.,

$$\frac{h}{\lambda_\nu} = c_\nu \mathrm{Re}_h^{\frac{3}{4}}. \tag{125}$$

Possible definitions for the element Reynolds number are:

- based on the strain rate tensor, as proposed in [35],

$$\mathrm{Re}^{\mathrm{S}}_h = \frac{\left(\boldsymbol{\varepsilon}(\mathbf{u}^h):\boldsymbol{\varepsilon}(\mathbf{u}^h)\right)^{\frac{1}{2}} h^2}{\nu} \tag{126}$$

- and based on the resolved velocity, as suggested in [180],

$$\mathrm{Re}_h^{\mathrm{R}} = \frac{\|\mathbf{u}^h\| h}{\nu}. \tag{127}$$

The element length h may be approximated by the cubic root of the element volume $V(\Omega^e)$ as done in [180]:

$$h = (V(\Omega^e))^{\frac{1}{3}}. \tag{128}$$

For setting $1/c_\nu$, results from experimental studies are considered. Among others, the experimental study in [157] aimed at estimating $1/c_\nu$ from direct measurements of the enstrophy field in a turbulent flow. In that study, a mean value of $\langle 1/c_\nu \rangle = 12.3$ was reported. In an earlier experimental work in [27], $\langle 1/c_\nu \rangle = 11.2$ was obtained indirectly from measurements in scalar fields. Based on these values, $c_\nu = 0.1$ was assumed for LES in [180].

In [35], C_{sgs}^B was first introduced as a universal constant, and it was suggested that $C_{\mathrm{sgs}}^B \approx 0.37$, resulting from a priori investigations of DNS data for forced homogeneous isotropic turbulence. However, subsequent applications (see, e.g., [34, 36, 180]) indicated a Reynolds-number dependence of C_{sgs}^B which reflects a proportionality to the subgrid-scale energy transfer. The corresponding function should approach a finite value in the high-Reynolds-number limit (i.e., $\mathrm{Re} \to \infty$) and tend to zero as $\mathrm{Re} \to 1$.

In [180], this aspect was further addressed in the context of the application of the multifractal subgrid-scale modeling approach to wall-bounded turbulent flow. Therefore, an enhancement of the multifractal subgrid-scale modeling, referred to as near-wall limit, was derived for wall-resolved LES in [180] to particularly account for the involved near-wall effects. Important aspects of wall-bounded turbulent flow, affecting the multifractal subgrid-scale modeling, are the decrease of the local element Reynolds number as the wall is approached as well as the higher anisotropy of the vorticity field in the near-wall region. The reduction in Re_h results in a decrease of the number of cascade steps, which in turn leads to a significant decrease of B towards the wall. As the local element Reynolds number should decrease towards the wall, definition (127) based on the norm of the resolved velocity was considered particularly appropriate for this flow type in [180].

As aforementioned, the vorticity field becomes highly anisotropic in the near-wall region. This strong anisotropy leads to strong correlations in the orientation of the subgrid-scale vorticity. These stronger correlations in turn cause an increase of the intermittency factor $\mathcal{I}_{\boldsymbol{\omega}}$, which is defined by the correlation between the subgrid-scale vorticity and the vorticity of the smaller resolved scales. In equation (120), the intermittency factor $\mathcal{I}_{\boldsymbol{\omega}}$ has only been determined up to the proportionality constant C_{sgs}^B. Precisely this factor allows for modifying the derivation of the multifractal subgrid-scale modeling approach to provide a near-wall limit. Higher intermittency factors $\mathcal{I}_{\boldsymbol{\omega}}$ owing to stronger correlations are associated with an increase of C_{sgs}^B. Therefore, C_{sgs}^B becomes non-uniform and also depends on local flow features.

Based on these considerations, C_{sgs}^B is multiplied by an anisotropy factor f_{ai} for wall-bounded turbulent flow, yielding an enhanced proportionality coefficient $C_{\mathrm{sgs}}^{B,\mathrm{nw}}$:

$$C_{\mathrm{sgs}}^{B,\mathrm{nw}} = f_{\mathrm{ai}} C_{\mathrm{sgs}}^B. \tag{129}$$

The aforementioned limits of C_{sgs}^B depending on the Reynolds number have to be maintained by the enhanced parameter $C_{\mathrm{sgs}}^{B,\mathrm{nw}}$. The intermittency factor $\mathcal{I}_{\boldsymbol{\omega}}$ is bounded as $0 \leq \mathcal{I}_{\boldsymbol{\omega}} \leq 1$. Furthermore, the norm of the strain rate tensor is taken to be an appropriate measure for anisotropy. Combing all three requirements, the following form of the anisotropy factor for wall-bounded turbulent flow was suggested in [180]:

$$f_{\mathrm{ai}} = \left(1 - \left(\mathrm{Re}_h^{\mathrm{S}}\right)^{-\frac{3}{16}}\right), \tag{130}$$

where the element Reynolds number according to Eq. (126) is used. The exponent $-3/16$ was defined based on applications to wall-bounded flow problems. In doing so, the element Reynolds number is introduced into the final proportionality coefficient $C_{\mathrm{sgs}}^{B,\mathrm{nw}}$. According to [180], this procedure allows for a fixed value for C_{sgs}^B for a wide range of Reynolds numbers and resolutions. The parameter C_{sgs}^B was set to 0.25 in [180].

6.7 Residual-Based Subgrid-Scale Modeling

The multifractal subgrid-scale modeling approach introduced so far is based on physical reasoning. In particular, the multifractal subgrid-scale modeling approach aims at capturing the physical interaction that leads to the actual energy transfer between the larger and the smaller scales in turbulent flows, i.e., the resolved and the subgrid scales in the respective LES. Therefore, it is not purely dissipative and allows for physical backscatter of energy, among other things. An introduction of additional artificial (or subgrid-scale) dissipation to also stabilize numerical schemes is not intended by the multifractal subgrid-scale modeling approach. In fact, incorporating the multifractal subgrid-scale approximation into the variational multiscale formulation does not ensure the stability of the final numerical method in general. Therefore, potentially

destabilizing effects induced by the numerical scheme have to be accounted for otherwise, as elaborately discussed in [36]. For the multifractal subgrid-scale modeling approach in its original form, a backscatter limiter was proposed in [36] and in a more advanced adaptive form in [34] to overcome this limitation.

In [180], the multifractal subgrid-scale modeling approach was embedded into a residual-based variational multiscale formulation. A mathematically solid foundation, as outlined in Sect. 4, renders residual-based subgrid-scale approximations, which lead to stabilized methods, a reliable means for taking care of stability issues not addressed by the multifractal subgrid-scale modeling. Hence, the following solely numerically motivated stabilization terms are included:

$$\begin{aligned}&\mathcal{B}_{\text{RBStab}}(\mathbf{v}^h,q^h;\mathbf{u}^h,p^h_{\text{kin}}) := \left(\mathbf{u}^h\cdot\nabla\mathbf{v}^h,\tau_{\text{M}}\mathbf{r}^h_{\text{M}}\right)_{\Omega^*}\\&+\left(\nabla q^h,\tau_{\text{M}}\mathbf{r}^h_{\text{M}}\right)_{\Omega^*}+\left(\nabla\cdot\mathbf{v}^h,\tau_{\text{C}}r^h_{\text{C}}\right)_{\Omega^*}.\end{aligned}\tag{131}$$

As shown in Eq. (66), the PSPG and grad-div term emanate from $\mathcal{B}^{1,\text{lin}}_{\text{NS}}(\mathbf{v}^h,q^h;\hat{\mathbf{u}},\hat{p}_{\text{kin}})$, which has not been addressed by the multifractal subgrid-scale modeling. The SUPG term, formally arsing from $C(\mathbf{v}^h;\mathbf{u}^h,\hat{\mathbf{u}})$, as explained in Sect. 4.4, provides convective stabilization and, hence, the necessary dissipation on the subgrid-scale level. Since the terms given in Eq. (131) arise from a residual-based approximation of the subgrid scales, their inclusion may also be interpreted as a second subgrid-scale modeling step.

6.8 The Algebraic Variational Multiscale–Multigrid–Multifractal Method

Inserting expressions (123), (124) as well as (131) into Eq. (34), the modeled variational multiscale formulation is given as follows: find $(\mathbf{u}^h,p^h_{\text{kin}})\in S^h_{\mathbf{u}}\times S^h_p$ such that

$$\begin{aligned}&\mathcal{B}_{\text{NS}}(\mathbf{v}^h,q^h;\mathbf{u}^h,p^h_{\text{kin}})\\&+\left(\mathbf{v}^h,\mathbf{u}^h\cdot\nabla\left(B\delta\mathbf{u}^h\right)+B\delta\mathbf{u}^h\cdot\nabla\mathbf{u}^h\right)_{\Omega^*}\\&+\left(\mathbf{v}^h,B\delta\mathbf{u}^h\cdot\nabla\left(B\delta\mathbf{u}^h\right)\right)_{\Omega^*}\\&+\left(\mathbf{u}^h\cdot\nabla\mathbf{v}^h,\tau_{\text{M}}\mathbf{r}^h_{\text{M}}\right)_{\Omega^*}+\left(\nabla q^h,\tau_{\text{M}}\mathbf{r}^h_{\text{M}}\right)_{\Omega^*}\\&+\left(\nabla\cdot\mathbf{v}^h,\tau_{\text{C}}r^h_{\text{C}}\right)_{\Omega^*}=\ell_{\text{NS}}(\mathbf{v}^h)\end{aligned}\tag{132}$$

for all $(\mathbf{v}^h,q^h)\in\mathcal{V}^h_{\mathbf{u}}\times\mathcal{V}^h_p$. The multifractal subgrid-scale modeling terms are show in the second and third line and the residual-based stabilization terms in the fourth and fifth line (first term). This formulation combines all ingredients presented in the preceding sections, that is,

- the derivation within the framework of the VMM,
- the evaluation of the subgrid-scale velocity based on the multifractal subgrid-scale modeling approach,
- the identification of the required smaller resolved scales by level-transfer operators from PA-AMG and
- the inclusion of additional residual-based stabilization terms to primarily shield against potentially destabilizing effects due to the numerical scheme.

The resulting method was thus referred to as the Algebraic Variational Multiscale–Multigrid–Multifractal Method (AVM^4) in [180].

7 Comparison of Variational Multiscale Methods for Incompressible Flow

To asses the performance of approaches to LES, they are commonly applied to classical benchmark examples of canonical flow type, such as homogeneous isotropic turbulence and turbulent channel flow. These test cases were also considered for validating the various VMMs introduced in the preceding sections and for comparing them to each other. In the following, first, an overview of the respective studies will be given. As turbulent channel flow appears to be the numerical example mostly used in the literature for evaluating the computational methods discussed in this review, we will choose this flow problem exemplarily for showing selected computational results in the second part of this section.

7.1 Overview

The RBVMM exemplified in Sect. 4.4 was investigated for forced homogeneous isotropic turbulence and turbulent channel flow in [9]. Instead of using standard finite element shape functions, Non-Uniform Rational B-Splines (NURBS) shape functions of various orders were applied in that study. Its extension by time-dependent subgrid-scale approximations was investigated for LES of turbulent channel flow in [68]. For the considered range of time-step lengths, the time-dependent approach did not provide significantly better results than the quasi-static one. Recently, another comparative study on RBVMMs for LES of turbulent incompressible flow was provided in [52]. In that study, time-dependent and quasi-static subgrid-scales with and without L_2-projection of the residuals orthogonal to the finite element space were distinguished. Additionally, formulations without cross- and subgrid-scale Reynolds-scale terms were considered for the time-dependent cases. Three different benchmark examples were investigated: decaying homogeneous isotropic turbulence, the Taylor–Green vortex and turbulent channel flow. Overall, similar results were obtained for all methods. However, the authors observed that the results were sensitive to the scaling coefficients of the stabilization parameters. In particular, they omitted the grad-div term, which introduces strictly positive numerical dissipation. In contrast, the numerical dissipation of the

SUPG term, the second cross-stress term and the subgrid-scale Reynolds-stress term can locally be either positive or negative. Their averaged dissipation rate is always positive, though. This behavior reflects (local) backscatter of energy, commonly not taken into account in ILES approaches; see [52].

In [91], the VMM with explicit solution of large- and small-scale equation based on residual-free bubbles, presented in Sect. 5.1, was applied to turbulent recirculating flow in a lid-driven cavity and to a plane two-dimensional mixing layer. Moreover, the small-scale subgrid viscosity was determined dynamically by using an additional sub-submesh. The L_2-projection-based VMM with p-type scale separation, reviewed in Sect. 5.2.1, was tested for turbulent channel flow, a plane three-dimensional mixing layer and turbulent flow past a square-section cylinder in [119]. A comparison of these two aforementioned VMMs was shown for turbulent channel flow in [121]. The evaluations of the L_2-projection-based VMM revealed that the results are more sensitive to the choice of the large-scale space than to the small-scale subgrid-scale viscosity model, as outlined Sect. 5.3. Several deficiencies of the VMM with explicit solution of large- and small-scale equation were also detected in [121]. The parameter of the Smagorinsky model had to be chosen rather large for the coarse submeshes used in that study. Furthermore, a blow-up of the VMM with explicit solution of large- and small-scale equation was observed for simulations without grad-div term. The introduction of the grad-div term as a subgrid-scale model for the pressure into the L_2-projection-based VMM was later considered in [186] and examined for decaying homogeneous isotropic turbulence. For this example, the grad-div term appeared to be rather unimportant. An adaptive large-scale space allowing for an increase or attenuation of the direct influence of the small-scale subgrid viscosity term depending on the local flow structures was suggested in [122] and investigated for turbulent channel flow and turbulent flow past a square-section cylinder. For turbulent channel flow, somewhat improved results compared to the basic method with fixed large-scale space were obtained.

The VMM with h-type scale separation based on a VA procedure, described in Sect. 5.2.2, was applied to turbulent flow past a square-section cylinder in [129] as well as its dynamic version to turbulent flow past a prolate spheroid and a forward swept scaled wing in [60]. In [79], the VMM with h-type scale separation based on a GMG method was investigated for turbulent channel flow, and later in [81], for turbulent flow in an asymmetric diffuser. Results obtained with the methods proposed in [60, 79, 129] were compared to constant-coefficient as well as dynamic Smagorinsky models applied in the traditional way (i.e., acting on all scales), among others. Notably improved predictions could be achieved particularly for turbulent channel flow and turbulent flow past a square-section cylinder when checking them against, for instance, DNS and experimental data. In [83], the AVM^3 was applied to turbulent channel flow and turbulent recirculating flow in a lid-driven cavity. In a subsequent study in [85], turbulent flow past a square-section cylinder was investigated. Since trilinearly interpolated hexahedral elements were used for the velocity and the pressure field, a PSPG term was additionally included. Although the SUPG and the grad-div term were actually not required, the application to turbulent recirculating flow in a lid-driven cavity as well as to turbulent flow past a square-section cylinder revealed their beneficial impact on the convergence of the iterative solution procedure. While the AVM^3 performed only slightly better than the considered RBVMM with quasi-static subgrid-scales for the latter two test cases, notably improved results were observed for turbulent channel flow when using the AVM^3.

Applications of the AVM^4 to forced homogeneous isotropic turbulence may be found in [177] and to turbulent channel flow at friction Reynolds numbers up to 950, turbulent flow over a backward-facing step as well as past a square-section cylinder in [180]. Additionally, results obtained with the RBVMM as suggested in [9] were considered for a comparison. Particularly for turbulent channel flow, the AVM^4 produced results significantly closer to reference results from DNS than the considered RBVMM.

7.2 Application to Turbulent Channel Flow

Turbulent channel flow, as considered in most of the aforementioned studies, is characterized by the friction Reynolds number,

$$\mathrm{Re}_\tau = \frac{u_\tau \delta_\mathrm{c}}{\nu} \tag{133}$$

which is defined based on the channel half-width δ_c and the friction velocity,

$$u_\tau = \sqrt{\frac{\tau_\mathrm{W}}{\rho}} \tag{134}$$

where τ_W denotes the wall-shear stress and ρ the density. No-slip boundary conditions are imposed at the top and the bottom wall. Periodic boundary conditions are assumed in homogeneous streamwise and spanwise directions. A constant pressure gradient in streamwise direction, imposed as a volume force, drives the flow.

For a juxtaposition of the three concepts reviewed in Sects. 4–6, one representative form for each of them is chosen: the RBVMM based on quasi-static subgrid-scales as given in Eq. (68), the AVM^3 with small-scale subgrid-viscosity term and additional PSPG term as an

example for three-scale VMMs and the AVM^4 representing a structural subgrid-scale modeling strategy. Additionally, results obtained with a basic SUPG/ PSPG/Grad-div Stabilized Method (SPGSM) are included. Data for the AVM^3 and the AVM^4 shown in the following are extracted from [83] and [180] and additionally marked by the extensions "GGKW10" and "RG13", respectively. Moreover, data for the SPGSM and the RBVMM are likewise taken from [180] and identified accordingly.

Here, turbulent channel flow at $\mathrm{Re}_\tau = 395$ in a channel of dimensions $2\pi\delta_\mathrm{c}$ in streamwise, $2\delta_\mathrm{c}$ in wall-normal and $2/3\pi\delta_\mathrm{c}$ in spanwise direction is considered. As usual, δ_c is set to 1.0. DNS data for turbulent channel flow at this friction Reynolds number are provided in [155]. Reference data taken from that study are marked by "DNS MKM99" in the following. Trilinearly interpolated hexahedral elements are used for the velocity and pressure field. In wall-normal direction, the distribution of the elements is refined towards the walls, such that a better resolution in the vicinity of the walls is obtained. For temporal discretization, the generalized-α time-integration scheme, originally introduced in [46] for problems of solid mechanics and later extended to problems of fluid mechanics in [115], is applied. Here, generalized-α time integration is applied in the particular form presented for the incompressible Navier–Stokes equations in [85]. The parameters of the generalized-α scheme are chosen such that second-order accuracy in time is achieved. The time-step length, expressed in non-dimensional form as $\Delta t^+ = \Delta t u_\tau^2/\nu$ (see, e.g., [44]), is set to $\Delta t^+ = 0.7$. After the flow has reached a statistically stationary state, statistics are collected in homogeneous directions and in time during 5000 time steps. Statistical averages are denoted by $\langle\cdot\rangle$ and fluctuations by $(\cdot)'$. The root mean square, labeled by $\mathrm{rms}\,(\cdot)$, is defined as $\mathrm{rms}\,(\cdot) := \langle((\cdot)')^2\rangle^{\frac{1}{2}} = (\langle(\cdot)^2\rangle - \langle(\cdot)\rangle^2)^{\frac{1}{2}}$. All velocity results are normalized by the friction velocity u_τ, i.e., $u_i^+ = \langle u_i\rangle/u_\tau$ with $i = 1, 2, 3$, and plotted in wall units $x_2^+ = (u_\tau x_2)/\nu$, i.e., as a function of the normalized distance from the wall.

Figure 5 displays the mean streamwise velocity u_1^+ and the root-mean-square values of the velocity fluctuations in all three spatial directions, $\mathrm{rms}\,u_i^+$, obtained with the SPGSM, the RBVMM, the AVM^3 and the AVM^4. For the SPGSM, the RBVMM and the AVM^4, three discretizations of increasing resolution are considered. The coarser discretization with 32^3 elements exhibits a minimum non-dimensional element length of $h_{2,\mathrm{min}}^+ = (u_\tau h_{2,\mathrm{min}})/\nu = 1.43$ in wall-normal direction, the medium one with 64^3 elements a minimum element length of $h_{2,\mathrm{min}}^+ = 1.32$ and the finer one with 128^3 elements a minimum element length of $h_{2,\mathrm{min}}^+ = 1.00$. A coarser grid with 32^3 elements and a minimum non-dimensional element length of $h_{2,\mathrm{min}}^+ = 1.32$ and a medium grid with 64^3 elements and $h_{2,\mathrm{min}}^+ = 0.60$ are used for the AVM^3. While the coarser grid used for the AVM^3 is comparable to the respective one used for the other three methods considered here, the medium one exhibits a considerably different near-wall resolution. For all methods, convergence to DNS is observed for all quantities. Differences between the SPGSM and the RBVMM are only marginal for all results, indicating that the inclusion of the second cross- and the subgrid-scale Reynolds-stress term into the residual-based variational multiscale formulation does not necessarily improve the results. Using the coarser discretization, the profiles for u_1^+ obtained from the AVM^3 and the AVM^4 are substantially closer to the DNS profile than the profiles from the SPGSM and the RBVMM. However, a generally large deviation is observed for all methods, which has to be attributed to the applied second-order accurate method in combination with the coarse discretization used here. When using the medium discretization, the profile by the AVM^3 is considerably more accurate. The profile obtained with the AVM^4 is already for the medium discretization quite close to the DNS profile, and the improvement due to the finer discretization is only of small amount. In contrast, the SPGSM and the RBVMM provide profiles which substantially deviate from the DNS data using the medium discretization. Even with the finer discretization, there are still some deviations from the DNS results for the SPGSM and the RBVMM, while the AVM^4 results match them almost exactly. An overall similar picture is obtained for $\mathrm{rms}\,u_1^+$. For the root-mean-square velocities in wall-normal and spanwise direction, all methods somewhat deviate from the DNS data for the coarser discretization. Both the AVM^3 and the AVM^4 as well as the SPGSM and the RBVMM, respectively, yield good approximations for the medium discretization. The AVM^4, the SPGSM and the RBVMM capture $\mathrm{rms}\,u_2^+$ and $\mathrm{rms}\,u_3^+$ very accurately for the finer one.

Further insights into the behavior of the various VMMs is gained from an analysis of the subgrid-scale dissipation. For the basic approach, i.e., the SPGSM, the subgrid-scale dissipation consists of the contributions by the SUPG, PSPG and grad-div term and is denoted by $\varepsilon_{\mathrm{SPGSM}}$. The individual contributions due to the SUPG and the grad-div term read:

$$\varepsilon_{\mathrm{SUPG}} = \left(\tau_\mathrm{M}\mathbf{r}_\mathrm{M}^h \otimes \mathbf{u}^h\right):\nabla\mathbf{u}^h, \tag{135}$$

$$\varepsilon_{\mathrm{GD}} = \tau_\mathrm{C} r_\mathrm{C}^h \mathbf{I}:\nabla\mathbf{u}^h = \tau_\mathrm{C} r_\mathrm{C}^h(\nabla\cdot\mathbf{u}^h). \tag{136}$$

An analogous measure for the dissipation introduced by the PSPG term is defined as

$$\varepsilon_{\mathrm{PSPG}} = \nabla p_{\mathrm{kin}}^h \cdot \tau_\mathrm{M}\mathbf{r}_\mathrm{M}^h \tag{137}$$

and provides, in general, a contribution of negligible amount. For the subgrid-scale dissipation $\varepsilon_{\mathrm{AVM}^4}$ of the AVM^4, the dissipation owing to the cross- and

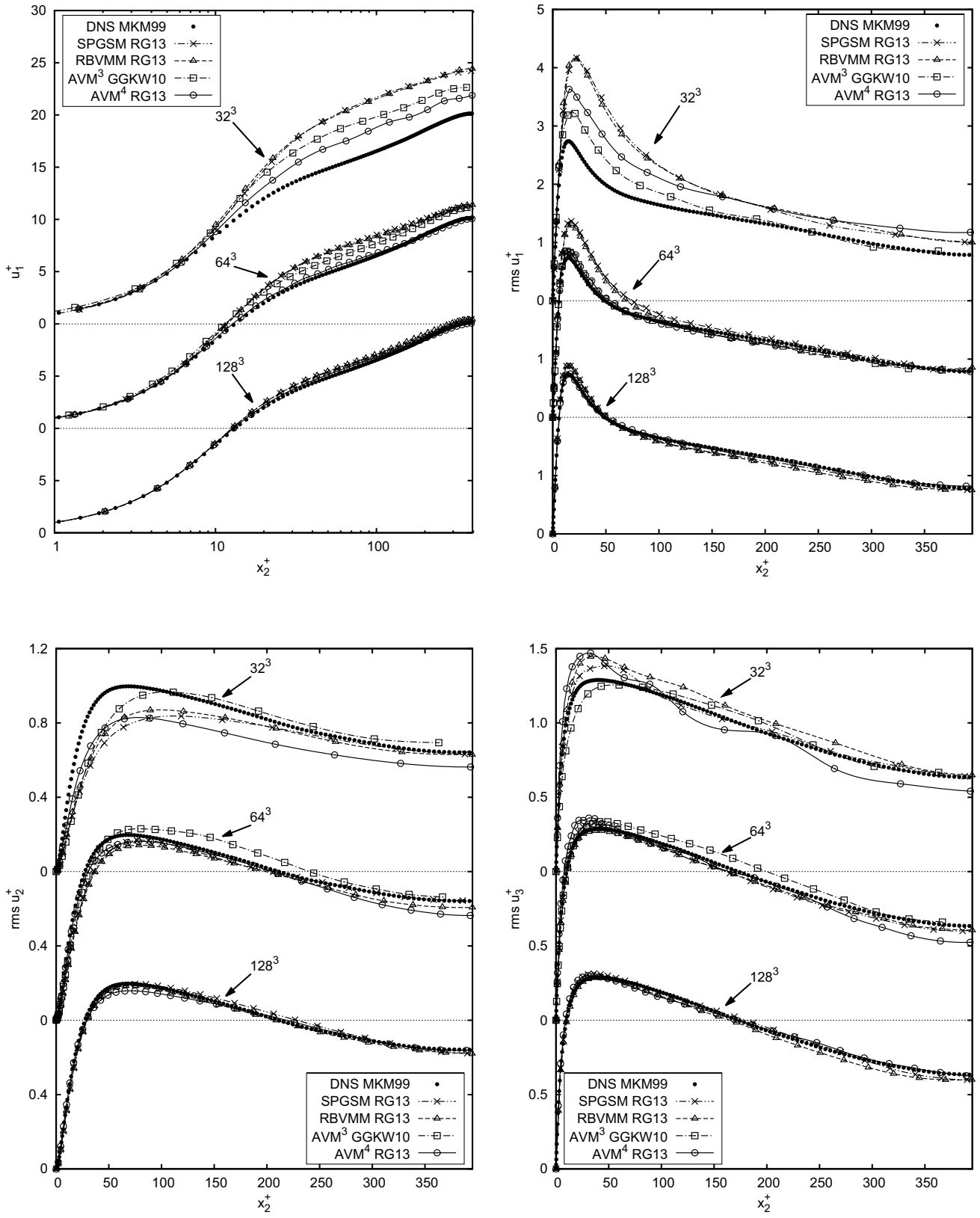

Fig. 5 Convergence study of mean streamwise velocity u_1^+ and root-mean-square velocities rms u_i^+ for turbulent channel flow at $\mathrm{Re}_\tau = 395$ using 32^3, 64^3 and 128^3 elements and various VMMs

subgrid-scale Reynolds-stress terms, $\varepsilon_{\text{MFS-C}}$ and $\varepsilon_{\text{MFS-R}}$, respectively, modeled by the multifractal subgrid-scale modeling approach have to be included in addition to the aforementioned terms. They are defined as

$$\varepsilon_{\text{MFS-C}} = -\left(B\delta\mathbf{u}^h \otimes \mathbf{u}^h + \mathbf{u}^h \otimes B\delta\mathbf{u}^h\right):\boldsymbol{\varepsilon}(\mathbf{u}^h), \tag{138}$$

$$\varepsilon_{\text{MFS-R}} = -\left(B\delta\mathbf{u}^h \otimes B\delta\mathbf{u}^h\right):\boldsymbol{\varepsilon}(\mathbf{u}^h). \tag{139}$$

The contributions by the second cross- and the subgrid-scale Reynolds-stress term of the RBVMM are given by

$$\varepsilon_{\text{RBVMM-C}} = \left(\mathbf{u}^h \otimes \tau_{\text{M}}\mathbf{r}_{\text{M}}^h\right):\nabla\mathbf{u}^h, \tag{140}$$

$$\varepsilon_{\text{RBVMM-R}} = -\left(\tau_{\text{M}}\mathbf{r}_{\text{M}}^h \otimes \tau_{\text{M}}\mathbf{r}_{\text{M}}^h\right):\nabla\mathbf{u}^h, \tag{141}$$

resulting, together with the respective contributions by the SUPG, PSPG and grad-div term, in the subgrid-scale dissipation $\varepsilon_{\text{RBVMM}}$ of the RBVMM. The contribution of the small-scale subgrid-viscosity term of the AVM^3 is obtained as

$$\varepsilon_{\text{SV}} = 2\nu'_{\text{sgs}}\boldsymbol{\varepsilon}(\mathbf{u}'^h):\boldsymbol{\varepsilon}(\mathbf{u}'^h). \tag{142}$$

The subgrid-scale dissipation of the AVM^3, including potential contributions from an SUPG, PSPG and grad-div term, is then denoted by $\varepsilon_{\text{AVM}^3}$. In non-dimensionalized form, the mean subgrid-scale dissipation is defined as $\varepsilon^+ = \langle\varepsilon\rangle\nu/u_\tau^4$.

To evaluate the dissipative properties of the various methods, the subgrid-scale dissipation estimated from filtered DNS data is considered as a reference. In [100], DNS of turbulent channel flow at $\text{Re}_\tau = 211$ was examined, and the energy transfer between resolved and unresolved scales that has to be captured in LES was estimated. To identify the subgrid-scale quantities, filtering corresponding to a resolution of $h_1^+ = 75$ and $h_3^+ = 39$ was applied in homogeneous directions. In the following, data taken from [100] are marked by "DNS HKUF94". For LES, the channel dimensions are $2\pi\delta_{\text{c}}$ in streamwise, $2\delta_{\text{c}}$ in wall-normal and $4/3\pi\delta_{\text{c}}$ in spanwise direction. The domain is discretized by 32^3 elements such that the minimal non-dimensional element length in wall-normal direction amounts to $h_{2,\text{min}}^+ = 1.63$ and the element lengths in the homogeneous directions to $h_1^+ = 41.43$ and $h_3^+ = 27.62$. Figure 6 displays the distribution of the subgrid-scale dissipation in wall-normal direction introduced by the SPGSM, the RBVMM and the AVM^4 as well as the data determined from filtered DNS. Respective data for the AVM^3 are not available. Excellent agreement is observed between the AVM^4 and filtered DNS. Both filtered DNS data as well as the results from the AVM^4 demonstrate a predominant subgrid-scale dissipation in the vicinity of the channel walls. In the core region, the subgrid-scale dissipation almost vanishes. The increased subgrid-scale dissipation particularly occurs within the buffer layer of the channel flow. The peak value is located at approximately $x_2^+ = 12$. Taking into account that the buffer layer constitutes the region of vigorous turbulence dynamics with the turbulent energy production rate reaching its maximum value at approximately $x_2^+ = 12$ (see, e.g., [207]), a very intense dissipation has to be expected in that region. A detailed investigation of the individual contributions to $\varepsilon_{\text{AVM}^4}$ reveals that the contribution $\varepsilon_{\text{MFS-C}}$ of the cross-stress terms is responsible for the pronounced peak in the vicinity of the wall and, thus, the excellent agreement between the subgrid-scale dissipation $\varepsilon_{\text{AVM}^4}$ and the filtered DNS data in the buffer layer. In contrast, the contribution $\varepsilon_{\text{MFS-R}}$ of the subgrid-scale Reynolds-stress term is only of very small amount. The distribution of the subgrid-scale dissipation of the AVM^3, merely analyzed in the context of turbulent variable-density flow at low Mach number in [87] and, therefore, not explicitly included here, exhibits a similar pronounced peak in the buffer-layer and approaches zero in the core of the channel. The SPGSM and the RBVMM provide considerably different curves in the buffer layer as well as towards the core of the channel. Although the respective distributions exhibit their maximum values close to the buffer layer, these maximum values are clearly smaller and less pronounced than the peak value of the AVM^4 and filtered DNS. Additionally, a higher subgrid-scale dissipation in the core of the channel is observed.

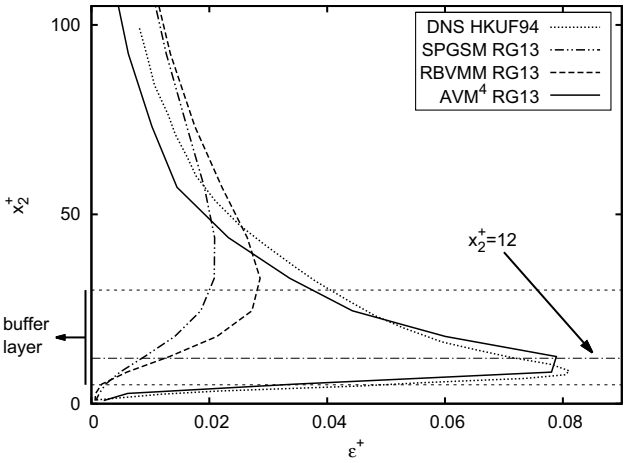

Fig. 6 Mean subgrid-scale dissipation ε^+ for turbulent channel flow at $\text{Re}_\tau = 211$ using 32^3 elements and various VMMs

8 Wall-Layer Modeling

For wall-bounded turbulent flow at already moderately high Reynolds number, the resolution of the flow regions in the vicinity of the wall causes a prohibitive raise in

computational effort required for LES of such a flow overall. This was already outlined in [42], which estimates were recently revisited in [45]. Thus, it is often aimed at modeling those layers close to the walls in lieu of adequately resolving them. In fact, already for early applications of LES such as the one in [55], it was either inevitable, particularly in the early years, or desired to separately treat the near-wall regions, that is, the wall layers, which usually require the majority of the degrees of freedom for an adequate resolution. In the last two decades, the interest in approaches to wall-layer modeling has notably increased. In the following, first, a brief overview on such approaches in the context of traditional LES will be provided. Afterwards, two ideas on wall-layer modeling which were recently proposed in combination with VMMs will be outlined. On the one hand, the weak enforcement of Dirichlet boundary conditions as well as a mixed/hybrid Dirichlet formulation will be addressed. On the other hand, a recent approach aiming at wall-layer modeling via function enrichment will be presented.

8.1 Wall-Layer Modeling for Traditional Large-Eddy Simulation

General overviews on wall-layer modeling for traditional LES were provided in [168], updating an earlier article of the same name by the author, among others, in [169], and recently in [133]. A review article focusing on hybrid LES/RANS methods can be found in [67]. One particularly well-known representative of such hybrid LES/RANS methods referred to as Detached-Eddy Simulation (DES) is reviewed in [197].

According to [168], the concepts for wall-layer modeling may be classified as follows:

- equilibrium-stress models,
- zonal approaches and
- hybrid LES/RANS methods.

This classification appears to be debatable, at least, since methods assigned to the second class, zonal approaches, in [168] are included in the class of hybrid LES/RANS methods in [67], for instance. However, in the following, it will be stuck to the classification above, and this ambiguity will be addressed in the context of a brief presentation of some representative concepts for each of the classes.

Equilibrium-stress models were the first wall-layer models and still remain the simplest ones. The basic idea relies on the assumption of the validity of the law of the wall, particularly including a logarithmic layer towards the outer end of the wall layer. This assumption was exploited, e.g., in the early works on LES in [55, 195] in various forms. Such simple models were more recently investigated in comparison to more complex zonal approaches in [217], for example.

The probably best-known form of a zonal approach is the Two-Layer Model (TLM) proposed in [5]. Another version of a TLM was later provided in [37], named Thin Boundary Layer Equations (TBLE). In a TLM approach as proposed in [5, 37], additional grids, which are embedded in the basic grid, are located in the respective wall-layer regions. In those studies, the grids were arranged between the first (finite) volume center away from the wall in wall-normal direction and the wall. On the embedded grids, simplified forms of the Navier–Stokes equations are solved, the TBLE,

$$\frac{\partial u_{\mathrm{t}_i}}{\partial t} + \frac{\partial u_{\mathrm{t}_i} u_j}{\partial x_j} + \frac{\partial P_{\mathrm{m}}}{\partial x_{\mathrm{t}_i}} = \frac{\partial}{\partial x_{\mathrm{n}}} \left[\left(\nu + \nu_{\mathrm{sgs}} \right) \frac{\partial u_{\mathrm{t}_i}}{\partial x_{\mathrm{n}}} \right], \tag{143}$$

for the velocity components in both directions x_{t_i}, with $i = 1, 2$, tangential to the wall, that is, orthogonal to the wall-normal direction x_{n}; see, e.g., [37]. The wall-normal velocity is then obtained via mass conservation:

$$u_{\mathrm{n}} = - \int_0^{x_{\mathrm{n}}} \left(\frac{\partial u_{\mathrm{t}_1}}{\partial x_{\mathrm{t}_1}} + \frac{\partial u_{\mathrm{t}_2}}{\partial x_{\mathrm{t}_2}} \right) \mathrm{d}x_{\mathrm{n}}. \tag{144}$$

Boundary conditions for this equation system are given by the no-slip condition imposed by the wall on one side and a matching condition for the velocity with respect to the values at the respective volume centers (or nodes) of the basic grid on the other side. Furthermore, the pressure in Eq. (143) is usually assumed to be independent of the wall-normal direction x_{n} and thus equal to the matching pressure P_{m}. Two simpler variants are obtained by either assuming the complete left-hand side of Eq. (143) to be zero or constituted by the pressure-gradient term only; see, e.g., [217]. In Eq. (143), a subgrid viscosity ν_{sgs} is included, which was determined by a simple mixing-length model in [5, 37, 217]. The TLM enables computational savings compared to a complete LES including the wall layer owing to the following reasons:

- Due to the fact that the pressure is assumed constant in wall-normal direction, merely (non-linear) scalar transport equations have to be solved on the embedded grids for two velocity components u_{t_1} and u_{t_2} in wall-parallel directions instead of a coupled velocity-pressure equation system. The third velocity component u_{n} is obtained via Eq. (144).
- The embedded grids need only be refined in wall-normal direction, and not in the wall-parallel directions.

As aforementioned, it is interesting to note that such zonal approaches are categorized in [67] as hybrid LES/RANS methods in the form of "unified LES/RANS methods with

hard interface layering RANS and LES". Among other things, this differing classification shows that the borderlines between the respective methods are rather soft, among other things. For an overview on the multitude of hybrid LES/RANS methods, the reader is referred to [67]. The probably most famous representative, DES, was originally proposed in [199]. Various improved versions, such as Delayed Detached-Eddy Simulation (DDES), introduced in [198], were subsequently published.

8.2 Weak Enforcement of Dirichlet Boundary Conditions and Mixed/Hybrid Dirichlet Formulation

A weak enforcement of no-slip boundary conditions was originally proposed for the Stokes equations in [134], which was based either on a Lagrange-multiplier approach or a penalty method. The issue of weakly enforcing Dirichlet boundary conditions for flow problems was revisited in [10], using Nitsche's method [160]. The reader is referred also to [203] for a comparative review of Nitsche's method and a Lagrange-multiplier approach for imposing boundary conditions in general. In a subsequent publication, the authors of [10], among others, proposed an alternative version to their original one, which determines the model parameter of Nitsche's method based on the law of the wall due to [200], e.g., in [11].

In [69], a new method for weakly imposing Dirichlet boundary conditions based on an embedded Dirichlet formulation and utilizing an additional discontinuous stress field was proposed. It is based on the embedded Dirichlet method introduced in [74], including a wall-stress model to impose a tangential traction boundary condition. Moreover, it guarantees the correct impermeability of the wall by a consistent modification of the approach developed in [10, 11]. The impermeability of the wall is ensured despite the weak enforcement of the Dirichlet boundary condition in both tangential and normal directions. This allows for a straightforward handling of complex, curved geometries, since local coordinate systems are not required to enforce a strong Dirichlet boundary condition in the wall-normal direction.

The incompressible Navier–Stokes equations (1) and (2) may be extended to a mixed/hybrid formulation by adding the following equation:

$$\frac{1}{2\nu}\left(\boldsymbol{\sigma} + p_{\text{kin}}\mathbf{I}\right) - \boldsymbol{\varepsilon}(\mathbf{u}) = \mathbf{0} \quad \text{in } \Omega, \tag{145}$$

where the stress tensor $\boldsymbol{\sigma}$ is introduced as an additional independent variable. Moreover, the Dirichlet boundary condition (4) is reformulated in residual form as

$$\mathbf{u} - \mathbf{u}_{\text{D}} = \mathbf{0} \quad \text{on } \Gamma_{\text{D},\mathbf{u}}. \tag{146}$$

Equations (145) and (146) are introduced into an enhanced finite element formulation of the mixed/hybrid approach: find $(\mathbf{u}^h, p^h_{\text{kin}}) \in \mathcal{S}^h_{\mathbf{u}} \times \mathcal{S}^h_p$ and $\boldsymbol{\sigma}^h \in \mathcal{S}^h_{\boldsymbol{\sigma}}$ such that

$$\mathcal{B}_{\text{NS- MH}}(\mathbf{v}^h, q^h, \mathbf{r}^h; \mathbf{u}^h, p^h_{\text{kin}}, \boldsymbol{\sigma}^h) = \ell_{\text{NS}}(\mathbf{v}^h), \tag{147}$$

for all $(\mathbf{v}^h, q^h) \in \mathcal{V}^h_{\mathbf{u}} \times \mathcal{V}^h_p$ and $\mathbf{r}^h \in \mathcal{V}^h_{\boldsymbol{\sigma}}$, where appropriate discrete solution and weighting function spaces $\mathcal{S}^h_{\boldsymbol{\sigma}}$ and $\mathcal{V}^h_{\boldsymbol{\sigma}}$ for $\boldsymbol{\sigma}^h$ and the stress weighting function $\mathbf{r}^h$ are assumed. The form on the left-hand side of Eq. (147) is defined by

$$\begin{aligned}
&\mathcal{B}_{\text{NS-MH}}(\mathbf{v}^h, q^h, \mathbf{r}^h; \mathbf{u}^h, p^h_{\text{kin}}, \boldsymbol{\sigma}^h) := \\
&\mathcal{B}_{\text{NS}}(\mathbf{v}^h, q^h; \mathbf{u}^h, p^h_{\text{kin}}) \\
&+ \left(\mathbf{r}^h, \tfrac{1}{2\nu}\boldsymbol{\sigma}^h\right)_\Omega + \left(\mathbf{r}^h, \tfrac{p^h_{\text{kin}}}{2\nu}\mathbf{I}\right)_\Omega \\
&- \left(\mathbf{r}^h, \boldsymbol{\varepsilon}(\mathbf{u}^h)\right)_\Omega - \left(\mathbf{r}^h, \tau_{\text{B,t}}\left(\mathbf{u}_{\text{D}} - \mathbf{u}^h\right) \otimes \mathbf{n}\right)_{\Gamma_{\text{D},\mathbf{u}}} \\
&- \left(\mathbf{r}^h, \left(\tau_{\text{B,n}} - \tau_{\text{B,t}}\right)\left[\left(\mathbf{u}_{\text{D}} - \mathbf{u}^h\right) \cdot \mathbf{n}\right]\mathbf{n} \otimes \mathbf{n}\right)_{\Gamma_{\text{D},\mathbf{u}}},
\end{aligned} \tag{148}$$

with the outward normal vector $\mathbf{n}$ on the boundary.

The additional stress-based terms in the last three lines of Eq. (148) are only introduced for elements next to a boundary or the boundaries themselves, respectively. According to the embedded Dirichlet method in [74], these discontinuous discrete stresses are locally eliminated within each element. The introduction of two parameters, $\tau_{\text{B,n}}$ and $\tau_{\text{B,t}}$, allows for separately treating the wall-normal and the tangential direction. For $\tau_{\text{B,n}} = \tau_{\text{B,t}} = 1.0$, the original formulation in [74] is recovered.

Such a separate treatment of wall-normal and tangential direction is particularly beneficial for wall-bounded turbulent flow. On the one hand, in tangential direction, a weak enforcement of the velocities subject to the law of the wall is enabled. For this purpose, as in [11], the law of the wall according to [200] and given by

$$\begin{aligned}
x_2^+ = u^+ + \mathrm{e}^{-\kappa_{\text{lw}} B_{\text{lw}}}\Big(&\mathrm{e}^{\kappa_{\text{lw}} u^+} - 1 - \kappa_{\text{lw}} u^+ \\
&- \frac{\left(\kappa_{\text{lw}} u^+\right)^2}{2!} - \frac{\left(\kappa_{\text{lw}} u^+\right)^3}{3!} - \frac{\left(\kappa_{\text{lw}} u^+\right)^4}{4!}\Big),
\end{aligned} \tag{149}$$

is used, where κ_{lw} denotes the von Kármán constant and B_{lw} the log-law constant. Moreover, the distance to the wall as well as the velocity are expressed in wall units; see also Sect. 7.2 for definitions.

On the other hand, a strict enforcement of the non-penetration condition in normal direction is ensured. The improved control of the boundary value in wall-normal direction avoids undesired transport of momentum across the (weakly enforced) boundary. It is also consistent with properties of turbulent channel flows as shown, e.g., in [173]. In fact, it is known that, in the vicinity of the wall (i.e., within the viscous sublayer), the root-mean-square values of the velocity fluctuations in tangential direction scale as $O(x_2^+)$, while the wall-normal fluctuations scale as $O((x_2^+)^2)$, and are much smaller close to the wall, as a result.

The mixed/hybrid Dirichlet formulation together with an RBVMM was investigated for turbulent channel flow at

moderate friction Reynolds number of $\mathrm{Re}_\tau = 395$ in [69]. Grids with and without adequate resolution of the boundary layer were considered. Compared to strongly-imposed boundary conditions, the mixed/hybrid Dirichlet formulation showed an error reduction of up to 50% for mean velocity results in the core of the channel on coarse discretizations.

8.3 Wall-Layer Modeling via Function Enrichment

This modeling approach based on function enrichment was recently proposed in [130]. The idea underlying this approach follows the paradigm of DES that not all turbulent scales need to be resolved at the wall. Rather, their ensemble-averaged solution is merely computed. Therefore, specific solution functions are incorporated that are able to recover the mean velocity profile. As a result, if the solution function space is capable of resolving the mean gradient, the resolution in wall-normal direction may be very coarse. A (local) enhancement of the function space by problem-specific shape functions is enabled, e.g., by the eXtended Finite Element Method (XFEM). The XFEM was originally proposed to recover discontinuities in the element interior for crack-propagation problems in solid mechanics in [13, 152] and later broadened to various other applications, as reviewed, e.g., in [65].

Following the concept of the XFEM, the discrete velocity $\mathbf{u}^h$ is given by

$$\mathbf{u}^h(\mathbf{x},t) = \mathbf{u}^{h,\mathrm{std}}(\mathbf{x},t) + \mathbf{u}^{h,\mathrm{enr}}(\mathbf{x},t). \tag{150}$$

Therein, the standard finite element expansion reads

$$\mathbf{u}^{h,\mathrm{std}}(\mathbf{x},t) = \sum_{A\in\mathcal{E}} N_A(\mathbf{x})\mathbf{u}_A^{\mathrm{std}}(t), \tag{151}$$

where N_A denote the standard polynomial shape functions and $\mathbf{u}_A^{\mathrm{std}}$ the standard velocity degrees of freedom at node A. The enrichment part, using additional degrees of freedom $\mathbf{u}_A^{\mathrm{enr}}$, is given by

$$\mathbf{u}^{h,\mathrm{enr}}(\mathbf{x},t) = \sum_{A\in\mathcal{E}_{\mathrm{enr}}} N_A(\mathbf{x})\big(\Psi(\mathbf{x},t) - \Psi(\mathbf{x}_A,t)\big)\mathbf{u}_A^{\mathrm{enr}}(t). \tag{152}$$

Moreover, $\mathcal{E}$ denotes the set of all nodes and $\mathcal{E}_{\mathrm{enr}}$ a subset of enriched nodes in the near-wall region.

An appropriate choice for the enrichment function $\Psi(\mathbf{x},t)$ is the crucial feature of the overall approach. This function enables the inclusion of information a priori known about boundary layers into the function space without prescribing the solution itself. In [130], the enrichment function was determined based on the law of the wall (149) by setting $u^+ = \Psi/\kappa_{\mathrm{lw}}$:

$$x_2^+ = \frac{\Psi}{\kappa_{\mathrm{lw}}} + \mathrm{e}^{-\kappa_{\mathrm{lw}}B_{\mathrm{lw}}}\Big(\mathrm{e}^{\Psi} - 1 - \Psi - \frac{\Psi^2}{2!} - \frac{\Psi^3}{3!} - \frac{\Psi^4}{4!}\Big). \tag{153}$$

It is emphasized that the law of the wall is not prescribed a priori as the targeted velocity profile; the numerical method is rather enabled to utilize a law of the wall besides the standard polynomial shape functions. The method is then required to find the best possible solution in a variationally consistent manner from the complete function space consisting of standard polynomial shape functions and the functions according to the law of the wall. Figure 7 depicts the decomposition of the mean velocity in the inner layer into a standard polynomial component (i.e., a linear one for the present illustration) as well as an enrichment component.

Together with the unresolved scales in LES, the overall approach may also be interpreted as a particular form of a three-scale decomposition of the velocity field. The scales $\mathbf{u}^{h,\mathrm{std}}$ associated with the standard function space resolve larger turbulent scales, which are at least of the size of the characteristic element length, in the sense of an LES. The scales $\mathbf{u}^{h,\mathrm{enr}}$ associated with the enhancement of the function space are supposed to cover flow scales in a statistical sense without resolving the turbulent scales in the near-wall region explicitly. For the modeling of the unresolved scales in LES, the mutifractal subgrid-scale model as described in Sect. 6 was used in [130].

Wall-layer modeling via function enrichment was tested for turbulent channel flow at moderate and moderately high friction Reynolds numbers between $\mathrm{Re}_\tau = 590$ and 5 000, flow past periodic hills and a backward-facing step in [130]. Excellent agreement with experimental and

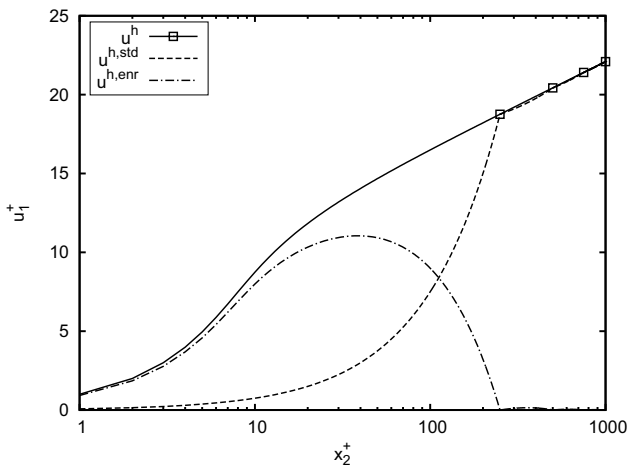

Fig. 7 Decomposition of mean velocity in inner layer into standard and enrichment components where symbols indicate locations of nodes

DNS data was stated for turbulent-channel-flow simulations with the first node located at up to a distance of $x_2^+ = 500$ away from the wall and, in particular, for flows exhibiting adverse pressure gradients and separation.

9 Passive and Active Scalar Transport

Extensions of LES methods to turbulent mixing of scalar fields are also of particular relevance. Passive scalar fields, occurring, for instance, in electrochemical processes, have no influence on the flow field. In contrast, active scalar fields such as the temperature in weakly compressible flows, for example, encountered in turbulent combustion, may give rise to substantial density variations. For these applications, new length scales in the scalar field as well as additional physics have to be incorporated into the approach to LES. An introduction into LES of scalar transport in turbulent flow, including a survey of selected subgrid-scale models further developed for that purpose, may be found, e.g., in [188]. In the following, extensions of the VMMs introduced in Sect. 4–6 to passive and active scalar transport will be presented, including a brief introduction into the dynamics of a scalar field evolving in a turbulent flow.

9.1 Problem Statement: The Convection–Diffusion Equation

Scalar transport in the domain Ω is described by the convection–diffusion equation, given in convective form here, as:

$$\frac{\partial \phi}{\partial t} + \mathbf{u} \cdot \nabla \phi - D \Delta \phi = f_\phi \quad \text{in } \Omega, \tag{154}$$

where $\phi(\mathbf{x}, t)$ denotes a scalar quantity, for instance, a concentration, and D, which is assumed constant, the kinematic diffusivity. The velocity field $\mathbf{u}(\mathbf{x}, t)$ is obtained from the incompressible Navier–Stokes equations. For the sake of completeness, a potential source term f_ϕ is additionally included. Dirichlet boundary conditions are provided on the part $\Gamma_{\mathrm{D},\phi}$ of the boundary $\partial\Omega$, while Neumann boundary conditions are imposed on $\Gamma_{\mathrm{N},\phi}$, assuming $\Gamma_{\mathrm{D},\phi} \cap \Gamma_{\mathrm{N},\phi} = \emptyset$ and $\Gamma_{\mathrm{D},\phi} \cup \Gamma_{\mathrm{N},\phi} = \partial\Omega$:

$$\phi = \phi_\mathrm{D} \quad \text{on } \Gamma_{\mathrm{D},\phi}, \tag{155}$$

$$-\phi(\mathbf{u} \cdot \mathbf{n}) + D \nabla \phi \cdot \mathbf{n} = h_\phi \quad \text{on } \Gamma^{\mathrm{in}}_{\mathrm{N},\phi}, \tag{156}$$

$$D \nabla \phi \cdot \mathbf{n} = h_\phi \quad \text{on } \Gamma^{\mathrm{out}}_{\mathrm{N},\phi}. \tag{157}$$

Analogously to the Neumann boundary condition for the momentum equation (see Sect. 2.1), the diffusive flux is prescribed on the outflow part $\Gamma^{\mathrm{out}}_{\mathrm{N},\phi}(t) = \{\mathbf{x} \in \Gamma_{\mathrm{N},\phi} | \mathbf{u}(\mathbf{x}, t) \cdot \mathbf{n}(\mathbf{x}) \geqslant 0\}$ and the total flux on a potential inflow part $\Gamma^{\mathrm{in}}_{\mathrm{N},\phi}(t) = \{\mathbf{x} \in \Gamma_{\mathrm{N},\phi} | \mathbf{u}(\mathbf{x}, t) \cdot \mathbf{n}(\mathbf{x}) < 0\}$, with $\Gamma^{\mathrm{out}}_{\mathrm{N},\phi} \cap \Gamma^{\mathrm{in}}_{\mathrm{N},\phi} = \emptyset$ and $\Gamma^{\mathrm{out}}_{\mathrm{N},\phi} \cup \Gamma^{\mathrm{in}}_{\mathrm{N},\phi} = \Gamma_{\mathrm{N},\phi}$. The initial condition is given by

$$\phi = \phi_0 \quad \text{in } \Omega. \tag{158}$$

9.2 Scalar Subgrid Scales in Large-Eddy Simulation

The passive scalar field undergoes different transport regimes depending on Reynolds and Schmidt number (see, e.g., [207]). The ratio of kinematic viscosity ν and diffusivity D defines the Schmidt number as $\mathrm{Sc} = \nu/D$. The aforementioned transport regimes are caused by the occurrence of different length scales in the flow and scalar field and need to be considered in the subgrid-scale modeling procedure.

For small Schmidt numbers (i.e., $\mathrm{Sc} \leq 1$), the scalar-variance spectrum possesses an inertial-convective range similar to the inertial range of the kinetic-energy spectrum. In this range, the scalar-variance spectrum scales depending on the wave number k as $E_\phi \sim k^{-\frac{5}{3}}$. Analogously to the Kolmogorov scale $\eta_\mathrm{K} = (\nu^3/\varepsilon)^{\frac{1}{4}}$ for the velocity field, the Obukhov–Corrsin scale $\eta_\mathrm{OC} = (D^3/\varepsilon)^{\frac{1}{4}}$ defines the diffusive scale associated with the smallest turbulent structures in the scalar field. The ratio of these scales depends on the Schmidt number as $\eta_\mathrm{OC}/\eta_\mathrm{K} = \mathrm{Sc}^{-\frac{3}{4}}$. Flows at large Schmidt numbers (i.e., $\mathrm{Sc} \gg 1$) exhibit a more complex situation, as two distinct inertial ranges exist. For scales within the inertial range of the underlying fluid field, that is, scales much larger than the Kolmogorov scale, an inertial-convective range similar to $\mathrm{Sc} \leq 1$ emanates. At smaller scales, velocity fluctuations are already affected by dissipation, while scalar diffusion is not yet effective. Therefore, a second inertial range, referred to as viscous-convective range, emerges in the scalar field. Within this range, the scalar-variance spectrum scales as $E_\phi \sim k^{-1}$. Furthermore, the diffusive scale is defined by the Batchelor scale as $\eta_\mathrm{B} = (\nu D^2/\varepsilon)^{\frac{1}{4}}$. The ratio of the Batchelor scale to the Kolmogorov scale is obtained as $\eta_\mathrm{B}/\eta_\mathrm{K} = \mathrm{Sc}^{-\frac{1}{2}}$.

Figure 8 illustrates the various modeling situations encountered in LES of passive scalar transport by means of the scalar-variance spectrum $E_\phi(k)$ and the kinetic-energy spectrum $E(k)$. The particular case $\mathrm{Sc} \approx 1$ is shown separately. The diffusive wave number is denoted by k_D and the viscous one by k_ν. The wave number corresponding to the discretization is k_h. While in LES of passive scalar transport at low Schmidt numbers both velocity and scalar field

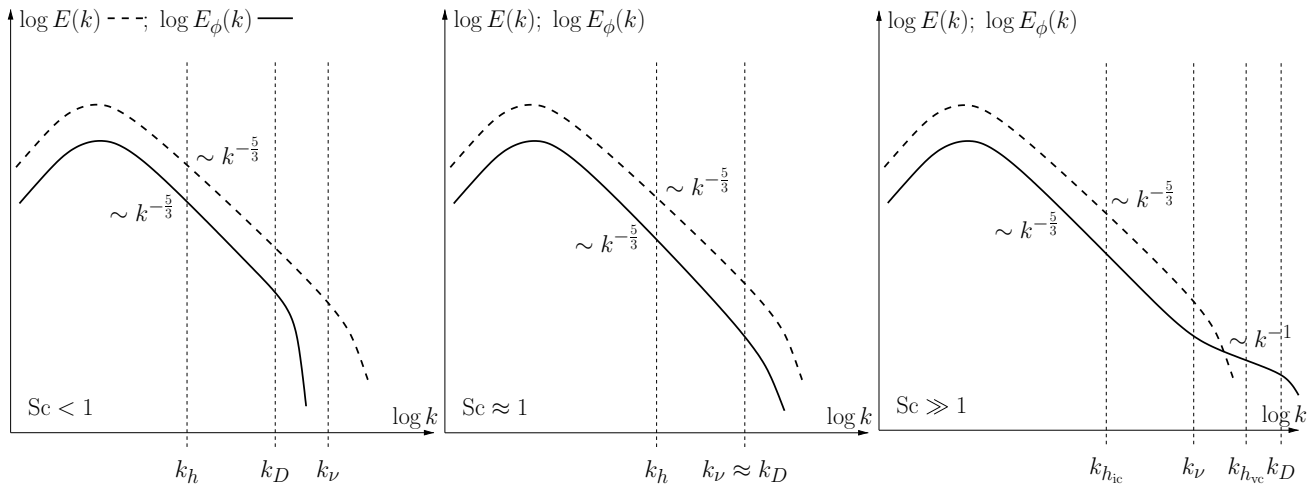

Fig. 8 Modeling situations in LES of passive scalar transport

are usually underresolved, two different situations need to be distinguished in the high-Schmidt-number case. If k_h is located within the inertial-convective range (marked by the additional index "ic" in the right diagram of Fig. 8), the same modeling situation as for $\mathrm{Sc} \leq 1$ is encountered. The situation is different if k_h lies within the viscous-convective range (marked by the additional index "vc"). In this case, subgrid-scale modeling is merely required in the scalar field as the velocity scales are resolved. Hence, different approaches are needed depending on the Schmidt-number regime, the resolution of velocity and scalar field as well as the physical mechanisms driving the subgrid-scale scalar field.

9.3 Variational Multiscale Formulation of the Convection–Diffusion Equation

For the variational formulation of the convection–diffusion equation (154), an appropriate solution function space $\mathcal{S}_\phi$ for ϕ as well as a weighting function space $\mathcal{V}_\phi$ for the scalar weighting function w are assumed. The convection–diffusion equation is then multiplied by $w \in \mathcal{V}_\phi$ and integrated over the domain Ω. The diffusive term is further integrated by parts, with boundary conditions (155) as well as (156) and (157) applied to the resulting boundary integral. The variational formulation of the convection–diffusion equation is thus given as follows: find $\phi \in \mathcal{S}_\phi$ such that

$$\mathcal{B}_{\mathrm{CD}}(w;\phi) = \ell_{\mathrm{CD}}(w) \tag{159}$$

for all $w \in \mathcal{V}_\phi$. The form on the left-hand side is given as

$$\begin{aligned}\mathcal{B}_{\mathrm{CD}}(w;\phi) := &\left(w, \frac{\partial \phi}{\partial t}\right)_\Omega + (w, \mathbf{u}\cdot\nabla\phi)_\Omega + (\nabla w, D\nabla\phi)_\Omega \\ &- (w, \phi(\mathbf{u}\cdot\mathbf{n}))_{\Gamma^{\mathrm{in}}_{\mathrm{N},\phi}},\end{aligned} \tag{160}$$

where the last term arises due to the inflow part of the Neumann boundary condition. Again, this term is not subject to the following scale separation and omitted in the subsequent derivations. The linear form on the right-hand side, including the Neumann boundary condition, is given as

$$\ell_{\mathrm{CD}}(w) := \left(w, f_\phi\right)_\Omega + \left(w, h_\phi\right)_{\Gamma_{\mathrm{N},\phi}}. \tag{161}$$

For a basic variational multiscale formulation of the convection-diffusion equation following a two-scale decomposition, analogous to Sect. 3.3, the scalar quantity is decomposed into a resolved and subgrid-scale component as

$$\phi = \phi^h + \hat{\phi}, \tag{162}$$

implying a direct sum decomposition of the underlying function space in the form $\mathcal{S}_\phi = \mathcal{S}^h_\phi \oplus \hat{\mathcal{S}}_\phi$. Based on the variational multiscale concept, a variational projection for separating resolved and unresolved scales is assumed. Therefore, a direct sum decomposition of weighting function space $\mathcal{V}_\phi = \mathcal{V}^h_\phi \oplus \hat{\mathcal{V}}_\phi$ is introduced as well. Accordingly, the weighting function is decomposed as

$$w = w^h + \hat{w}. \tag{163}$$

Inserting decomposition (162) into the variational form (159), weighting separately by the resolved and the subgrid-scale part of the decomposed weighting function (163) and omitting the equation projected onto the space of unresolved scales, the variational multiscale

formulation of the convection-diffusion equation is obtained as follows:

$$\begin{aligned}&\mathcal{B}_{\mathrm{CD}}(w^h;\phi^h)+\mathcal{C}_{\mathrm{CD}}(w^h;\mathbf{u}^h,\hat{\mathbf{u}},\phi^h,\hat{\phi})\\&+\mathcal{R}_{\mathrm{CD}}(w^h;\hat{\mathbf{u}},\hat{\phi})+\mathcal{B}^{1,\mathrm{lin}}_{\mathrm{CD}}(w^h;\hat{\phi})=\ell_{\mathrm{CD}}(w^h)\end{aligned}\tag{164}$$

for all $w^h\in\mathcal{V}^h_\phi$, where

$$\mathcal{C}_{\mathrm{CD}}(w^h;\mathbf{u}^h,\hat{\mathbf{u}},\phi^h,\hat{\phi}):=\left(w^h,\mathbf{u}^h\cdot\nabla\hat{\phi}+\hat{\mathbf{u}}\cdot\nabla\phi^h\right)_\Omega\tag{165}$$

and

$$\mathcal{R}_{\mathrm{CD}}(w^h;\hat{\mathbf{u}},\hat{\phi}):=\left(w^h,\hat{\mathbf{u}}\cdot\nabla\hat{\phi}\right)_\Omega\tag{166}$$

are the projections of the convective subgrid-scale flux vectors onto the space of resolved scales. Since these terms are analogous to the cross- and subgrid-scale Reynolds-stress terms of the momentum equation (see Sect. 3.3), they are likewise referred to as cross-stress terms and subgrid-scale Reynolds-stress term, respectively. The form

$$\mathcal{B}^{1,\mathrm{lin}}_{\mathrm{CD}}(w^h;\hat{\phi}):=\left(w^h,\frac{\partial\hat{\phi}}{\partial t}\right)_\Omega+\left(\nabla w^h,D\nabla\hat{\phi}\right)_\Omega\tag{167}$$

contains the remaining linear terms in the unresolved-scale quantity. To solve the variational multiscale formulation for $\phi^h\in\mathcal{S}^h_\phi$, the cross- and subgrid-scale Reynolds-stress terms as well as $\mathcal{B}^{1,\mathrm{lin}}_{\mathrm{CD}}(w^h;\hat{\phi})$ have to be modeled. For passive scalar transport, which constitutes a one-way-coupled problem, subgrid-scale modeling in the momentum equation remains unaffected.

A three-scale decomposition, analogous to Sect. 3.4, assumes the scalar quantity to be decomposed into a large resolved-, small resolved- and subgrid-scale component as

$$\phi=\underbrace{\overline{\phi}^h+\phi'^h}_{\phi^h}+\hat{\phi},\tag{168}$$

implying a direct sum decomposition of the underlying function space in the form $\mathcal{S}_\phi=\overline{\mathcal{S}}^h_\phi\oplus\mathcal{S}'^h_\phi\oplus\hat{\mathcal{S}}_\phi$. This goes along with a direct sum decomposition of the weighting function space as $\mathcal{V}_\phi=\overline{\mathcal{V}}^h_\phi\oplus\mathcal{V}'^h_\phi\oplus\hat{\mathcal{V}}_\phi$, resulting in the following split-up of the weighting function:

$$w=\underbrace{\overline{w}^h+w'^h}_{w^h}+\hat{w}.\tag{169}$$

The three-scale decomposition allows for replacing Eq. (164) by two equations, an equation projected onto the space of larger resolved scales,

$$\begin{aligned}&\mathcal{B}_{\mathrm{CD}}(\overline{w}^h;\phi^h)+\mathcal{C}_{\mathrm{CD}}(\overline{w}^h;\mathbf{u}^h,\hat{\mathbf{u}},\phi^h,\hat{\phi})\\&+\mathcal{R}_{\mathrm{CD}}(\overline{w}^h;\hat{\mathbf{u}},\hat{\phi})+\mathcal{B}^{1,\mathrm{lin}}_{\mathrm{CD}}(\overline{w}^h;\hat{\phi})=\ell_{\mathrm{CD}}(\overline{w}^h)\end{aligned}\tag{170}$$

for all $\overline{w}^h\in\overline{\mathcal{V}}^h_\phi$, which is solved for $\overline{\phi}^h\in\overline{\mathcal{S}}^h_\phi$, and an equation projected onto the space of smaller resolved scales,

$$\begin{aligned}&\mathcal{B}_{\mathrm{CD}}(w'^h;\phi^h)+\mathcal{C}_{\mathrm{CD}}(w'^h;\mathbf{u}^h,\hat{\mathbf{u}},\phi^h,\hat{\phi})\\&+\mathcal{R}_{\mathrm{CD}}(w'^h;\hat{\mathbf{u}},\hat{\phi})+\mathcal{B}^{1,\mathrm{lin}}_{\mathrm{CD}}(w'^h;\hat{\phi})=\ell_{\mathrm{CD}}(w'^h)\end{aligned}\tag{171}$$

for all $w'^h\in\mathcal{V}'^h_\phi$, which governs $\phi'^h\in\mathcal{S}'^h_\phi$. In (170) and (171), the resolved part of the scalar quantity and the velocity may be further separated into a large- and a small-scale part, as given in (168) and (38).

9.4 Active Scalar Transport: Variable-Density Flow at Low Mach Number

VMMs for LES of turbulent flow including scalar transport in general are barely addressed in literature so far. Regarding active scalar transport in particular, mainly turbulent variable-density flow at low Mach number is considered. Therefore, with respect to the subsequent discussion of VMMs for LES of passive and active scalar transport, a brief summary of the corresponding governing equation system is presented here. Comprehensive derivations of the system of equations may be found, e.g., in [61, 156, 183] and with emphasis on combustion, e.g., in [145].

Variable-density flow at low Mach number in the domain Ω is described by the following form of the conservation equations of mass, momentum and energy, the latter expressed in terms of temperature:

$$\frac{\partial\rho}{\partial t}+\nabla\cdot(\rho\mathbf{u})=0\quad\text{in }\Omega,\tag{172}$$

$$\begin{aligned}&\rho\frac{\partial\mathbf{u}}{\partial t}+\rho\mathbf{u}\cdot\nabla\mathbf{u}+\nabla p_{\mathrm{hyd}}\\&-\nabla\cdot\left(2\mu\left(\boldsymbol{\varepsilon}(\mathbf{u})-\frac{1}{3}(\nabla\cdot\mathbf{u})\mathbf{I}\right)\right)=\rho\mathbf{f}\quad\text{in }\Omega,\end{aligned}\tag{173}$$

$$\rho\frac{\partial T}{\partial t}+\rho\mathbf{u}\cdot\nabla T-\nabla\cdot\left(\frac{\lambda}{c_p}\nabla T\right)=\frac{1}{c_p}\frac{\mathrm{d}p_{\mathrm{the}}}{\mathrm{d}t}\quad\text{in }\Omega.\tag{174}$$

Momentum and energy equation are again given in convective form. Furthermore, $\rho(\mathbf{x},t)$ denotes the density, $\mathbf{u}(\mathbf{x},t)$ the velocity, $p_{\mathrm{hyd}}(\mathbf{x},t)$ the hydrodynamic pressure, $\mu(\mathbf{x},t)$ the dynamic viscosity, $\mathbf{f}$ a potential volume force vector, $T(\mathbf{x},t)$ the temperature, $\lambda(\mathbf{x},t)$ the thermal conductivity and c_p the specific heat capacity at constant pressure, which is assumed constant. The thermodynamic pressure $p_{\mathrm{the}}(t)$, which is constant in space, is either assumed constant in time as well or determined from global conservation principles over the domain Ω depending on the boundary conditions.

Continuity and momentum equation are coupled to the energy equation via the equation of state for an ideal gas,

$$\rho(T) = \frac{p_{\text{the}}}{RT}, \tag{175}$$

determining the density ρ. The gas constant is denoted by R. Moreover, the dynamic viscosity $\mu(T)$ is assumed to depend on T according, for instance, to Sutherland's law. The thermal conductivity $\lambda(T)$, likewise depending on T, can be expressed as $\lambda = (c_p\mu)/\text{Pr}$, where Pr denotes the Prandtl number. The Prandtl number, which is assumed constant, estimates the ratio of kinematic viscosity $\nu = \mu/\rho$ and (kinematic) thermal diffusivity $D_T = \lambda/(\rho c_p)$ and is the analogue to the Schmidt number in the context of heat transfer.

The derivation of the variational multiscale formulation of the low-Mach-number equation system, (172) to (174), parallels the ones for the incompressible Navier–Stokes equations and the convection–diffusion equation, thoroughly presented in Sects. 3.2 and 9.3. Therefore, it is refrained from explicitly presenting the variational multiscale formulation. A a step-by-step derivation may be found, e.g., in [178].

9.5 Residual-Based Variational Multiscale Methods

Stabilized methods for convection-dominated flow problems, as discussed in Sect. 4.1, are commonly derived starting from the convection–diffusion equation; see, e.g., [26, 29, 161]. Thus, the SUPG method, already mentioned in that section, also plays an essential role in FEMs for scalar-transport problems. The considerations and approaches towards RBVMMs for LES, that is, the incorporation of all cross- and subgrid-scale Reynolds-stress terms via residual-based subgrid-scale approximations and the concepts of time-dependent or quasi-static as well as potential orthogonal subgrid-scales, may also be transferred to the variational multiscale formulation of the convection–diffusion equation.

Using an extension to passive-scalar-transport problems of the method suggested in [9] for incompressible flow, multi-ion transport at high Schmidt numbers in turbulent Taylor-Couette flow was examined in [8]. Thermal/velocity boundary-layer simulations, where temperature was assumed as a passive scalar, were considered with an RBVMM in [3]. Thermally coupled flow problems described via the Bousinessq approximation as well as turbulent flow over a surface-mounted obstacle with passive scalar transport were investigated in [48], comparing quasi-static and time-dependent orthogonal residual-based subgrid-scale approximations. Applications of an RBVMM based on the one presented in [9] to LES of turbulent variable-density flow at low Mach number can be found in [88]. Therein, laminar and turbulent flow problems, among others, recirculating flow in a lid-driven cavity with heating and cooling of the walls, were examined. Another RBVMM with time-dependent and othogonal subgrid scales was proposed in [4]. Therein, residual-based subgrid scales were included in all non-linear terms arising in the VMM as well as in the evaluation of the physical parameters. The method was applied to turbulent channel flow with a heated and cooled wall as well as to natural convection in a cavity.

The evolution of the subgrid-scale scalar quantity is governed by the equation projected onto the space of unresolved scales, similar to $\hat{\mathbf{u}}$. An analytical approximation for $\hat{\phi}$ is obtained from this equation by considerations analogous to the ones outlined in Sects. 4.2 and 4.3. In the following, merely the residual-based variational multiscale formulation corresponding to the one presented in elaborate form for the Navier–Stokes equations in Sect. 4.4 is given in some more detail. Other variants, such as formulations based on time-dependent residual-based subgrid-scales, are obtained in a similar manner.

Assuming quasi-static subgrid-scales, the subgrid-scale part $\hat{\phi}$ of the scalar quantity is given as

$$\hat{\phi} = -\tau_{\text{CD}} r^h_{\text{CD}} \tag{176}$$

based on the resolved-scale part. The discrete residual of the convection–diffusion equation reads as

$$r^h_{\text{CD}} = \frac{\partial \phi^h}{\partial t} + \mathbf{u}^h \cdot \nabla \phi^h - D\Delta\phi^h - f_\phi. \tag{177}$$

Again, various definitions for the stabilization parameter τ_{CD} are provided in the literature, for instance, the form corresponding to the definition of τ_{M} for the momentum equation (see Eq. (61)):

$$\tau_{\text{CD}} = \frac{1}{\sqrt{\frac{4}{\Delta t^2} + \mathbf{u}^h \cdot \mathbf{G}\mathbf{u}^h + C_{\text{I}} D^2 \mathbf{G}:\mathbf{G}}}. \tag{178}$$

Approximation (176) for the subgrid-scale scalar quantity as well as approximation (59) for the subgrid-scale velocity are introduced into the cross- and subgrid-scale Reynolds-stress terms of the variational multiscale formulation of the convection–diffusion equation. Integrating by parts some terms and neglecting the transient and diffusive term contained in $\mathcal{B}^{1,\text{lin}}_{\text{CD}}(w^h;\hat{\phi})$ as well as potential boundary terms for the same reasons as given for the respective terms of the momentum equation in Sect. 4.4, the following residual-based stabilization terms are obtained:

$$\begin{aligned} &C_{\text{CD}}(w^h;\mathbf{u}^h,\hat{\mathbf{u}},\phi^h,\hat{\phi}) \approx \\ &\left(\mathbf{u}^h \cdot \nabla w^h, \tau_{\text{CD}} r^h_{\text{CD}}\right)_{\Omega^*} - \left(w^h, \tau_{\text{M}} \mathbf{r}^h_{\text{M}} \cdot \nabla \phi^h\right)_{\Omega^*}, \end{aligned} \tag{179}$$

$$\mathcal{R}_{\text{CD}}(w^h;\hat{\mathbf{u}},\hat{\phi}) \approx -\left(\tau_{\text{CD}} r^h_{\text{CD}} \nabla w^h, \tau_{\text{M}} \mathbf{r}^h_{\text{M}}\right)_{\Omega^*}, \tag{180}$$

$$\mathcal{B}_{\mathrm{CD}}^{1,\mathrm{lin}}(w^h;\hat{\phi}) \approx 0. \tag{181}$$

The first term of $\mathcal{C}_{\mathrm{CD}}(w^h;\mathbf{u}^h,\hat{\mathbf{u}},\phi^h,\hat{\phi})$ constitutes the SUPG term for the convection–diffusion equation.

A closed residual-based variational multiscale formulation for the convection–diffusion equation thus reads: find $\phi^h \in \mathcal{S}_\phi^h$ such that

$$\begin{aligned}&\mathcal{B}_{\mathrm{CD}}(w^h;\phi^h) + \left(\mathbf{u}^h\cdot\nabla w^h, \tau_{\mathrm{CD}} r_{\mathrm{CD}}^h\right)_{\Omega^*}\\ &- \left(w^h, \tau_{\mathrm{M}}\mathbf{r}_{\mathrm{M}}^h\cdot\nabla\phi^h\right)_{\Omega^*}\\ &- \left(\tau_{\mathrm{CD}} r_{\mathrm{CD}}^h\nabla w^h, \tau_{\mathrm{M}}\mathbf{r}_{\mathrm{M}}^h\right)_{\Omega^*} = \ell_{\mathrm{CD}}(w^h).\end{aligned} \tag{182}$$

for all $w^h \in \mathcal{V}_\phi^h$.

9.6 Small-Scale Subgrid Diffusivity

Starting from the three-scale decomposition (168) and (169), modeling the large- and small-scale equation (170) and (171) analogously to (68) and (69) and reunifying the two equations according to (73) results in: find $\phi^h \in \mathcal{S}_\phi^h$ such that

$$\mathcal{B}_{\mathrm{CD}}(w^h;\phi^h) + \left(\nabla w'^h, D'_{\mathrm{sgs}}\nabla\phi'^h\right)_\Omega = \ell_{\mathrm{CD}}(w^h). \tag{183}$$

for all $w^h \in \mathcal{V}_\phi^h$. Note that the small-scale subgrid-diffusivity term, i.e., the second term on the left-hand side, is integrated by parts, in contrast to the small-scale subgrid-viscosity term in (73). This is due to the fact that, to the best of the authors' knowledge, the present approach introducing a small-scale subgrid diffusivity has so far only been applied in the context of FEMs, where such an integration by parts is usually done. The idea of adding such a small-scale subgrid-diffusivity term for reasons of stability goes back to [94]. A more general variant of this idea can also be found in [136]. In [94], a rather general definition for the small-scale subgrid diffusivity reading

$$D'_{\mathrm{sgs}} = C_{\mathrm{t}} h, \tag{184}$$

where h denotes an (unspecified) characteristic element length and C_{t} a bounded constant, which necessarily assumes the dimension of a velocity for consistency of (184), was proposed.

To the best of the authors' knowledge, the only application of a small-scale subgrid-diffusivity formulation according to Eq. (183) to turbulent flow was reported in [87] for LES of turbulent variable-density flow at low Mach number, as addressed in Sect. 9.4. In this context, in accordance with (174), the general notation for the small-scale subgrid diffusivity D'_{sgs} in Eq. (183) is specified to be $\left(\lambda/c_p\right)'_{\mathrm{sgs}}$. For an appropriate definition of this small-scale subgrid diffusivity, for instance, the literature on traditional (all-scale) subgrid-scale modeling for LES of turbulent compressible flow might be consulted. In most of those studies, the version of the dynamic Smagorinsky model developed in [154], which extended the original proposal in [73] for incompressible flow to the compressible case and scalar transport, is used as the subgrid-scale model. For the scalar-transport equation, a subgrid diffusivity is used which is defined by the ratio of the subgrid viscosity used in the momentum equation and a turbulent Prandtl or Schmidt number, respectively, as proposed, e.g., in [59]. An overview on traditional subgrid-scale models for turbulent compressible flow can also be found in [146].

A small-scale subgrid diffusivity in analogy to the respective all-scale form used, e.g., in [154] is given as

$$\left(\frac{\lambda}{c_p}\right)'_{\mathrm{sgs}} = \frac{\mu'_{\mathrm{sgs}}}{\mathrm{Pr}_{\mathrm{sgs}}}, \tag{185}$$

where $\mathrm{Pr}_{\mathrm{sgs}}$ denotes the turbulent Prandtl number. For the numerical examples in [87], a constant value $\mathrm{Pr}_{\mathrm{sgs}} = 0.9$ was assumed. That choice was based on numerical evidence in [125, 139] for turbulent variable-density flow in a channel configuration. In [87], the resolved scales were separated into larger and smaller resolved scales via level-transfer operators from PA-AMG as addressed in Sect. 5.2.2, leading to a variable-density extension of the AVM^3. After such a scale separation, all small-scale values such as the small-scale part of the scalar quantity required for (183) are available.

The extension of the AVM^3 to variable-density flow at low Mach number was applied to two turbulent flow configurations with heating in [87]. For both examples, channel flow and flow over a backward-facing step, superior results were achieved with the AVM^3 compared to the RBVMM.

9.7 Multifractal Subgrid-Scale Modeling for Scalar Fields

The concept of structural subgrid-scale modeling is again represented by the AVM^4, which makes use of multifractal subgrid-scales and was further developed to passive scalar transport in [179]. Multifractal subgrid-scale modeling for passive scalar quantities was originally proposed in [34] and further enhanced in [179]. An elaborate derivation may also be found in [177].

To explicitly calculate the subgrid-scale scalar field, integration of its gradient field $\nabla\hat{\phi}(\mathbf{x},t)$ based on Green's function for the Laplacian is considered:

$$\hat{\phi}(\mathbf{x},t) = \frac{1}{4\pi}\int \frac{\nabla\cdot(\nabla\hat{\phi}(\check{\mathbf{x}},t))}{\|\mathbf{x}-\check{\mathbf{x}}\|}\mathrm{d}\check{\mathbf{x}}. \tag{186}$$

This relation represents the scalar analogue to the law of Biot–Savart (101). Analogously to the subgrid-scale vorticity field, the subgrid-scale scalar gradient field is reconstructed within each element by a two-step cascade process, separately recovering its magnitude $\|\nabla\hat{\phi}\|(\mathbf{x},t)$ and orientation vector $\hat{\mathbf{e}}_{\nabla\phi}(\mathbf{x},t)$, which is of unit length; that is,

$$\nabla\hat{\phi} = \|\nabla\hat{\phi}\|\hat{\mathbf{e}}_{\nabla\phi}. \tag{187}$$

The ratio of the element length h to the diffusive length scale λ_D estimates the required number of cascade steps $\mathcal{N}_\phi$ in the subgrid-scale scalar gradient cascade via

$$\mathcal{N}_\phi = \log_2\left(\frac{h}{\lambda_D}\right). \tag{188}$$

As already mentioned in Sect. 6.1, several studies showed that the diffusion-rate field of a passive scalar quantity exhibits multifractal scale similarity. Therefore, the multiplicative cascade distributes the total subgrid-scale diffusion within each element to obtain a multifractal expression for the magnitude $\|\nabla\hat{\phi}\|$ of the gradient of the subgrid-scale scalar quantity. The scalar-variance diffusion is defined as

$$\chi = D\nabla\phi\cdot\nabla\phi. \tag{189}$$

The diffusion spectrum $Z_\chi(k)$ associated with the aforementioned transport regimes scales as

$$Z_\chi(k) \sim k^\gamma, \tag{190}$$

where $\gamma = 1/3$ at inertial-convective scales and $\gamma = 1$ at viscous-convective scales. The average subgrid-scale diffusion $\hat{\chi}$ is determined depending on the average diffusion $\delta\chi^h$ at smaller resolved scales. Further decomposing the resolved scalar field ϕ^h according to the h-type three-scale separation shown in Eq. (82) for the velocity as

$$\phi = \underbrace{\overline{\phi}^h + \delta\phi^h}_{\phi^h} + \hat{\phi}, \tag{191}$$

the diffusion rates associated with the smaller resolved scales and the subgrid scales are given by

$$\delta\chi^h = D\nabla\delta\phi^h\cdot\nabla\delta\phi^h, \tag{192}$$

$$\hat{\chi} = D\nabla\hat{\phi}\cdot\nabla\hat{\phi}. \tag{193}$$

The length scale $\overline{h} = \alpha h$, which separates larger and smaller resolved scales, is assumed to be located in the inertial-convective or the viscous-convective range depending on the Schmidt number. The diffusion spectrum is integrated both from the wave number k_h to the diffusive wave number k_D,

$$\hat{\chi} = \int_{k_h}^{k_D} c_\chi k^\gamma \mathrm{d}k, \tag{194}$$

where $c_\chi > 0$ denotes the associated proportionality constant, and from $k_{\overline{h}}$ to k_h,

$$\delta\chi^h = \int_{k_{\overline{h}}}^{k_h} c_\chi k^\gamma \mathrm{d}k, \tag{195}$$

leading to an expression for the subgrid-scale diffusion that depends on the diffusion at the smaller resolved scales:

$$\hat{\chi} = \left(1-\alpha^{-(\gamma+1)}\right)^{-1}\left[\left(\frac{k_D}{k_h}\right)^{(\gamma+1)} - 1\right]\delta\chi^h. \tag{196}$$

Applying the multiplicative cascade to the resulting average subgrid-scale diffusion and introducing Eqs. (192) and (193) yields the following expression for the magnitude of the subgrid-scale scalar gradient:

$$\begin{aligned}\|\nabla\hat{\phi}\|(\mathbf{x},t) = &\left[\left(1-\alpha^{-(\gamma+1)}\right)^{-1}\right.\\ &\left.\times\left(\left(\tfrac{k_D}{k_h}\right)^{(\gamma+1)} - 1\right)\left(2^{\mathcal{N}_\phi}\right)^3\prod_{n=1}^{\mathcal{N}_\phi}\mathcal{M}_n(\mathbf{x},t)\right]^{\frac{1}{2}}\|\nabla\delta\phi^h\|.\end{aligned} \tag{197}$$

To determine the orientation $\hat{\mathbf{e}}_{\nabla\phi}$ of the gradient of the subgrid-scale scalar field, an additive decorrelation cascade is set up analogously to the one for the subgrid-scale vorticity field:

$$\hat{\mathbf{e}}_{\nabla\phi}(\mathbf{x},t) = \mathcal{I}_{\nabla\phi}\delta\mathbf{e}^h_{\nabla\phi} + \left(1-\mathcal{I}_{\nabla\phi}\right)\sum_{n=1}^{\mathcal{N}_\phi}\boldsymbol{\delta}^*_n(\mathbf{x},t), \tag{198}$$

based on the orientation $\delta\mathbf{e}^h_{\nabla\phi}$ of the gradient of the smaller resolved scales and the (modified) stochastic-decorrelation increments $\boldsymbol{\delta}^*_n$. The scalar-gradient intermittency factor $\mathcal{I}_{\nabla\phi}$ is defined from the relative orientation of $\nabla\hat{\phi}$ and $\nabla\delta\phi^h$ as

$$\mathcal{I}_{\nabla\phi} = \frac{\int\nabla\hat{\phi}\cdot\nabla\delta\phi^h\mathrm{d}\mathbf{x}}{\int\|\nabla\hat{\phi}\|\,\|\nabla\delta\phi^h\|\mathrm{d}\mathbf{x}}. \tag{199}$$

After combining cascades (197) and (198) and introducing the resulting subgrid-scale scalar gradient $\nabla\hat{\phi}$, which is assumed approximately equal to its expectation value, into Eq. (186), the subgrid-scale scalar field is calculated as

$$\begin{aligned}\hat{\phi}(\mathbf{x},t) = &\left(1-\alpha^{-(\gamma+1)}\right)^{-\frac{1}{2}}2^{\frac{3\mathcal{N}_\phi}{2}}\\ &\times\left(2^{(\gamma+1)\mathcal{N}_\phi}-1\right)^{\frac{1}{2}}\left\langle\mathcal{M}^{\frac{1}{2}}\right\rangle^{\mathcal{N}_\phi}\mathcal{I}_{\nabla\phi}\delta\phi^h(\mathbf{x},t),\end{aligned} \tag{200}$$

where assumptions analogous to the ones discussed in Sect. 6.5 for the subgrid-scale vorticity are incorporated. Furthermore, k_D/k_h is replaced by relation (188). The required independence of $\hat{\phi}$ from $\mathcal{N}_\phi$ as $\mathcal{N}_\phi\to\infty$, i.e., the high-Reynolds-number limit, constrains $\mathcal{I}_{\nabla\phi}$ as

$$\mathcal{I}_{\nabla\phi} \sim 2^{-\left(\frac{\gamma+1}{2}+\frac{3}{2}\right)\mathcal{N}_\phi}\left\langle\mathcal{M}^{\frac{1}{2}}\right\rangle^{-\mathcal{N}_\phi}. \tag{201}$$

Eventually, the subgrid-scale scalar quantity $\hat{\phi}$ reads

$$\hat{\phi}(\mathbf{x},t) = B_\phi \delta\phi^h(\mathbf{x},t), \tag{202}$$

where

$$B_\phi = C_{\text{sgs}}^{B_\phi}\left(1-\alpha^{-(\gamma+1)}\right)^{-\frac{1}{2}} 2^{-\frac{(\gamma+1)\mathcal{N}_\phi}{2}}\left(2^{(\gamma+1)\mathcal{N}_\phi}-1\right)^{\frac{1}{2}}. \tag{203}$$

The required proportionality constant is denoted by $C_{\text{sgs}}^{B_\phi}$. Parameter $C_{\text{sgs}}^{B_\phi}$ should exhibit a universal dependence on the Reynolds number and satisfy the same characteristics as discussed for C_{sgs}^{B} in Sect. 6.6. Based on the evaluations presented in [34], $C_{\text{sgs}}^{B_\phi}$ is expected to be approximately equal to or somewhat higher than C_{sgs}^{B} depending on the Reynolds number.

With respect to low- and high-Schmidt-number passive scalar mixing and the resulting transport regimes, it is crucial to explicitly distinguish between the number of cascade steps $\mathcal{N}_\mathbf{u}$ in the vorticity cascade and the number of cascade steps $\mathcal{N}_\phi$ in the scalar-gradient cascade. According to Fig. 8, different levels of resolution have to be considered in the velocity and scalar field for $\text{Sc} \neq 1$, and a potentially different number of cascade steps in both cascades is expected. The number of cascade steps $\mathcal{N}_\mathbf{u}$ in the vorticity cascade is estimated via the ratio of the element length h to the viscous length scale λ_ν as given in equation (103). According to Eq. (125), the ratio of h to λ_ν is approximated using the local element Reynolds number Re_h. The ratio of λ_D to λ_ν may be estimated based on the Schmidt number:

$$\frac{\lambda_D}{\lambda_\nu} = \text{Sc}^{-\varphi}, \tag{204}$$

where $\varphi = 3/4$ for $\text{Sc} \leq 1$ and $\varphi = 1/2$ for $\text{Sc} \gg 1$, as presented in Sect. 9.2. Combining this relation with Eq. (125) leads to an approximation for the ratio of h to λ_D:

$$\frac{h}{\lambda_D} = c_\nu \text{Re}_h^{\frac{3}{4}} \text{Sc}^{\varphi}, \tag{205}$$

resulting in a higher number of steps $\mathcal{N}_\phi$ in the scalar gradient cascade than in the vorticity cascade for $\text{Sc} \gg 1$ and vice versa for $\text{Sc} < 1$.

The final modeled variational multiscale formulation of the convection–diffusion equation is obtained by inserting approximation (202) into the cross- and subgrid-scale Reynolds-stress terms, (165) and (166), and adding an appropriate residual-based stabilization term to ensure proper stabilization of the numerical method as discussed in Sect. 6.7: find $\phi^h \in \mathcal{S}_\phi^h$ such that

$$\begin{aligned}
&\mathcal{B}_{\text{CD}}(w^h;\phi^h) \\
&+\left(w^h, \mathbf{u}^h \cdot \nabla\left(B_\phi \delta\phi^h\right) + B\delta\mathbf{u}^h \cdot \nabla\phi^h\right)_{\Omega^*} \\
&+\left(w^h, B\delta\mathbf{u}^h \cdot \nabla\left(B_\phi \delta\phi^h\right)\right)_{\Omega^*} \\
&+\left(\mathbf{u}^h \cdot \nabla w^h, \tau_{\text{CD}} r_{\text{CD}}^h\right)_{\Omega^*} = \ell_{\text{CD}}(w^h)
\end{aligned} \tag{206}$$

for all $w^h \in \mathcal{V}_\phi^h$. The modeled forms of the cross- and subgrid-scale Reynolds-stress terms can be found in the second and third line. The residual-based stabilization term, i.e., the SUPG term, is given in the fourth line on the left-hand side. Again, the required small-scale scalar field is obtained from the resolved field by scale separation based on level-transfer operators from PA-AMG as outlined in Sect. 5.2.2.

The resulting AVM^4 was applied to turbulent channel flow with passive scalar transport in [179]. A broad range of Schmidt numbers from 1 up to 1000 was considered. Compared to an RBVMM, improved results were obtained for all Schmidt numbers. Moreover, the predicted values for the transfer coefficient, which describes the transfer of the scalar quantity from the wall to the fluid, replicated the theoretical correlation with the Schmidt number for the entire considered range up to 1000.

In a subsequent study by the same authors, published in [178], the AVM^4 was further enhanced to active scalar transport in the context of turbulent variable-density flow at low Mach number. Therefore, the multifractal reconstruction procedure for subgrid-scale scalar quantities described above was applied to the temperature field. A variable-density extension was considered for subgrid-scale modeling in the momentum equation. Applications of the AVM^4 to turbulent flow in a channel with a heated and a cooled wall as well as to turbulent flow over a backward-facing step with heating were investigated in [178], and improved results compared to the ones predicted by a form of the RBVMM were obtained.

10 Turbulent Two-Phase Flow and Combustion

In this section, the ensemble of turbulent flow problems which have been addressed by VMMs is extended by taking into account two of the most important applications involving moving interfaces: two-phase flow and combustion. These two problems share several aspects such as an interface usually assumed to be very thin. However, there are also differences, e.g., related to diffusive–reactive processes propagating the interface, that is, the flame front, in combustion or related to surface-tension effects encountered at the phase interface in two-phase flow. At the outset of this section, it has to be emphasized that the presence of moving interfaces in the flow field, such as phase interfaces in two-phase flow and flame fronts in premixed combustion, comes along with additional requirements regarding the computational method. The method predominantly chosen in the studies reviewed in this section to enhance the basic VMM to enable the handling of the interfaces appearing in

two-phase flow and combustion is the XFEM, which has already been briefly addressed in Sect. 8.3.

10.1 Two-Phase Flow

Two contiguous bulk fluids separated by a deformable interface are assumed. Each of the two individual fluid flows may be turbulent, and interactions of the turbulent structures with the interface may occur. In LES of such configurations, the subdomains occupied by the two fluids are covered by the computational grid. Hence, there is the same modeling situation for the flow in each fluid subdomain as for turbulent single-phase flow. Depending on whether the interface may be assumed as resolved in a DNS-like manner or not, additional subgrid-scale modeling regarding underresolved interfaces may have to be taken into account; see, e.g., [131] for theoretical considerations on this issue. In fact, the derivation of appropriate interfacial subgrid-scale models is still in its infancy.

The interface $\Gamma_{\text{int}}(t)$ is commonly assumed infinitely thin and thus considered as a discontinuity in the flow field. A localized surface-tension force acts at the interface, and the density as well as the viscosity change discontinuously, giving rise to strong and/or weak discontinuities in the pressure field p and the velocity field $\mathbf{u}$, which are expressed in terms of two jump conditions:

$$[[\mathbf{u}]] = 0 \quad \text{on } \Gamma_{\text{int}}, \tag{207}$$

$$[\![-p_{\text{hyd}}\mathbf{I} + 2\mu\boldsymbol{\varepsilon}(\mathbf{u})]\!] \cdot \mathbf{n}_{\text{int}} = \gamma\kappa\mathbf{n}_{\text{int}} \quad \text{on } \Gamma_{\text{int}}. \tag{208}$$

These conditions, making use of the jump operator $[[\cdot]] := (\cdot)_- - (\cdot)_+$, are obtained from the conservation principles of mass and momentum across the interface (see, e.g., [210]) and couple the fluid flows in both subdomains, each governed by the Navier–Stokes equations. Variables and subdomains corresponding to the first and the second fluid are labeled by $(\cdot)_+$ and $(\cdot)_-$, respectively. By definition, the unit normal vector $\mathbf{n}_{\text{int}}(t)$ on the interface points from the subdomain $\Omega_+(t)$ to the subdomain $\Omega_-(t)$. Furthermore, μ denotes the dynamic viscosity, γ the surface-tension coefficient, which is assumed constant, and $\kappa = \nabla \cdot \mathbf{n}_{\text{int}}$ the curvature of the interface.

Various strategies to represent the interface in two-phase-flow simulations may be found in the literature, for instance, the Arbitrary Lagrangian-Eulerian (ALE) approach, the level-set method and the volume-of-fluid method; see, e.g., [192] for a review and [58] for an overview with an emphasis on FEMs. In the context of VMMs for LES of turbulent two-phase flow, merely the level-set method appears to have been applied. The level-set method describes the interface implicitly via the zero iso-contour of a signed distance function $\varphi(\mathbf{x}, t)$ and, thus, constitutes a convenient way to represent interfaces that are subject to large and complex deformations as encountered in turbulent flow. Based on φ, the two fluid subdomains Ω_+ and Ω_- as well as the interface are identified as

$$\varphi(\mathbf{x},t)\begin{cases} < 0 & \forall\, \mathbf{x} \in \Omega_-(t), \\ = 0 & \forall\, \mathbf{x} \in \Gamma_{\text{int}}(t), \\ > 0 & \forall\, \mathbf{x} \in \Omega_+(t). \end{cases} \tag{209}$$

The evolution of φ is mathematically governed by the advection equation

$$\frac{\partial\varphi}{\partial t} + \mathbf{u}\cdot\nabla\varphi = 0 \quad \text{in } \Omega, \tag{210}$$

where the velocity $\mathbf{u}(\mathbf{x}, t)$ is obtained from the Navier–Stokes equations. Using φ, the unit normal vector on the interface is given by $\mathbf{n}_{\text{int}} = -\nabla\varphi/\|\nabla\varphi\|$. Residual-based stabilization methods for the level-set equation (210) were suggested, e.g., in [126, 159].

However, capturing the interface implicitly by means of the level-set method leads to elements (or cells) that are cut by the interface, such that the aforementioned discontinuities occur within the element itself. Two approaches to cope with discontinuities inside elements are commonly distinguished, which both have already been considered for LES within the framework of the VMM. A straightforward way to deal with discontinuities in the element interior consists of artificially thickening the interface over several elements. As a result, physical parameters are smoothly blended from one fluid to the other, and surface tension is incorporated via a local volume force, for instance, by using the continuum surface force model proposed in [22]. LESs based on RBVMMs, making use of smeared interfaces, were presented, e.g., in [2, 184]. Alternatively, the interface may be treated in

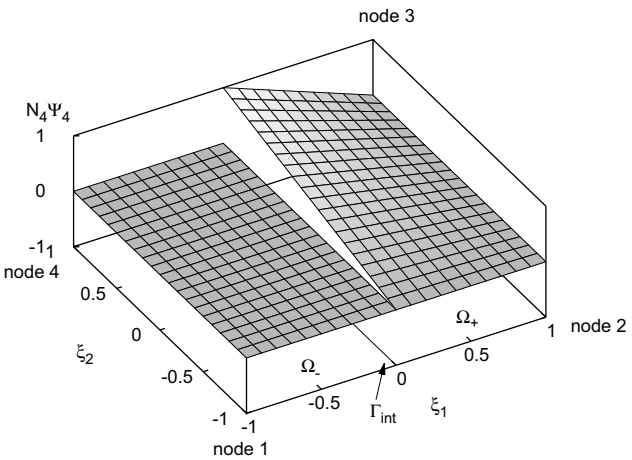

Fig. 9 Jump-enriched shape function corresponding to node 4 of a bilinearly-interpolated quadrilateral element

a sharp fashion, as enabled, e.g., by the XFEM. XFEMs and similar methods for two-phase flow were proposed, e.g., in [43, 98, 124, 181, 191, 193]. Based on appropriate enrichment functions that are able to represent jumps and/or kinks in the pressure and velocity field, discontinuities in the element interior are recovered.

For instance, the face-oriented stabilized Nitsche-type XFEM suggested in [193] incorporates jump enrichments for both the velocity and the pressure field. The applied jump enrichment is based on a symmetric Heaviside function and allows for reproducing discontinuities in the primary field as well as in its gradient. Figure 9 illustrates the enriched shape function for one node of a two-dimensional bilinearly-interpolated quadrilateral element. As the velocity field merely exhibits a kink, but not a jump, Nitsche's method [160], which was originally considered for elliptic problems with embedded interfaces in [97], is used to weakly couple the two individual fluid flows. For further details on Nitsche's method, the reader is referred to the references already provided in Sect. 8.2 as well as to, e.g., [32] for a review in the context of embedded interfaces.

Moreover, face-oriented ghost-penalty and fluid stabilization terms are applied to intersected elements. Face-oriented ghost-penalty stabilization terms, first presented for elliptic problems in [30] and later further developed for problems governed by the Stokes equations by the same authors in [31], ensure numerical stability for arbitrary interface locations. Further face-oriented fluid stabilization terms in the interface region enhance the method to high-Reynolds-number flows governed by the Navier–Stokes equations; see also Section 4 for FOS methods in general as well as [194] for application together with face-oriented ghost-penalty stabilization terms to incompressible flow problems with embedded boundaries. Residual-based stabilization terms in the interior of the fluid subdomains complete the Nitsche-type XFEM proposed in [193].

In [182], the Nitsche-type XFEM as introduced in [193] was applied in conjunction with the AVM^4, which has been presented in Sect. 6.8, to LES of turbulent two-phase flow; that is, the effect of the subgrid scales was taken into account by multifractal subgrid-scale modeling. The entire method was referred to as the XAVM^4. For application to LES of turbulent channel flow carrying a bubble of the size of the channel half-width in [182], it was assumed that the interface is represented in a DNS-like manner.

10.2 Combustion

Combustion processes are encountered in a variety of technical systems; see, e.g., [172, 218, 221] for textbooks introducing into the topic. Gaseous combustion, one of the main types of combustion in practice, represents a reacting flow, characterized by a strong and irreversible heat release within very thin flame fronts. Mathematically, problems of combustion in the predominant form of deflagrations (i.e., flames at low speed) are usually described by a variable-density formulation of the Navier–Stokes equations for low-speed flows as addressed in Sect. 9.4. Three different types of combustion are usually distinguished: non-premixed, premixed and partially premixed combustion. For a premixed flame, which will be focused on in the following, a perfect mixing of the reactants before entering the reaction zone is assumed. The characteristic feature of premixed combustion is the propagation of the flame front towards the unburned gases as a result of diffusive–reactive processes.

In technical processes, combustion almost always takes place in a turbulent form; see, e.g., [15, 39, 166]. The scales of turbulent combustion are even smaller than the smallest turbulent flow scales. More precisely, the aforementioned very thin flame fronts, within which the chemical reactions proceed, are usually smaller than the Kolmogorov scale. Hence, the combustion-related scales are distinctly separated from the scales of turbulence. Due to this, according to [166], almost all turbulent combustion models explicitly or implicitly assume scale separation. This assumption is reflected, among others, by the so-called laminar flamelet concept, which is elaborated on in [166]. Based on such flamelet models, a turbulent flame is considered as an ensemble of thin quasi-laminar structures, the flamelets. These flamelets are embedded in an otherwise non-reacting turbulent flow field. From a scale-separation or flamelet perspective, respectively, the propagating flame front characterizing turbulent premixed combustion is typically considered as an almost infinitely thin interface within the turbulent flow field, separating the burned from the unburned gas.

LES of turbulent combustion still represents a relatively new field of research, which mostly started to develop not until the end of the 1990s; see, e.g., [77, 113, 171] for reviews. Beyond the closure problems also appearing in turbulent flow/transport problems, which have already been addressed above, the closure problem characteristic for turbulent combustion is related to the chemical source term appearing in the respective system of equations. A particular problem related to LES of premixed combustion is due to the fact that, in most of the cases, the flame is entirely on a subgrid scale. An adequate resolution would require a substantially increased number of computational degrees of freedom, as outlined, e.g., in [171]. According to [113], the majority of contributions dealing with LES for turbulent combustion focus on the applicability of RANS-type combustion models to LES to provide a closure for the filtered chemical source term. These closures are

typically developed from physical analysis. Three different approaches may be distinguished in this context according to [213]: a geometrical approach, an approach based on turbulent mixing, and a purely statistical approach. In the following, it will be focused on two geometrical approaches, the progress-variable (or c-equation) and the level-set/G-equation approach, which represent the state of the art in the context of premixed combustion modeling according to [113], aside from linear eddy modeling (see, e.g., [41]) and models based on probability density functions. Both models, which will be focused on in the remainder of this section, are based on the laminar flamelet concept, and their tight relationship is detailed, e.g., in [39].

Underlying the progress-variable approach is the Bray-Moss-Libby (BML) modeling assumption originally proposed in [23]. Based on the progress variable c, the conservation equations for mass fractions and energy, which are part of the system of equations for combustion, are replaced by the (single) conservation equation for c. This progress-variable equation reads

$$\rho\frac{\partial c}{\partial t} + \rho\mathbf{u}\cdot\nabla c - \nabla\cdot\left(\rho D_T\nabla c\right) = \dot{\omega}_c \quad \text{in } \Omega, \tag{211}$$

where $\dot{\omega}_c$ denotes the chemical source term of this c-equation and D_T the thermal diffusivity (see Sect. 9.4 for definition). It is assumed that the progress variable takes the value $c = 0$ in the unburned phase and the value $c = 1$ in the burned phase. As shown in [89], defining a reaction coefficient σ subject to

$$\dot{\omega}_c = \rho\sigma(1-c), \tag{212}$$

for which a certain chemical kinetics, such as Arrhenius chemical kinetics, may be chosen, the progress-variable equation may be reformulated in the schematic form of an instationary convection-diffusion-reaction equation with non-zero right-hand side:

$$\rho\frac{\partial c}{\partial t} + \rho\mathbf{u}\cdot\nabla c - \nabla\cdot\left(\rho D_T\nabla c\right) + \rho\sigma c = \rho\sigma \quad \text{in } \Omega. \tag{213}$$

The RBVMM and the AVM^3 were applied to the numerical example case of a flame-vortex interaction assuming Arrhenius chemical kinetics in [89]. This actually laminar reactive flow problem may serve as a model problem for interactions of turbulent flows and (premixed) flames. The evolution of both a pocket of unburned gas and a secluded, drop-like structure, which detaches itself and moves into the burned gas, were accurately predicted already for a relatively coarse discretization in [89].

A level-set/G-equation valid for both the corrugated-flamelets and the thin-reaction-zones regime, the most important regimes of turbulent premixed combustion, according to [166] (to which the reader is also referred for more details on those regimes) reads

$$\frac{\partial G}{\partial t} + \mathbf{u}\cdot\nabla G + \left(s_\mathrm{L}^0 - D_T\kappa\right)\mathbf{n}_\mathrm{int}\cdot\nabla G = 0 \quad \text{in } \Omega, \tag{214}$$

where $G(\mathbf{x},t)$ replaces φ of the level-set equation (210). Hence, the location of the flame front, representing the interface Γ_int in the present case, is given by the zero level set of G, that is, $G(\mathbf{x},t) = 0$. The burned phase is identified as the subdomain defined by $G > 0$ and the unburned phase as the subdomain defined by $G < 0$. Accordingly, the unit normal vector $\mathbf{n}_\mathrm{int}$ at the flame front points from the burned phase into the unburned phase. The curvature of the flame front is denoted by κ and also calculated as shown in Sect. 10.1. In Eq. (214), the laminar burning velocity of the unstretched planar flame s_L^0 (i.e., the burning velocity without curvature effects, in particular) is used, which is related to the laminar burning velocity s_L via

$$s_\mathrm{L} = s_\mathrm{L}^0\left(1 - L_\mathrm{M}\kappa\right), \tag{215}$$

based on the Markstein length L_M.

As aforementioned, the flame front, which propagates with the laminar burning velocity according to the laminar flamelet concept, is assumed to be infinitely thin. Consequently, constant densities ρ_u in the unburned and ρ_b in the burned phase can be assumed. However, jump conditions need to be formulated at the flame front. These jump conditions are derived from mass and momentum conservation across the interface (see, e.g., [221]). Assuming continuity of the tangential velocity components, among others, the jump conditions may eventually be formulated as

$$[[\mathbf{u}]] = -\rho_\mathrm{u}s_\mathrm{L}[[\rho^{-1}]]\mathbf{n}_\mathrm{int} \quad \text{on } \Gamma_\mathrm{int}, \tag{216}$$

$$[[-p_\mathrm{hyd}\mathbf{I} + 2\mu\boldsymbol{\varepsilon}(\mathbf{u})]]\cdot\mathbf{n}_\mathrm{int} = \left(\rho_\mathrm{u}s_\mathrm{L}\right)^2[[\rho^{-1}]]\mathbf{n}_\mathrm{int} \quad \text{on } \Gamma_\mathrm{int}. \tag{217}$$

By comparing mass-conservation equation (216) to the respective equation (207) for two-phase flow, one of the main differences between these two phenomena, that is, the acceleration through the flame front for combustion in contrast to the continuity of the velocity at the interface for two-phase flow, may easily be observed as a consequence of the non-zero right-hand side of (216).

In [18], among others, using a level-set/G-equation formulation, a piloted Bunsen burner flame was investigated by an XFEM including a distributed Lagrange multiplier approach for enforcing the interface conditions at the flame front, which has not been explicitly addressed here. An RBVMM for the level-set/G-equation formulation and an XFEM using Nitsche's method for enforcing the interface conditions at the flame front together with a semi-Lagrangian time-integration procedure proposed in [103] was applied to several combustions problems such as a spherical flame, two- and three-dimensional Bunsen burner flames and a flame-vortex interaction in [102].

11 Conclusions

The variational multiscale method was introduced about twenty years ago, and it has been exploited for developing computational methods for large-eddy simulation of turbulent flow since the beginning of this century. Already in 2006, articles reviewing the early years of the variational multiscale method for large-eddy simulation were published in [80, 118]. Now, a decade later, the developments in this context have broadened and intensified considerably, such that the time has come for reviewing again, glancing at the progress which has been made in the meantime. In contrast to another review article published almost simultaneously in [1] as well as the aforementioned earlier reviews, which all entirely focused on large-eddy simulation of turbulent incompressible flow, the present one has aimed at additionally covering further aspects of numerically simulating turbulent flow as well as applications beyond incompressible single-phase flow.

After having introduced the incompressible Navier–Stokes equations, the fundamental concepts of and traditional approaches to large-eddy simulation, respectively, as well as the variational multiscale formulation, the core part of this review article has been dedicated to the various concepts for subgrid-scale modeling within the variational multiscale method for large-eddy simulation proposed by researchers in this field to date. These concepts comprise (i) implicit large-eddy simulation, represented by residual-based and stabilized methods, (ii) functional subgrid-scale modeling via small-scale subgrid-viscosity models and (iii) structural subgrid-scale modeling, which has so far merely been realized via the introduction of multifractal subgrid scales. All of these subgrid-scale modeling approaches were initially introduced for large-eddy simulation of turbulent incompressible flow in the literature and, accordingly, have been outlined for this application in this article as well. Afterwards, an overview on exemplary numerical test cases to which variational multiscale methods for large-eddy simulation have been applied in the past years has been provided. In particular, computational results obtained from turbulent channel flow, which appears to be the numerical example mostly used in the literature for evaluating the presented methods, have been explicitly shown and compared.

In the remainder of this article, as aforementioned, the focus was on particularly important issues such as wall-layer modeling and applications beyond incompressible single-phase flow. Wall-layer modeling is an aspect for large-eddy simulation of wall-bounded turbulent flow which becomes particularly relevant at very high Reynolds number. In fact, in the last two decades and thus mostly in parallel with the developments for variational multiscale methods for large-eddy simulation, the interest in approaches to wall-layer modeling has notably increased. In the last two sections of this review article, passive and active scalar transport has been considered, and developments for large-eddy simulation of turbulent two-phase flow and combustion have been briefly covered. All of these applications introduce additional challenges which need to be addressed adequately within the overall framework of a variational multiscale method.

Future developments regarding the variational multiscale method for large-eddy simulation will most likely be found in the context of both focal points of this article. On the one hand, advanced subgrid-scale modeling will be a key issue to obtain (further) improved results. On the other hand, the variational multiscale method for large-eddy simulation will need to be advanced with a view to further and potentially even more complex applications such as multiphysics problems.

Compliance with Ethical Standards

Conflicts of interest The authors declare that they have no conflict of interest.

References

1. Ahmed N, Chacón Rebollo T, John V, Rubino S (2017) A review of variational multiscale methods for the simulation of turbulent incompressible flows. Arch Comput Methods Eng 24:115. doi: 10.1007/s11831-015-9161-0
2. Akkerman I, Bazilevs Y, Kees CE, Farthing MW (2011) Isogeometric analysis of free-surface flow. J Comput Phys 230:4137–4152
3. Araya G, Bohr E, Jansen K, Castillo L, Peterson K (2006) Generation of turbulent inlet conditions for thermal/velocity boundary layer simulations. AIAA Paper 2006-0699, Reno, NV
4. Avila M, Codina R, Principe J (2014) Large eddy simulation of low Mach number flows using dynamic and orthogonal subgrid scales. Comput Fluids 99:44–66
5. Balaras E, Benocci C, Piomelli U (1996) Two layer approximate boundary conditions for large-eddy simulations. AIAA J 34:1111–1119
6. Bardina J, Ferziger JH, Reynolds WC (1980) Improved subgrid models for large eddy simulation. AIAA Paper 1980-1357, Snowmass, CO
7. Bardina J, Ferziger JH, Reynolds WC (1983) Improved turbulence models based on large eddy simulation of homogeneous, incompressible, turbulent flows. Technical Report TF-19, Thermosciences Division, Department of Mechanical Engineering, Stanford University
8. Bauer G, Gamnitzer P, Gravemeier V, Wall WA (2013) An isogeometric variational multiscale method for large-eddy simulation of coupled multi-ion transport in turbulent flow. J Comput Phys 251:194–208
9. Bazilevs Y, Calo VM, Cottrell JA, Hughes TJR, Reali A, Scovazzi G (2007) Variational multiscale residual-based turbulence modeling for large eddy simulation of incompressible flows. Comput Methods Appl Mech Eng 197:173–201

10. Bazilevs Y, Hughes TJR (2007) Weak imposition of Dirichlet boundary conditions in fluid mechanics. Comput Fluids 36:12–26
11. Bazilevs Y, Michler C, Calo VM, Hughes TJR (2010) Isogeometric variational multiscale modeling of wall-bounded turbulent flows with weakly enforced boundary conditions on unstretched meshes. Comput Methods Appl Mech Eng 199:780–790
12. Becker R, Braack M (2001) A finite element pressure gradient stabilization for the Stokes equations based on local projections. Calcolo 38:173–199
13. Belytschko T, Black T (1999) Elastic crack growth in finite elements with minimal remeshing. Int J Numer Methods Eng 45:601–620
14. Berselli LC, Iliescu T, Layton WJ (2006) Mathematics of large eddy simulation of turbulent flows. Springer, Berlin
15. Bilger RW, Pope SB, Bray KNC, Driscoll JF (2005) Paradigms in turbulent combustion research. Proc Combust Inst 30:21–42
16. Bochev PB, Gunzburger MD, Lehoucq RB (2007) On stabilized finite element methods for the Stokes problem in the small time step limit. Int J Numer Methods Fluids 53:573–597
17. Boris JP, Grinstein FF, Oran ES, Kolbe RL (1992) New insights into large-eddy simulation. Fluid Dyn Res 10:199–228
18. van der Bos F, Gravemeier V (2009) Numerical simulation of premixed combustion using an enriched finite element method. J Comput Phys 228:3605–3624
19. van der Bos F, van der Vegt JJW, Geurts BJ (2007) A multiscale formulation for compressible turbulent flows suitable for general variational discretization techniques. Comput Methods Appl Mech Eng 196:2863–2875
20. Braack M, Burman E (2006) Local projection stabilization for the Oseen problem and its interpretation as a variational multiscale method. Comput Methods Appl Mech Eng 43:2544–2566
21. Braack M, Burman E, John V, Lube G (2007) Stabilized finite element methods for the generalized Oseen problem. Comput Methods Appl Mech Eng 196:853–866
22. Brackbill JU, Kothe DB, Zemach C (1992) A continuum method for modeling surface tension. J Comput Phys 100:335–354
23. Bray KNC, Moss JB (1977) A unified statistical model of the premixed turbulent flame. Acta Astronaut 4:291–319
24. Brezzi F, Fortin M (1991) Mixed and hybrid finite element methods. Springer, New York
25. Brezzi F, Franca LP, Hughes TJR, Russo A (1997) $b = \int g$. Comput Methods Appl Mech Eng 145:329–339
26. Brooks AN, Hughes TJR (1982) Streamline Upwind/Petrov-Galerkin formulations for convection dominated flows with particular emphasis on the incompressible Navier-Stokes equations. Comput Methods Appl Mech Eng 32:199–259
27. Buch KA, Dahm WJA (1998) Experimental study of the fine-scale structure of conserved scalar mixing in turbulent shear flows. Part 2. $Sc \approx 1$. J Fluid Mech 364:1–29
28. Burman E, Fernández MA, Hansbo P (2006) Continuous interior penalty finite element method for Oseen's equations. SIAM J Numer Anal 44:1248–1274
29. Burman E, Hansbo P (2004) Edge stabilization for Galerkin approximations of convection-diffusion-reaction problems. Comput Methods Appl Mech Eng 193:1437–1453
30. Burman E, Hansbo P (2012) Fictitious domain finite element methods using cut elements: II. A stabilized Nitsche method. Appl Numer Math 62:328–341
31. Burman E, Hansbo P (2014) Fictitious domain methods using cut elements: III. A stabilized Nitsche method for Stokes' problem. ESAIM. Math Model Numer Anal 48:859–874
32. Burman E, Zunino P (2012) Numerical approximation of large contrast problems with the unfitted Nitsche method. In: Blowey J, Jensen M (eds) Frontiers in numerical analysis. Lecture Notes in Computational Science and Engineering, vol 85. Springer, Berlin, pp 227–282
33. Burton GC (2003) A multifractal subgrid-scale model for large-eddy simulation of turbulent flows. Dissertation, The University of Michigan
34. Burton GC (2008) The nonlinear large-eddy simulation method applied to $Sc \approx 1$ a*nd* $Sc \gg 1$ passive-scalar mixing. Phys Fluids 20:035103
35. Borton GC, Dahm WJA (2005) Multifractal subgrid-scale modeling for large-eddy simulation. I. Model development and a priori testing. Phys Fluid 17:075111
36. Burton GC, Dahm WJA (2005) Multifractal subgrid-scale modeling for large-eddy simulation. II. Backscatter limiting and a posteriori evaluation. Phys Fluids 17:075112
37. Cabot W, Moin P (1999) Approximate wall boundary conditions in the large-eddy simulation of high Reynolds number flows. Flow Turbul Combust 63:269–291
38. Calo VM (2004) Residual-based multiscale turbulence modeling: Finite volume simulations of bypass transition. Dissertation, Stanford University
39. Cant RS, Mastorakos E (2008) An introduction to turbulent reacting flows. Imperial College Press, London
40. Chacón Rebollo T, Gómez Mármol M, Rubino S (2015) Numerical analysis of a finite element projection-based VMS turbulence model with wall laws. Comput Methods Appl Mech Eng 285:379–405
41. Chakravarthy VK, Menon S (2001) Large-eddy simulation of turbulent premixed flames in the flamelet regime. Combust Sci Technol 162:175–222
42. Chapman DR (1979) Computational aerodynamics development and outlook. AIAA J 17:1293–1313
43. Chessa J, Belytschko T (2003) An extended finite element method for two-phase fluids. J Appl Mech 70:10–17
44. Choi H, Moin P (1994) Effects of the computational time step on numerical solutions of turbulent flow. J Comput Phys 113:1–4
45. Choi H, Moin P (2012) Grid-point requirements for large eddy simulation: Chapman's estimates revisited. J Comput Phys 24:011702
46. Chung J, Hulbert GM (1993) A time integration algorithm for structural dynamics with improved numerical dissipation: the generalized-α method. J Appl Mech 60:371–375
47. Codina R (2002) Stabilized finite element approximation of transient incompressible flows using orthogonal subscales. Comput Methods Appl Mech Eng 191:4295–4321
48. Codina R, Principe J, Avila M (2010) Finite element approximation of turbulent thermally coupled incompressible flows with numerical sub-grid scale modelling. Int J Numer Methods Heat Fluid Flow 20:492–515
49. Codina R, Principe J, Guasch O, Badia S (2007) Time dependent subscales in the stabilized finite element approximation of incompressible flow problems. Comput Methods Appl Mech Eng 196:2413–2430
50. Collis SS (2002) The DG/VMS method for unified turbulence simulation. AIAA Paper 2002-3124, St. Louis, MO
51. Collis SS (2001) Monitoring unresolved scales in multiscale turbulence modeling. Phys Fluids 13:1800–1806
52. Colomés O, Badia S, Codina R, Principe J (2015) Assessment of variational multiscale models for the large eddy simulation of turbulent incompressible flows. Comput Methods Appl Mech Eng 285:32–63
53. Comerford A, Gravemeier V, Wall WA (2013) An algebraic variational multiscale-multigrid method for large-eddy simulation of turbulent pulsatile flows in complex geometries with

detailed insight into pulmonary airway flow. Int J Numer Methods Fluids 71:1207–1225
54. De Mulder T (1998) The role of bulk viscosity in stabilized finite element formulations for incompressible flow: a review. Comput Methods Appl Mech Eng 163:1–10
55. Deardorff JW (1970) A numerical study of three-dimensional turbulent channel flow at large Reynolds numbers. J Fluid Mech 41:453–480
56. Domaradzki JA, Adams NA (2002) Direct modeling of subgrid-scales of turbulence in large eddy simulation. J Turbul 3:024
57. Domaradzki JA, Loh K (1999) The subgrid-scale estimation model in the physical space representation. Phys Fluids 11:2330–2342
58. Elgeti S, Sauerland H (2016) Deforming fluid domains within the finite element method: five mesh-based tracking methods in comparison. Arch Comput Methods Eng 23:323–361
59. Erlebacher G, Hussaini MY, Speziale CG, Zang TA (1992) Toward the large-eddy simulation of compressible turbulent flows. J Fluid Mech 238:155–185
60. Farhat C, Rajasekharan A, Koobus B (2006) A dynamic variational multiscale method for large eddy simulations on unstructured meshes. Comput Methods Appl Mech Eng 195:1667–1691
61. Fedorchenko AT (1997) A model of unsteady subsonic flow with acoustics excluded. J Fluid Mech 334:135–155
62. Franca LP, Hughes TJR (1988) Two classes of mixed finite element methods. Comput Methods Appl Mech Eng 69:89–129
63. Franca LP, Nesliturk A (2001) On a two-level finite element method for the incompressible Navier-Stokes equations. Int J Numer Methods Eng 52:433–453
64. Frederiksen RD, Dahm WJA, Dowling DR (1997) Experimental assessment of fractal scale similarity in turbulent flows. Part 3. Multifractal scaling. J Fluid Mech 338:127–155
65. Fries TP, Belytschko T (2010) The extended/generalized finite element method: an overview of the method and its applications. Int J Numer Methods Eng 84:253–304
66. Fröhlich J, Rodi W (2002) Introduction to large eddy simulation of turbulent flows. In: Launder BE, Sandham ND (eds) Closure strategies for turbulent and transitional flows. Cambridge University Press, Cambridge, pp 267–298
67. Fröhlich J, von Terzi D (2008) Hybrid LES/RANS methods for the simulation of turbulent flows. Prog Aerosp Sci 44:349–377
68. Gamnitzer P, Gravemeier V, Wall WA (2010) Time-dependent subgrid scales in residual-based large eddy simulation of turbulent channel flow. Comput Methods Appl Mech Eng 199:819–827
69. Gamnitzer P, Gravemeier V, Wall WA (2012) A mixed/hybrid Dirichlet formulation for wall-bounded flow problems including turbulent flow. Comput Methods Appl Mech Eng 245–246:22–35
70. Garnier E, Adams N, Sagaut P (2009) Large eddy simulation for compressible flows. Springer, New York
71. Georgiadis NJ, Rizzetta DP, Fureby C (2010) Large-eddy simulation: current capabilities, recommended practices, and future research. AIAA J 48:1772–1784
72. Germano M (1992) Turbulence: the filtering approach. J Fluid Mech 238:325–336
73. Germano M, Piomelli U, Moin P, Cabot WH (1991) A dynamic subgrid-scale eddy viscosity model. Phys Fluids A 3:1760–1765
74. Gerstenberger A, Wall WA (2010) An embedded Dirichlet formulation for 3D continua. Int J Numer Methods Eng 82:537–563
75. Geurts BJ (2004) Elements of direct and large eddy simulation. R. T. Edwards, Philadelphia
76. Ghosal S, Lund TS, Moin P, Akselvoll K (1995) A dynamic localization model for large-eddy simulation of turbulent flows. J Fluid Mech 286:229–255
77. Gicquel LYM, Staffelbach G, Poinsot T (2012) Large eddy simulation of gaseous flames in gas turbine combustion chambers. Prog Energy Combust Sci 38:782–817
78. Gravemeier V (2006) A consistent dynamic localization model for large eddy simulation of turbulent flows based on a variational formulation. J Comput Phys 218:677–701
79. Gravemeier V (2006) Scale-separating operators for variational multiscale large eddy simulation of turbulent flows. J Comput Phys 212:400–435
80. Gravemeier V (2006) The variational multiscale method for laminar and turbulent flow. Arch Comput Methods in Eng 13:249–324
81. Gravemeier V (2007) Variational multiscale large eddy simulation of turbulent flow in a diffuser. Comput Mech 39:477–495
82. Gravemeier V, Comerford A, Yoshihara L, Ismail M, Wall WA (2012) A novel formulation for Neumann inflow boundary conditions in biomechanics. Int J Numer Methods Biomed Eng 28:560–573
83. Gravemeier V, Gee MW, Kronbichler M, Wall WA (2010) An algebraic variational multiscale-multigrid method for large-eddy simulation of turbulent flow. Comput Methods Appl Mech Eng 199:853–864
84. Gravemeier V, Gee MW, Wall WA (2009) An algebraic variational multiscale-multigrid method based on plain aggregation for convection-diffusion problems. Comput Methods Appl Mech Eng 198:3821–3835
85. Gravemeier V, Kronbichler M, Gee MW, Wall WA (2011) An algebraic variational multiscale-multigrid method for large-eddy simulation: generalized-α time integration, Fourier analysis and application to turbulent flow past a square-section cylinder. Comput Mech 47:217–233
86. Gravemeier V, Lenz S, Wall WA (2008) Towards a taxonomy for multiscale methods in computational mechanics: building blocks of existing methods. Comput Mech 41:279–291
87. Gravemeier V, Wall WA (2010) An algebraic variational multiscale-multigrid method for large-eddy simulation of turbulent variable-density flow at low Mach number. J Comput Phys 229:6047–6070
88. Gravemeier V, Wall WA (2011) Residual-based variational multiscale methods for laminar, transitional and turbulent variable-density flow at low Mach number. Int J Numer Methods Fluids 65:1260–1278
89. Gravemeier V, Wall WA (2011) Variational multiscale methods for premixed combustion based on a progress-variable approach. Combust Flame 158:1160–1170
90. Gravemeier V, Wall WA, Ramm E (2004) A three-level finite element method for the instationary incompressible Navier-Stokes equations. Comput Methods Appl Mech Eng 193:1323–1366
91. Gravemeier V, Wall WA, Ramm E (2005) Large eddy simulation of turbulent incompressible flows by a three-level finite element method. Int J Numer Methods Fluids 48:1067–1099
92. Gresho PM, Sani RL (2000) Incompressible flow and the finite element method, volume 1, advection-diffusion. Wiley, Chichester
93. Gresho PM, Sani RL (2000) Incompressible flow and the finite element method, volume 2, isothermal laminar flow. Wiley, Chichester
94. Guermond JL (1999) Stabilization of Galerkin approximations of transport equations by subgrid modeling. Math Model Numer Anal 33:1293–1316

95. Guermond JL, Oden JT, Prudhomme S (2004) Mathematical perspectives on large eddy simulation models for turbulent flows. J Math Fluid Mech 6:194–248
96. Hachem E, Rivaux B, Kloczko T, Digonnet H, Coupez T (2010) Stabilized finite element method for incompressible flows with high Reynolds number. J Comput Phys 229:8643–8665
97. Hansbo A, Hansbo P (2002) An unfitted finite element method, based on Nitsche's method, for elliptic interface problems. Comput Methods Appl Mech Eng 191:5537–5552
98. Hansbo P, Larson MG, Zahedi S (2014) A cut finite element method for a Stokes interface problem. Appl Numer Math 85:90–114
99. Harari I, Hauke G (2007) Semidiscrete formulations for transient transport at small time steps. Int J Numer Methods Fluids 54:731–743
100. Härtel C, Kleiser L, Unger F, Friedrich R (1994) Subgrid-scale energy transfer in the near-wall region of turbulent flows. Phys Fluids 6:3130–3143
101. Harten A (1996) Multiresolution representation of data: a general framework. SIAM J Numer Anal 33:1205–1256
102. Henke F (2012) An extended finite element method for turbulent premixed combustion. Dissertation, Technische Universität München
103. Henke F, Winklmaier M, Gravemeier V, Wall WA (2014) A semi-Lagrangean time-integration approach for extended finite element methods. Int J Numer Methods Eng 98:174–202
104. Hickel S, Adams NA, Domaradzki JA (2006) An adaptive local deconvolution method for implicit LES. J Comput Phys 213:413–436
105. Hsu TC, Akkerman I, Bazilevs Y (2011) High-performance computing of wind turbine aerodynamics using isogeometric analysis. Comput Fluids 49:93–100
106. Hughes TJR (1995) Multiscale phenomena: green's functions, the Dirichlet-to-Neumann formulation, subgrid scale models, bubbles and the origins of stabilized methods. Comput Methods Appl Mech Eng 127:387–401
107. Hughes TJR, Feijóo GR, Mazzei L, Quincy JB (1998) The variational multiscale method—A paradigm for computational mechanics. Comput Methods Appl Mech Eng 166:3–24
108. Hughes TJR, Franca LP, Balestra M (1986) A new finite element formulation for computational fluid dynamics: V. Circumventing the Babuška-Brezzi condition: A stable Petrov-Galerkin formulation of the Stokes problem accommodating equal-order interpolation. Comput Methods Appl Mech Eng 59:85–99
109. Hughes TJR, Franca LP, Hulbert M (1989) A new finite element formulation for computational fluid dynamics: VIII. The Galerkin/least-squares method for advective-diffusive equations. Comput Methods Appl Mech Eng 73:173–189
110. Hughes TJR, Mazzei L, Jansen KE (2000) Large eddy simulation and the variational multiscale method. Comput Vis Sci 3:47–59
111. Hughes TJR, Mazzei L, Oberai AA, Wray AA (2001) The multiscale formulation of large eddy simulation: decay of homogeneous isotropic turbulence. Phys Fluids 13:505–512
112. Hughes TJR, Wells GN (2005) Conservation properties for the Galerkin and stabilised forms of the advection-diffusion and incompressible Navier-Stokes equations. Comput Methods Appl Mech Eng 194:1141–1159
113. Janicka J, Sadiki A (2005) Large eddy simulation of turbulent combustion systems. Proc Combust Inst 30:537–547
114. Jansen KE, Tejada-Martínez AE (2002) An evaluation of the variational multiscale model for large-eddy simulation while using a hierarchical basis. AIAA Paper 2002-0283, Reno, NV
115. Jansen KE, Whiting CH, Hulbert GM (2000) A generalized-α method for integrating the filtered Navier-Stokes equations with a stabilized finite element method. Comput Methods Appl Mech Eng 190:305–319
116. Jeanmart H, Winckelmans GS (2007) Investigation of eddy-viscosity models modified using discrete filters: a simplified "regularized variational multiscale model" and an "enhanced field model". Phys Fluids 19:055110
117. John V (2004) Large eddy simulation of turbulent incompressible flows. Springer, Berlin
118. John V (2006) On large eddy simulation and variational multiscale methods in the numerical simulation of turbulent incompressible flows. Appl Math 51:321–353
119. John V, Kaya S (2005) A finite element variational multiscale method for the Navier-Stokes equations. SIAM J Sci Comput 26:1485–1503
120. John V, Kaya S (2008) Finite element error analysis for a projection-based variational multiscale method with nonlinear eddy viscosity. J Math Anal Appl 344:627–641
121. John V, Kindl A (2010) Numerical studies of finite element variational multiscale methods for turbulent flow simulations. Comput Methods Appl Mech Eng 199:841–852
122. John V, Kindl A (2010) A variational multiscale method for turbulent flow simulation with adaptive large scale space. J Comput Phys 229:301–312
123. Johnson C, Nävert U, Pitkäranta J (1984) Finite element methods for linear hyperbolic problems. Comput Methods Appl Mech Eng 45:285–312
124. Kamran K, Rossi R, Oñate E (2015) A locally extended finite element method for the simulation of multi-fluid flows using the particle level set method. Comput Methods Appl Mech Eng 294:1–18
125. Kawamura H, Ohsaka K, Abe H, Yamamoto K (1998) DNS of turbulent heat transfer in channel flow with low to medium-high Prandtl number fluid. Int J Heat Fluid Flow 19:482–491
126. Kees CE, Akkerman I, Farthing MW, Bazilevs Y (2011) A conservative level set method suitable for variable-order approximations and unstructured meshes. J Comput Phys 230:4536–4558
127. Knaepen B, Debliquy O, Carati D (2005) Large-eddy simulation without filter. J Comput Phys 205:98–107
128. Kolmogorov AN (1991) The local structure of turbulence in incompressible viscous fluid for very large Reynolds numbers. In: Proceedings of the Royal Society of London A: Mathematical, Physical & Engineering Sciences, vol 434, pp 9–13 (republished English translation of Doklady Akademii Nauk SSSR, vol 30, pp 299–303, 1941 **in Russian**)
129. Koobus B, Farhat C (2004) A variational multiscale method for the large eddy simulation of compressible turbulent flows on unstructured meshes - application to vortex shedding. Comput Methods Appl Mech Eng 193:1367–1383
130. Krank B, Wall WA (2016) A new approach to wall modeling in LES of incompressible flow via function enrichment. J Comput Phys 316:94–116
131. Labourasse E, Lacanette D, Toutant A, Lubin P, Vincent S, Lebaigue O, Caltagirone JP, Sagaut P (2007) Towards large eddy simulation of isothermal two-phase flows: governing equations and a priori tests. Int J Multiph Flow 33:1–39
132. Lallemand MH, Steve H, Dervieux A (1992) Unstructured multigridding by volume agglomeration: current status. Comput Fluids 21:397–433
133. Larsson J, Kawai S, Bodart J, Bermejo-Moreno I (2016) Large eddy simulation with modeled wall-stress: recent progress and future directions. Mech Eng Rev 3:15–00418
134. Layton W (1999) Weak imposition of "no-slip" conditions in finite element methods. Comput Math Appl 38:129–142

135. Layton W, Röhe L, Tran H (2011) Explicitly uncoupled VMS stabilization of fluid flow. Comput Methods Appl Mech Eng 200:3183–3199
136. Layton WJ (2002) A connection between subgrid scale eddy viscosity and mixed methods. Appl Math Comput 133:147–157
137. Leonard A (1974) Energy cascade in large eddy simulation of turbulent fluid flow. Adv Geophys A 18:237–248
138. Lesieur M, Métais O (1996) New trends in large-eddy simulations of turbulence. Annu Rev Fluid Mech 28:45–82
139. Lessani B, Papalexandris MV (2006) Time-accurate calculation of variable density flows with strong temperature gradients and combustion. J Comput Phys 212:218–246
140. Lilly DK (1992) A proposed modification of the Germano subgrid-scale closure method. Phys Fluids 4:633–635
141. Lin PT, Sala M, Shadid JN, Tuminaro RS (2006) Performance of fully coupled algebraic multilevel domain decomposition preconditioners for incompressible flow and transport. Int J Numer Methods Eng 67:208–225
142. Lins EF, Elias RN, Fuerra GM, Rochinha FA, Coutinho ALGA (2009) Edge-based finite element implementation of the residual-based variational multiscale method. Int J Numer Methods Fluids 61:1–22
143. Liu S, Meneveau C, Katz J (1994) On the properties of similarity subgrid-scale models as deduced from measurements in a turbulent jet. J Fluid Mech 215:83–119
144. Liu W (2009) A triple level finite element method for large eddy simulations. J Comput Phys 228:2690–2706
145. Majda A, Sethian J (1985) The derivation and numerical solution of the equations for zero Mach number combustion. Combust Sci Technol 42:185–205
146. Martin MP, Piomelli U, Candler GV (2000) Subgrid-scale models for compressible large-eddy simulations. Theor Comput Fluid Dyn 13:361–376
147. Masud A, Calderer R (2011) A variational multiscale method for incompressible turbulent flows: bubble functions and fine scale fields. Comput Methods Appl Mech Eng 200:2577–2593
148. Mavriplis DJ, Venkatakrishnan V (1996) A 3D agglomeration multigrid solver for the Reynolds-averaged Navier-Stokes equations on unstructured meshes. Int J Numer Methods Fluids 23:527–544
149. Meneveau C (2012) Germano identity-based subgrid-scale modeling: a brief survey of variations on a fertile theme. Phys Fluids 24:121301
150. Meneveau C, Katz J (2000) Scale-invariance and turbulence models for large-eddy simulation. Annu Rev Fluid Mech 32:1–32
151. Meneveau C, Sreenivasan KR (1991) The multifractal nature of turbulent energy dissipation. J Fluid Mech 224:429–484
152. Moës N, Dolbow J, Belytschko T (1999) A finite element method for crack growth without remeshing. Int J Numer Methods Eng 46:131–150
153. Moin P (2002) Advances in large eddy simulation methodology for complex flows. Int J Heat Fluid Flow 23:710–720
154. Moin P, Squires K, Cabot W, Lee S (1991) A dynamic subgrid-scale model for compressible turbulence and scalar transport. Phys Fluids 3:2746–2757
155. Moser RD, Kim J, Mansour NN (1999) Direct numerical simulation of turbulent channel flow up to $\mathrm{Re}_\tau = 590$. Phys Fluids 11:943–945
156. Müller B (1998) Low-Mach-number asymptotics of the Navier-Stokes equations. J Eng Math 34:97–109
157. Mullin JA, Dahm WJA (2006) Dual-plane stereo particle image velocimetry measurements of velocity gradient tensor fields in turbulent shear flow. II. Experimental results. Phys Fluids 18:035102
158. Munts EA, Hulshoff SJ, de Borst R (2007) A modal-based multiscale method for large eddy simulation. J Comput Phys 224:389–402
159. Nagrath S, Jansen KE, Lahey RT Jr (2005) Computation of incompressible bubble dynamics with a stabilized finite element level set method. Comput Methods Appl Mech Eng 194:4565–4587
160. Nitsche J (1971) Über ein Variationsprinzip zur Lösung von Dirichlet-Problemen bei Verwendung von Teilräumen, die keinen Randbedingungen unterworfen sind. Abhandlungen aus dem Mathematischen Seminar der Universität Hamburg 36:9–15
161. Oñate E (1998) Derivation of stabilized equations for numerical solution of advective-diffusive transport and fluid flow problems. Comput Methods Appl Mech Eng 151:233–265
162. Oñate E, Valls A, Garcia J (2007) Computation of turbulent flows using a finite calculus-finite element formulation. Int J Numer Methods Fluids 54:609–637
163. Oberai AA, Liu J, Sondak D, Hughes TJR (2014) A residual based eddy viscosity model for the large eddy simulation of turbulent flows. Comput Methods Appl Mech Eng 282:54–70
164. Oberai AA, Wanderer J (2005) Variational formulation of the Germano identity for the Navier-Stokes equations. J Turbul 6:1–17
165. Olshanskii M, Lube G, Heister T, Löwe J (2009) Grad-div stabilization and pressure models for the incompressible Navier-Stokes equations. Comput Methods Appl Mech Eng 198:3975–3988
166. Peters N (2000) Turbulent combustion. Cambridge University Press, Cambridge
167. Piomelli U (1999) Large-eddy simulation: Achievements and challenges. Prog Aerosp Sci 35:335–362
168. Piomelli U (2008) Wall-layer models for large-eddy simulations. Prog Aerosp Sci 44:437–446
169. Piomelli U, Balaras E (2002) Wall-layer models for large-eddy simulations. Annu Rev Fluid Mech 34:349–374
170. Piomelli U, Cabot WH, Moin P, Lee S (1991) Subgrid-scale backscatter in turbulent and transitional flows. Phys Fluids A 3:1766–1771
171. Pitsch H (2006) Large-eddy simulation of turbulent combustion. Annu Rev Fluid Mech 38:453–482
172. Poinsot T, Veynante D (2005) Theoretical and numerical combustion. R.T. Edwards, Philadelphia
173. Pope SB (2000) Turbulent flows. Cambridge University Press, Cambridge
174. Prasad RR, Meneveau C, Sreenivasan KR (1988) Multifractal nature of the dissipation field of passive scalars in fully turbulent flows. Phys Rev Lett 61:74–77
175. Ramakrishnan S, Collis SS (2006) Partition selection in multiscale turbulence modeling. Phys Fluids 18:075105
176. Rasquin M, Smith C, Chitale K, Seol ES, Matthews BA, Martin JL, Sahni O, Loy RM, Shephard MS, Jansen KE (2014) Scalable implicit flow solver for realistic wing simulations with flow control. Comput Sci Eng 16:13–21
177. Rasthofer U (2015) Computational multiscale methods for turbulent single and two-phase flows. Dissertation, Technische Universität München
178. Rasthofer U, Burton GC, Wall WA, Gravemeier V (2014) An algebraic variational multiscale-multigrid-multifractal method (AVM^4) for large-eddy simulation of turbulent variable-density flow at low Mach number. Int J Numer Meth Fluids 76:416–449
179. Rasthofer U, Burton GC, Wall WA, Gravemeier V (2014) Multifractal subgrid-scale modeling within a variational multiscale

method for large-eddy simulation of passive-scalar mixing in turbulent flow at low and high Schmidt numbers. Phys Fluids 26:055108
180. Rasthofer U, Gravemeier V (2013) Multifractal subgrid-scale modeling within a variational multiscale method for large-eddy simulation of turbulent flow. J Comput Phys 234:79–107
181. Rasthofer U, Henke F, Wall WA, Gravemeier V (2011) An extended residual-based variational multiscale method for two-phase flow including surface tension. Comput Methods Appl Mech Eng 200:1866–1876
182. Rasthofer U, Wall WA, Gravemeier V (2016) An extended algebraic variational multiscale-multigrid-multifractal method ($XAVM^4$) for large-eddy simulation of turbulent two-phase flow (under review)
183. Rehm RG, Baum HR (1978) The equations of motion for thermally driven, buoyant flows. J Res Natl Bur Sci 83:297–308
184. Rodriguez JM, Sahni O, Lahey RT Jr, Jansen KE (2013) A parallel adaptive mesh method for the numerical simulation of multiphase flows. Comput Fluids 87:115–131
185. Rogallo RS, Moin P (1984) Numerical simulation of turbulent flows. Annu Rev Fluid Mech 16:99–137
186. Röhe L, Lube G (2010) Analysis of a variational multiscale method for large-eddy simulation and its application to homogeneous isotropic turbulence. Comput Methods Appl Mech Eng 199:2331–2342
187. Russo A (1996) Bubble stabilization of finite element methods for the linearized incompressible Navier-Stokes equations. Comput Methods Appl Mech Eng 132:335–343
188. Sagaut P (2006) Large eddy simulation for incompressible flows. Springer, Berlin
189. Sagaut P, Ciardi M (2006) A finite-volume variational multiscale method coupled with a discrete interpolation filter for large-eddy simulation of isotropic turbulence and fully developed channel flow. Phys of Fluids 18:115101
190. Sagaut P, Deck S, Terracol M (2006) Multiscale and multiresolution approaches in turbulence. Imperial College Press, London
191. Sauerland H, Fries TP (2011) The extended finite element method for two-phase and free-surface flows: a systematic study. J Comput Phys 230:3369–3390
192. Scardovelli R, Zaleski S (1999) Direct numerical simulation of free-surface and interfacial flow. Annu Rev Fluid Mech 31:567–603
193. Schott B, Rasthofer U, Gravemeier V, Wall WA (2015) A face-oriented stabilized Nitsche-type extended variational multiscale method for incompressible two-phase flow. Int J Numer Methods Eng 104:721–748
194. Schott B, Wall WA (2014) A new face-oriented stabilized XFEM approach for 2D and 3D incompressible Navier-Stokes equations. Comput Methods Appl Mech Eng 276:233–265
195. Schumann U (1975) Subgrid scale model for finite difference simulations of turbulent flows in plane channels and annuli. J Comput Phys 18:376–404
196. Smagorinsky J (1963) General circulation experiments with the primitive equations. I. The basic experiment. Mon Weather Rev 91:99–164
197. Spalart PR (2009) Detached-eddy simulation. Annu Rev Fluid Mech 41:181–202
198. Spalart PR, Deck S, Shur ML, Squires KD, Strelets MK, Travin A (2006) A new version of detached-eddy simulation, resistant to ambiguous grid densities. Theor Comput Fluid Dyn 20:181–195
199. Spalart PR, Jou WH, Strelets M, Allmaras SR (1997) Comments on the feasibility of LES for wings, and on a hybrid RANS/LES approach. In: Liu C, Liu Z (eds) Advances in DNS/LES. Greyden Press, Columbus, pp 137–147
200. Spalding DB (1961) A single formula for the law of the wall. J Appl Mech 28:444–458
201. Sreenivasan KR (1991) Fractals and multifractals in fluid turbulence. Annu Rev Fluid Mech 23:539–600
202. Sreenivasan KR, Stolovitzky G (1995) Turbulent cascades. J Stat Phys 78:311–333
203. Stenberg R (1995) On some techniques for approximating boundary conditions in the finite element method. J Comput Appl Math 63:139–148
204. Stolz S, Adams NA (1999) An approximate deconvolution procedure for large-eddy simulation. Phys Fluids 11:1699–1701
205. Stolz S, Schlatter P, Kleiser L (2005) High-pass filtered eddy-viscosity models for large-eddy simulations of transitional and turbulent flow. Phys Fluids 17:065103
206. Taylor CA, Hughes TJR, Zarins CK (1998) Finite element modeling of blood flow in arteries. Comput Methods Appl Mech Eng 158:155–196
207. Tennekes H, Lumley JL (1972) A first course in turbulence. MIT Press, Cambridge
208. Tezduyar TE, Mittal S, Ray SE, Shih R (1992) Incompressible flow computations with stabilized bilinear and linear equal-order-interpolation velocity-pressure elements. Comput Methods Appl Mech Eng 95:221–242
209. Tezduyar TE, Osawa Y (2000) Finite element stabilization parameters computed from element matrices and vectors. Comput Methods Appl Mech Eng 190:411–430
210. Tryggvason G, Scardovelli R, Zaleski S (2011) Direct numerical simulations of gas-liquid multiphase flows. Cambridge University Press, New York
211. Tuminaro R, Tong C (2000) Parallel smoothed aggregation multigrid: aggregation strategies on massively parallel machines. In: J. Donnelley (ed.) Super computing 2000 proceedings
212. Vaněk P, Mandel J, Brezina M (1996) Algebraic multigrid by smoothed aggregation for second and fourth order elliptic problems. Computing 56:179–196
213. Veynante D, Vervisch L (2002) Turbulent combustion modeling. Prog Energy Combust Sci 28:192–266
214. Vreman AW (2003) The filtering analog of the varaitional multiscale method in large-eddy simulation. Phys Fluids 15:L61–L64
215. Vreman AW (2004) An eddy-viscosity subgrid-scale model for turbulent shear flow: algebraic theory and applications. Phys Fluids 16:3670–3681
216. Wanderer J, Oberai AA (2008) A two-parameter variational multiscale method for large eddy simulation. Phys Fluids 20:085107
217. Wang M, Moin P (2002) Dynamic wall modeling for large-eddy simulation of complex turbulent flows. Phys Fluids 14:2043–2051
218. Warnatz J, Maas U, Dibble RW (2001) Combustion: physical and chemical fundamentals, modeling and simulation, experiments, pollutant formation. Springer, Berlin
219. Wasberg CE, Gjesdal T, Reif BAP, Andreassen O (2009) Variational multiscale turbulence modelling in a high order spectral element method. J Comput Phys 228:7333–7356
220. Whiting CH, Jansen KE (2001) A stabilized finite element method for the incompressible Navier-Stokes equations using a hierarchical basis. Int J Numer Methods Fluids 35:93–116
221. Williams FA (1985) Combustion theory. Perseus Books, Reading
222. Zang Y, Street RL, Koseff JR (1993) A dynamic mixed subgrid-scale model and its application to turbulent recirculating flows. Phys Fluids 5:3186–3196
223. Zienkiewicz OC, Taylor RL, Zhu JZ (2005) The finite element method, Volume 1, its basis & fundamentals. Butterworth-Heinemann, Oxford